THE UNIVERSITY OF MANITOBA

ULTRASONIC VELOCITY AND ATTENUATION IN A GLASS-BEAD PERCOLATION SYSTEM

by

NORBERT GEORGE PACHET

A thesis submitted to the Faculty of Graduate Studies
in partial fulfillment of the requirements for
the degree of Master of Science

DEPARTMENT OF PHYSICS

Winnipeg, Manitoba, Canada
June, 1990

ISBN 0-315-63365-4

ULTRASONIC VELOCITY AND ATTENUATION IN A GLASS-BEAD PERCOLATION SYSTEM

by

Norbert George Pachet

A thesis submitted to the Faculty of Graduate Studies of the University of Manitoba in partial fulfillment of the requirements of the degree of

Master of Science

ABSTRACT

Ultrasonic velocity and attenuation measurements in the 1-20 MHz frequency range have been performed in a structural percolation system formed from glass microspheres of radius 1 μm . In these samples the positions of the particles and voids are symmetrically controlled (as in percolation) by first mixing the glass microspheres with nickel powder of similar grain size, the nickel powder being removed by etching in acid after the glass is sintered. The ultrasonic attenuation depends strongly on frequency; at the highest measurable frequencies, the mean free path of the ultrasonic wave is less than its wavelength, suggestive of a crossover to localized vibrational exitations. The measurements on these glass percolation networks permit the scaling behaviour of the ultrasonic velocity and attenuation to be studied closer to the percolation threshold than was possible in earlier work on metal sinters.

ACKNOWLEDGEMENTS

I would like to give great thanks my supervisor, Dr. John Page, for his endless patience and guidance throughout every stage of this work.

There are many people to whom I owe thanks for the assistance they provided: Tadeusz Foniok and Wayne Blonski of Geology for usage of their mixing apparatus, Henry Schriemer and Gary Cosby for portions of the data collection, Ron Chapman of Geology for carbon coating samples, Gail Pelletier for showing me the ropes on the SEM, the eternal Gilles Roy who showed me a that minute of work can save an hour of thought (and Dr. Page who showed me that a minute of thought can save an hour of work), and Drs. H. Gesser, B. Southern, and G. Williams for their committee work.

In addition, I give my heart-felt appreciation to my parents for their support and patience over the years. I would also like to extend my gratitude to my friends for keeping me relatively sane, and for the late night cinnamon coffee.

To Dan Vosper

Table of Contents

CHAPTER I: INTRODUCTION

Our interest in the anomalous vibrational properties of porous sintered materials originated about 15 years ago in the field of low temperature physics. At temperatures below 100 mK , the thermal boundary resistance or Kapitza resistance, between a solid material and liquid helium becomes large (for example, see Harrison [1979]). In order to reduce this resistance, the surface area of the solid was vastly increased by sintering powdered metal to form a metal sponge. This enhanced the surface area of the metal, and hence the heat exchange interface, by about four orders of magnitude.

About 15 years ago, it was found that below 20 mK the Kapitza resistance with pure ^3He was reduced more than could be explained by the increase of surface area of the heat exchanger. In addition, the temperature dependence of this resistance changed from T^{-3} to T^{-1}. Experiments supporting this dependence have been summarized by Harrison [1979]. Rutherford *et al* [1984] proposed that this modified heat transfer process was caused by a change in vibrational modes due to the disordered microscopic structure of the sinter. They commented that a sample created from sintered powder has three main frequency bands that are dictated by the grainy structure, as the schematic in Figure I-1 shows. At high frequencies, when the wavelength is smaller than the particle size, the vibrational modes induced are those of bulk material, albeit scattered at the particle boundaries. However, as the frequency is decreased, the wavelength approaches a size comparable to the

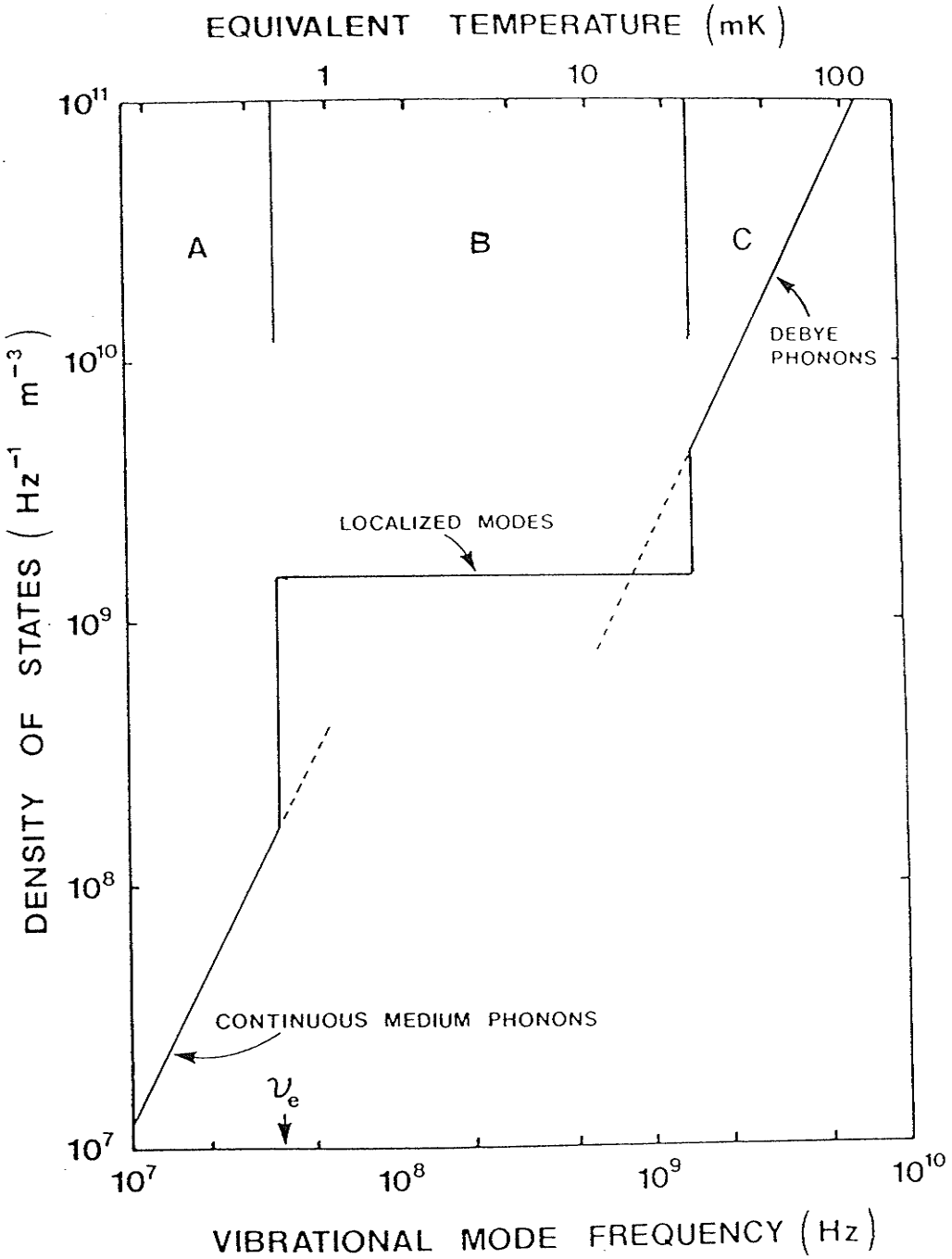

Figure I-1: Density of states of vibrational modes of sintered metal powder The band-edge frequency ν_e was determined by the condition $\lambda_e \sim 10d$. The upper scale is a measure of the temperature at which modes with frequency along the lower scale dominate in the excitation spectrum (after Maliepaard *et al* [1985]).

particle size, and the vibration is no longer free to propagate in the same manner as it did at the higher frequency: a cut-off frequency exists. This corresponds to the crossover between regions C and B of the figure. Now if one instead considers very low frequencies such that the length scale of the the finite particle and hole size is very small compared to the wavelength, then the entire sample effectively acts as a homogeneous medium. However, if the frequency is increased and the wavelength approaches the length scale of the average hole size, the medium can no longer be considered homogeneous: another cut-off corresponding to the crossover between regions A and B exists. Therefore between a wavelength longer than the particle size and a wavelength shorter than the average hole size lies a regime for which the nature of the vibrational modes is strongly influenced by the structural disorder. For this frequency range, we expect that the vibrations are strongly scattered so that the extended vibrations that propagate freely in an ordered solid may be replaced by localized acoustic modes.

Maliepaard *et al* [1985] investigated these vibrational regimes by propagating ultrasonic pulses through metal sinters. They found that at long wavelengths, the ultrasonic attenuation was low and the vibrational modes were correctly described by phonons with "soft" phonon velocities compared with bulk. The softening of the velocities with occupied volume fraction was in good agreement with a theoretical model of the elasticity of a percolating system [Kantor and Webman, 1984] and confirmed that the elasticity belongs to a different universality class than conductivity. At shorter wavelengths, they found a dramatic increase in the ultrasonic attenuation, corresponding to a rapid decrease in the mean free path, which indicated a crossover from

extended to localized vibrational modes. The attenuation was found to scale with the percolation correlation length that marks the boundary between the homogeneous and fractal regions of a percolating structure.

There were some drawbacks to the sample preparation method used by Maliepaard *et al.* The procedure used to create a sample involved packing a given amount of powder down to a predetermined thickness in order to obtain a chosen occupied volume fraction. This method of preparation does not correspond to an ideal percolating system for which each lattice site randomly does or does not contain a particle; there was no mechanism by which the distribution of the voids in the sample was controlled. In addition, the sinters were not truly fractal over a large range of length scales (although some submicron sinters were disordered over a large range of length scales).

In this thesis, these two problems are addressed. The positions of both the particles and the voids are symmetrically controlled (as they are in percolation) by introducing a second transitory powder to the sample. Specifically, glass beads were mixed with a metal powder of a similar grain size, and after the glass was sintered, the sample was immersed in acid to remove the metal. Homogeneous mixing of the two materials permits a truly random distribution of both constituents so that the resulting etched sinter is a nearly ideal physical realization of a percolating structure. Preliminary results of ultrasonic velocity and attenuation measurements performed on such samples have been discussed by Pachet and Page [1990].

In the next chapter, the aspects of percolation theory pertinent to the collected data are discussed. In Chapter III , the method of sample preparation is described in depth. In Chapter IV , the appa-

ratus and procedure used to collect the ultrasonic data are listed, while the data and its analysis are presented in Chapter V . Chapter VI is a self-contained section involving an investigation of the fractal nature of one of the samples, and conclusions are summarized in Chapter VII.

CHAPTER II: THEORY

This chapter introduces percolation theory and its scaling properties. It shows the dependence of the density and sound velocity of a percolating system on both the scaling properties of the system and its self-similar fractal nature. In §II:2 , the scaling and frequency dependence of the ultrasonic attenuation is discussed, and in the final section two microscopic elasticity models dependent upon percolation theory are presented.

§II: 1 — PERCOLATION THEORY AND SCALING RELATIONS FOR THE ULTRASONIC VELOCITY

The terminology and some theoretical results of percolation theory are presented in this section. Any intrinsic property of a percolating material dependent upon length (such as density or sound velocity) is expected to scale with the intrinsic correlation length of the sample. Percolating systems exhibit self-similar properties below this correlation length.

§II: 1.1 — Introduction to Percolation Theory

Consider an infinite volume consisting of lattice sites which are either occupied with probability p or empty with probability $1 - p$. An occupied site can be defined as part of a cluster if it is a nearest neighbour of an occupied site of the cluster. A system for which the distribution is $p = 1$ will have every occupied site belonging to the same cluster of infinite extent. As the value of p is decreased, there will be some occupied sites which are separate from the infinite cluster and form their own finite clusters. If p is very close to zero, then most clusters will consist of only one occupied site, and there is no infinite cluster. Between the two extremes lies a critical probability p_c (the percolation threshold) above which there is an

infinite cluster, and below which there is not. In this thesis, percolation theory is used to model the properties of porous solids so that we are exclusively interested in the behaviour of the infinite cluster for $p \gtrsim p_c$.

An important length scale that influences the vibrational properties of an infinite percolating cluster is the correlation or connectivity length ξ , which corresponds to an average radius of the largest holes in the cluster [Stauffer, 1985]. As p_c is approached from above, this average hole size diverges. The critical exponent ν is defined such that

$$\xi \propto (p - p_c)^{-\nu} \quad . \tag{II-1}$$

Numerical calculations have been performed to evaluate ν with the result that for three dimensions, $\nu = 0.88$ [Stanley, 1986] . For experimental systems such as the porous sinters described in this thesis, it is the occupied volume fraction f and not the percolation probability that is the experimentally controlled variable. If we assume that random percolation belongs to the same universality class as lattice-based percolation, the correlation length will scale with $f-f_c$ according to the same power law as it does for $p-p_c$:

$$\xi \propto (f - f_c)^{-\nu} \quad . \tag{II-2}$$

In summary, Equation (II-1) applies when performing computer simulations, and Equation (II-2) applies in experimental situations.

An object is considered to be a *fractal* if it has dilational symmetry. That is, the appearance of the object remains essentially unchanged with change in length scale. Below the correlation length ξ and extending down to the size of the individual cluster components, a percolating system exhibits such behaviour.

§II: 1.2 — Fractal Objects

A usual, everyday Euclidean object has translational symmetry and requires only a single dimension to describe its space: d . Fractal objects, however, have dilational symmetry. Because of this, there are three dimensions necessary to describe a fractal object:

d, the usual Euclidean spatial dimension,

D, the fractal (Hausdorff) dimension, and

$\tilde{d}$, the fracton (spectral) dimension.

The Euclidean dimension describes the space in which the fractal is imbedded while the two other dimensions are defined in analogy to the familiar concepts of mass and density of vibrational states, as described in the following subsections.

§II: 1.2a — Fractal (Hausdorff) Dimension D

If m is the mass and L is the length scale of a structure, then

$$m \propto L^{d} \qquad \text{(II-3a)}$$

in normal Euclidean space. In analogy to this, for a fractal structure, the fractal dimension D is defined such that

$$m \propto L^{D} \quad . \tag{II-3b}$$

For example, in three dimensions $d = 3$ while $D \leq 3$ and is not necessarily an integer.

It is possible to derive the length scale dependence of the density of a fractal if one refers to the definition of density in Euclidean space:

$$\rho = \frac{\text{mass}}{\text{volume}} \propto \frac{L^{d}}{L^{d}} \propto L^{0} \quad . \tag{II-4a}$$

That is, the density in Euclidean space is not dependent on the length scale. However, in fractal space, the mass does not have the same length dependence as the volume in which it is imbedded. Therefore

$$\rho \propto \frac{L^{D}}{L^{d}} \propto L^{D-d} \quad . \tag{II-4b}$$

For a percolating system with $p > p_c$, ρ has the length scale dependence of Equation (II-4b) when $L \leq \xi$, and the length scale independence of Equation (II-4a) when $L \geq \xi$. Since density at $L = \xi$ must be the same at length scales longer than ξ, then the measured bulk density ρ_o can be expressed as

$$\rho_o \propto \xi^{D-d}$$

so that

$$\rho_o \propto (p - p_c)^{\nu(d-D)} \tag{II-5}$$

from Equation (II-1) . By definition,

$$\rho \propto (p - p_c)^{\beta} \quad , \tag{II-6}$$

with numerical evaluations yielding $\beta = 0.44$ [Stanley, 1986] for three dimensions. Equations (II-5 and 6) give the relation

$$D = d - \frac{\beta}{\nu} \tag{II-7}$$

which yields the theoretical result that $D = 2.50$ for $d=3$.

§II: 1.2b — Fracton (Spectral) Dimension $\tilde{d}$

In Euclidean space, the low frequency vibrational modes of a solid are sound waves, for which the frequency ω is equal to the magnitude of the velocity v times the magnitude of the d-dimensional wavevector $\underline{k}$. In the Debye model, this phonon dispersion relationship

$$\omega = v\, k \tag{II-8}$$

can be used to calculate the density of states $g(\omega)$:

$$g(\omega) = \int \frac{d^d \underline{k}}{(2\pi/L)^d} \delta[\omega - \omega(\underline{k})]$$

$$g(\omega) \propto \int k^{d-1}\, dk\, \delta[\omega - vk] \quad , \quad \omega < \omega_D$$

$$g(\omega) \propto \omega^{d-1} \quad , \quad \omega < \omega_D \tag{II-9}$$

where ω_D is the Debye frequency.

For a fractal structure, the dispersion relation for vibrational frequencies differs from Equation (II-8) and the corresponding excitations are referred to as fractons. Following Rammal and Toulouse [1983], we write the fracton dispersion relation as

$$\omega = b\, k^{a} \qquad \text{(II-10)}$$

where a and b are constants. The density of states for fractons is then

$$g(\omega) \propto \int k^{D-1}\, dk\, \delta[\omega - b\, k^{a}] .$$

Therefore $$g(\omega) \propto \omega^{(D/a - 1)}$$

or $$g(\omega) \propto \omega^{(\tilde{d}-1)} , \qquad \text{(II-11)}$$

where the fracton dimension $\tilde{d} = D/a$ is defined such that the density of states $g(\omega)$ has a frequency dependence analogous to the Debye model, as first proposed by Alexander and Orbach [1982].

§II: 1.3 — Low Frequency Phonon Velocity

Since the infinite cluster of a percolating network is homogeneous at long length scales ($L \gg \xi$) and fractal at short length scales ($L \ll \xi$), the vibrational modes should show a crossover from phonons to fractons when the phonon wavelength is comparable to the correlation length. More precisely, this crossover is expected [Aharony *et al*,

1987] to occur at wavevector $\underline{k}$ such that $k\xi = 1$. The assumption that the phonon and fracton dispersion relations join continuously at this crossover point implies

$$v \xi^{-1} = b \xi^{-a}$$

$$v = b \xi^{1-a}$$

so that

$$v \propto \xi^{(1 - D/\tilde{d})} \qquad \text{(II-12)}$$

since $\tilde{d} = D/a$. With the use of Equation (II-1) , this can be expressed as

$$v \propto (p - p_c)^{\nu(D/\tilde{d} - 1)} \quad . \qquad \text{(II-13)}$$

Note that the phonon velocity v is independent of length scale (for $1/k > \xi$) so that Equation (II-13) predicts that the low frequency phonon velocity varies with $(p - p_c)$ as a simple power law, whose exponent depends on the correlation length exponent ν , the fractal dimension D , and the fracton dimension $\tilde{d}$.

§II: 1.4 — The Fracton Velocity

Writing the fracton dispersion relation (Equation (II-10)) as

$$\omega = (b\, k^{a-1})\, k \qquad \text{(II-14)}$$

suggests that the phase velocity of the fracton excitations is given by

$$\begin{aligned} v_{fr} &= b\, k^{a-1} \\ &= b\left(\frac{\omega}{b}\right)^{(a-1)/a} \\ &= c\, \omega^{(1 - \tilde{d}/D)} \quad . \end{aligned} \tag{II-15}$$

Hence fractons are believed to be dispersive excitations.

§II: 2 — SCALING RELATIONS FOR THE ULTRASONIC ATTENUATION

In this section, the interpretation of ultrasonic attenuation is viewed in the context of elastic scattering. The connection with the Ioffe-Regel criterion for localization is discussed, and various predictions for the frequency dependence of the attenuation in the phonon and fracton regimes of a percolating network are presented.

§II: 2.1 — Localization and the Ioffe-Regel Criterion

The attenuation coefficient of a wave is defined such that

$$I = I_o e^{-\alpha(\omega)x} \qquad \text{(II-16)}$$

where I is the wave intensity, I_o is the initial intensity, $\alpha(\omega)$ is the frequency-dependent attenuation coefficient, and x is the thickness of the attenuating medium. The attenuation $\alpha(\omega)$ consists of inelastic (absorption) and elastic (scattering) components. If the inelastic portion is insignificant relative to the elastic portion, then the attenuation can be associated with the elastic mean free path of the system $\ell(\omega)$ such that Equation (II-16) can be written as

$$I = I_o e^{-x/\ell(\omega)} \quad . \qquad \text{(II-17)}$$

That is, $\alpha(\omega) = \ell(\omega)^{-1}$.

According to single-parameter scaling theory, it is expected that any length-dependent intrinsic property of a material will scale with a critical length scale of the material, in this case the correlation length ξ . Therefore it is expected that the attenuation of any percolating sample due to elastic scattering will have the same wavelength dependence and will fall on a common curve when attenuation and wavelength are both scaled by ξ . This is discussed in greater detail in §V:3.2 .

At low frequencies, the vibrational wavelengths are much larger than the inhomogeneities and the scattering is weak. Thus the attenuation is low and the vibrational modes are correctly described by extended acoustic waves. As the frequency is increased, a condition is eventually attained for which the wavelength of the vibration is of the same order as the inhomogeneities. If the scattering is sufficiently strong, the phonons may become localized. By analogy with related problems in electronic systems, the criterion for localization is usually taken as the Ioffe-Regel condition that the elastic mean free path $\ell(\omega)$ be sufficiently short that

$$k\ell \lesssim 1 \quad . \tag{II-18}$$

Since $\alpha = \ell(\omega)^{-1}$, the localization condition can also be written

$$\frac{\alpha}{k} \gtrsim 1 \quad . \tag{II-19}$$

For a fractal network, the localized vibrations have been referred to as *fractons* [Alexander and Orbach, 1982].

§II: 2.2 — Frequency Dependence of the Attenuation in the Phonon and Fracton Regimes

In a percolating system, for wavelengths much longer than the largest inhomogeneity $\lambda \gg \xi$, the attenuation of the transmitted wave is dominated by Rayleigh scattering and has a frequency dependence of

$$\alpha \propto \frac{\omega^{d+1}}{v^{d}} \quad . \tag{II-20}$$

Thus for a three dimensional system, the attenuation in the phonon regime is expected to be proportional to ω^4 since v is independent of frequency.

For fractons, Aharony *et al* [1987] have calculated that the vibrational relaxation time $\tau(\omega)$ scales with frequency as

$$\frac{1}{\tau(\omega)} \propto \omega^{5-3\tilde{d}} \quad . \tag{II-21}$$

In a percolating system, this behaviour is predicted to occur at frequencies above the phonon-fracton crossover condition $\omega = \omega_c = v k_c$ where $k_c \xi = 1$. When $\tilde{d} = \frac{4}{3}$, the value conjectured by Alexander and Orbach [1982], Equation (II-21) predicts a particularly simple frequency dependence for the fracton relaxation time:

$$\frac{1}{\tau(\omega)} \propto \omega \quad . \tag{II-22}$$

Since fractons are expected to be localized modes (characterized by a single length scale), Aharony *et al* <u>further</u> suggested that the Ioffe-Regel condition $k\ell(\omega) = \omega\tau(\omega) = 1$ also applies throughout the fracton regime, with the implication that the proportional sign should be

replaced by an equals sign in Equation (II-22) . Thus the fractons are expected to be critically damped at all frequencies $\omega > \omega_c$ in this case.

Equations (II-20 and 22) can then be written

$$\frac{1}{\tau(\omega)} = \frac{\omega^4}{\omega_o^3} \qquad \omega < \omega_c \qquad \text{(II-23a)}$$

$$\frac{1}{\tau(\omega)} = \omega \qquad \omega > \omega_c \qquad \text{(II-23b)}$$

where the coefficient $1/\omega_o^3$ measures the strength of the Rayleigh scattering in the phonon regime. Since the phonon and fracton relaxation times are expected to be equal at the crossover frequency ω_c , we have $\omega_o = \omega_c$ for $\tilde{d} = \frac{4}{3}$. The corresponding behaviour of the attenuation is given by

$$\alpha = \frac{1}{v\tau(\omega)} = \frac{\omega^4}{v\omega_c^3} \qquad \omega < \omega_c \qquad \text{(II-24a)}$$

$$\alpha = \frac{1}{v_{fr}\tau(\omega)} = \frac{\omega_c}{v}\left(\frac{\omega}{\omega_c}\right)^{\tilde{d}/D} \qquad \omega > \omega_c \qquad \text{(II-24b)}$$

$$= \frac{\omega_c}{v}\left(\frac{\omega}{\omega_c}\right)^{\frac{4}{3D}} .$$

However if $\tilde{d} < \frac{4}{3}$, Aharony *et al* have pointed out that the situation may be more complicated and have predicted that there are two different fracton regimes. Above the phonon-fracton crossover frequency, $\tau(\omega)^{-1}$ is still given by Equation (II-21), but since $\tilde{d} < \frac{4}{3}$, $\tau(\omega)^{-1}$ varies more than linearly with frequency. Since they believe that fractons cannot be overdamped (that is, $\tau(\omega)^{-1}$ cannot be greater

than ω), two important consequences emerge. The first is that the Ioffe-Regel criterion is not satisfied at $\omega = \omega_c$. The second is that when the Ioffe-Regel condition is reached at some frequency ω_{IR} above ω_c, the frequency dependence of the relaxation time will cross over from $\omega^{5-3\tilde{d}}$ to ω behaviour. In their words "Above this frequency, we would predict a 'quantum' strong scattering regime on the fractal in which $\tilde{d}$ is renormalized to $\tilde{d}_q = \frac{4}{3}$". The predicted frequency dependence of the relaxation time is

$$\text{Phonons}: \quad \frac{1}{\tau(\omega)} = \omega\left(\frac{\omega}{\omega_o}\right)^d \qquad \text{for} \quad \omega < \omega_c , \tag{II-25a}$$

$$\text{"Weakly localized" fractons}: \quad \frac{1}{\tau(\omega)} = \omega\left(\frac{\omega}{\omega_{IR}}\right)^{4-3\tilde{d}} \qquad \text{for} \quad \omega_c < \omega < \omega_{IR} , \tag{II-25b}$$

$$\text{"Strongly localized" fractons}: \quad \frac{1}{\tau(\omega)} = \omega \qquad \text{for} \quad \omega > \omega_{IR} . \tag{II-25c}$$

This behaviour is shown in Figure II-1a. The crossover points ω_c and ω_{IR} are related by assuming a continuous crossover at ω_c to give

$$\omega_c^{\,d-4+3\tilde{d}} = \frac{\omega_o^d}{\omega_{IR}^{\,4-3\tilde{d}}} . \tag{II-26}$$

Thus ω_c is no longer equal to ω_o. The corresponding behaviour of the attenuation is (see Figure II-1b)

$$\alpha = \frac{1}{v\tau(\omega)} \propto \omega^{d+1} \qquad \text{for} \quad \omega < \omega_c , \tag{II-27a}$$

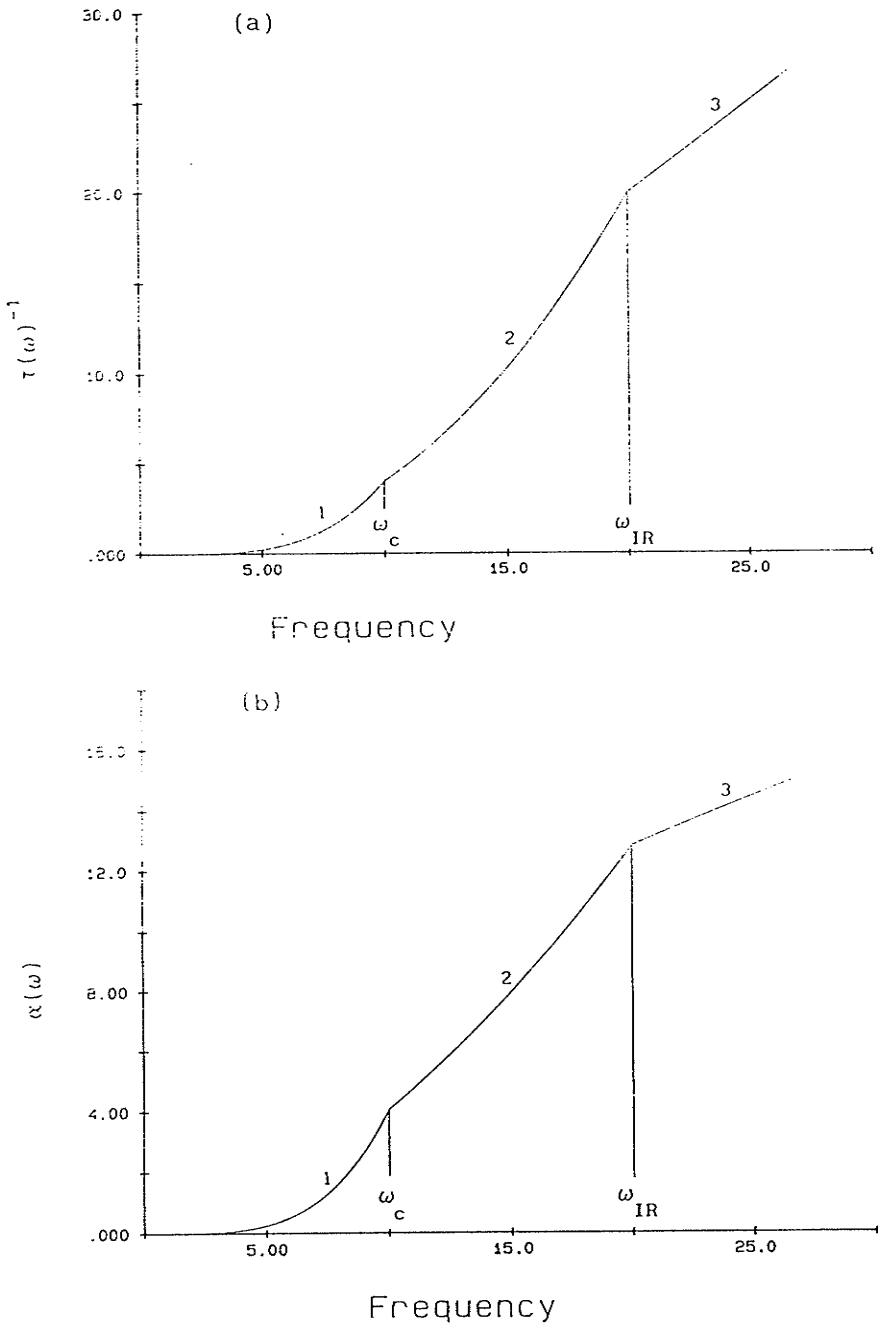

Figure II-1

(a) Schematic of the frequency dependence of the relaxation time $\tau(\omega)$, as predicted by Aharony *et al* [1987]. Region 1 corresponds to the phonon regime, region 2 is the "weakly localized" fractons regime, and region 3 is where "strongly localized" fractons exist.

(b) The corresponding curve for the frequency dependence of the attenuation $\alpha(\omega)$.

$$\alpha = \frac{1}{\mathscr{v}_{fr}\,\tau(\omega)} \propto \omega^{4 - \tilde{d}(3-1/D)} \qquad \text{for } \omega_c < \omega < \omega_{IR}\,, \qquad \text{(II-27b)}$$

$$\alpha = \frac{1}{\mathscr{v}'_{fr}\,\tau(\omega)} \propto \omega^{4/3D} \qquad \text{for } \omega > \omega_{IR}\,. \qquad \text{(II-27c)}$$

Assuming that the dispersion curves join continuously, the velocities $\mathscr{v}_{fr}$ ($\propto \omega^{1-\tilde{d}/D}$) and $\mathscr{v}'_{fr}$ ($\propto \omega^{1-4/3D}$) should be equal at $\omega = \omega_{IR}$, and constants in terms of ω_c and ω_{IR} can be calculated. Equation (II-27) could also be put in the form of equalities when appropriate cumbersome constants are included, joining the curves at the crossover points.

§II: 3 — MICROSCOPIC ELASTICITY MODELS

Several models have been developed to describe the microscopic forces acting between particles in a percolating system. One is a scalar elastic description while another treats the system as a tensorial elastic system with bond-bending forces. These two models predict different dependencies of the macroscopic elastic constants on the occupied volume fraction of the material. The theory of these two models is outlined in the next two sections.

§II: 3.1 — Scalar Elasticity Model

The first model to be studied, which is also the simplest, was the Born model [Born and Huang, 1954]. In this model, the elastic energy of the percolating system is given by

$$H = \frac{1}{2} \sum_{\substack{i,j \\ (nn)}} K_{ij} \left[\alpha (\underline{u}_i - \underline{u}_j)_{\parallel}^2 + \beta (\underline{u}_i - \underline{u}_j)_{\perp}^2 \right] \qquad \text{(II-28)}$$

where nn indicates nearest neighbours, $(\underline{u}_i - \underline{u}_j)_{\parallel}^2$ is the relative displacement of the site j in the direction parallel to the bond that links sites i and j, $(\underline{u}_i - \underline{u}_j)_{\perp}^2$ is the corresponding perpendicular displacement, α and β are constants, and K_{ij} is a variable which assumes either the value 1 with probability p, or the value 0 with probability $(1 - p)$.

In the case that $\alpha = \beta$, the "spring constants" of the bond, both parallel and perpendicular to the bond axis, are equal and the equations of motion are separable for each dimension. The equations of motion for the elasticity and conductivity problems then both have the same form, with the result that their dependence on $p-p_c$ is the same. That is, if we define the critical exponents τ and t for the macroscopic elastic moduli C and conductivity σ by

$$C \propto (p - p_c)^{\tau}$$
$$\sigma \propto (p - p_c)^{t} \quad , \qquad \text{(II-29)}$$

the result for the scalar elasticity model is that $t = \tau$. This result was first noted by de Gennes [1976]. From computer simulations, the exponent t has been found to lie within $1.9 \leq t \leq 2.0$ in three dimensions [Derrida *et al*, 1983]. Using scaling arguments, the conductivity exponent t can be related to the fracton dimensionality $\tilde{d}$ to give

$$\tilde{d}_{Born} = \frac{2(d\nu - \beta)}{t - \beta + 2\nu} \quad . \qquad \text{(II-30)}$$

Alexander and Orbach [1982] conjectured that $\tilde{d}_{Born} = \frac{4}{3}$ for all dimensions, reasoned from Equation (II-30) using the best estimates of t , ν and β for $d \geq 2$.

§II: 3.2 — Bond-Bending Model

In this model, the bonds of the percolating system are *not* described as a set of "three dimensional springs". Instead, the energy of the network is assumed to arise from a spring component along the axis of the bond plus an energy term arising from a change in angle between two bonds. This intuitively more appealing model is expressed in Equation (II-31) (see Kantor and Webman [1984], and references within):

$$H = \frac{Q}{4a^2} \sum_{\substack{i,j \\ (nn)}} K_{ij}(\underline{u}_i - \underline{u}_j)_{\parallel}^2 + \frac{G}{4} \sum_{\substack{ijk \\ (j,k\ nn \\ of\ i)}} K_{ij}K_{ik}\,\delta\phi_{ijk}^2 \qquad \text{(II-31)}$$

where K_{ij} and K_{ik} are the same random variables as in §II:3.1 , G and Q are local elastic constants, a is the lattice spacing, and $\delta\phi_{ijk}$ is the change in angle between bonds (ij) and (ik) as shown in Figure II-2a . The first term of this equation corresponds to the first term of Equation (II-28) .

Kantor and Webman [1984] have performed calculations using this model. The percolating network is considered to consist of completely rigid, multiply connected clusters joined together by relatively soft, singly connected thin channels, as schematically represented in Figure II-2b . All of the bond-bending and bond-stretching is considered to occur only at these thin channels which join the rigid clusters. This means that the stiffness of the system is overestimated for all values of p-p_c and the resultant calculated value of τ is a lower bound. They also made the approximation that near p_c , the elasticity

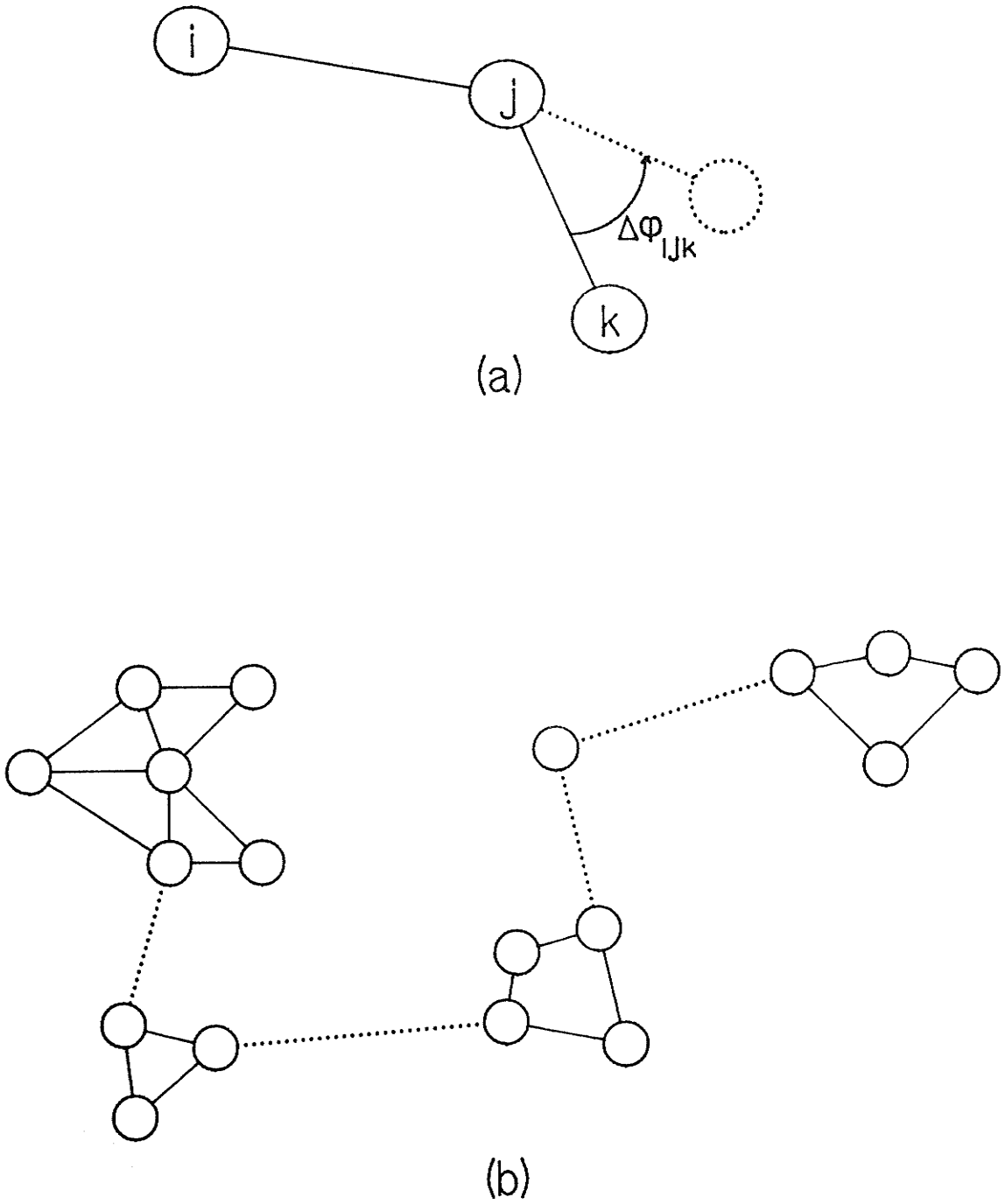

Figure II-2

(a) The change of angle between particles in the bond-bending model.

(b) Schematic of multiply connected clusters (——) joined by relatively soft, singly-connected channels (——).

is dominated by weak bond-bending forces in singly connected links; thus the first term of Equation (II-31) was ignored their analysis. With the added assumption that the singly connected bonds are randomly distributed over the entire region of size ξ , they obtained

$$\tau > d\nu + 1 \qquad \text{(II-32)}$$

where τ is the critical exponent of the macroscopic elastic moduli. For three dimensions, $d = 3$ and $\nu = 0.88$ so that $\tau > 3.55$. This is in contrast to the conductivity exponent for which $1.9 < t < 2.0$ in three dimensions. These results predict that the elasticity of a percolating system with bond-bending belongs to a different universality class than conductivity and is described by a different critical exponent.

With the assumption that the softness of a region is determined by its singly connected bonds, and that $N_s(L) \propto L^{-1/\nu}$, where $N_s(L)$ is the number of single bonds at length scale L [Pike and Stanley, 1981; Coniglio, 1981] , Webman and Grest [1985] calculated that for the bond-bending model, the fracton dimensionality can be expressed as

$$\tilde{d}_{b-b} = \frac{2(d\nu - \beta)}{(d + 2)\nu + 1 - \beta} \ . \qquad \text{(II-33)}$$

Note that this result states that $\tilde{d}_{b-b}$ is dependent upon the Euclidean dimension and the critical static exponents, but not τ. This contrasts Equation (II-30) for the scalar elasticity model which has a dependence upon the conductivity exponent t ($=\tau_{Born}$). In three dimensions, with $\nu = 0.88$ and $\beta = 0.44$, Equation (II-33) predicts $\tilde{d}_{b-b} = 0.89$ as opposed to the scalar elasticity model which states that $\tilde{d}_{Born} = 1.33$.

CHAPTER III: SAMPLE PREPARATION

In order to investigate the theoretical ideas described in Chapter II , a series of samples were created. It was important for these samples to have good homogeneity at long length scales (when $L > \xi$), and it was necessary for the set to have a large span of packing fractions, from $f \sim 0.5$ down to the percolation threshold f_c . In order to approach the crossover region (§II:2.2) with the frequency range available (1 to 20 MHz), the size of the particles used were considerably smaller than particles (or effective particles due to particle clustering) used in previous work [Maliepaard *et al*, 1985; Page and McCulloch, 1986]. It was necessary to create each sample of the set under identical conditions in order to meaningfully compare the data obtained from each sample. The final method and conditions used to create this set are described in §III:1 . In §III:2 , the efforts contributing to the selection of these conditions are described in detail.

§III: 1 — SAMPLE PREPARATION METHOD

Previous methods of sample preparation [Maliepaard *et al*, 1985; Page and McCulloch, 1986] involved pressing a single powdered substance to a calculated thickness in order to obtain the desired packing fraction. The limitations of this method included a restricted lower range of sample density that could be obtained, as well as lack of control over the sample homogeneity. This work addresses these limitations by introducing a second powdered material to the sample.

Two different materials of the same particle size were mixed together. One of the materials was transitory; it was removed from the sample after the second material was sintered. However, the presence of this transitory material made the distribution of the second material more homogeneous. Also, if relatively large quantities of the transitory material were added (but later removed), the packing fraction of the other material could be made as low as desired, even below percolation threshold. Thus the range of sample porosity was greatly expanded.

A set of five samples of different packing fractions were created. This involved mixing glass beads with nickel powder (which had similar grain size as the beads), pressing the mixture into a pellet, sintering the glass, and then immersing the sample in acid until the nickel particles dissolved.

§III: 1.1 — The Materials

The samples were created from (2.1 ± 0.5) μm glass microspheres from Duke Scientific and (2.5 to 3.0) μm nickel powder from Alfa Products. A scanning electron microscope (SEM) was used to obtain pictures of the samples. A micrograph of these two mixed but otherwise untreated materials is found in Figure III-1. The two particle types are visually distinguishable in this micrograph since the surface features of the nickel particles are rough and pitted, while the glass beads are nearly perfect spheres and have very smooth, unblemished surfaces. The nickel powder has a metal purity of 99.9% and a total purity of 99% . The composition of the glass varied from batch to batch, but the typical percentage of the constituents stated by the company are shown in Table III-1 . The density of nickel is 8.90 g/cm^3 [Weast, 1985] and the density of the glass was found to be (2.475 ± 0.015) g/cm (cf. §IV:2.3).

Table III-1

Typical Constituents of the Untreated Glass Beads

SiO_2	72.5 %	
Na_2O	13.7 %	
CaO	9.7 %	
MgO	3.3 %	
Al_2O_3	0.4 %	
Fe_xO_y	0.2 %	(assorted types)
K_2O	0.1 %	

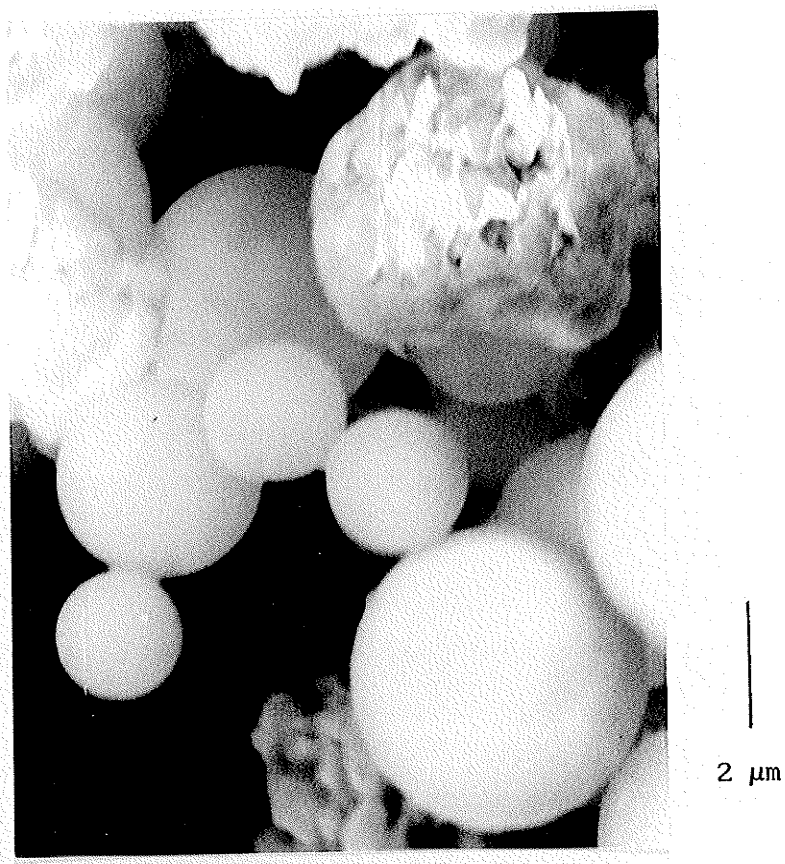

Figure III-1: A mixture of the two materials used for the sample preparation can be seen in this SEM micrograph. An example of a rough, pitted nickel particle can be seen in the upper righthand corner, and a smooth sphere of glass in the lower righthand corner.

§III: 1.2 — Forming the Samples into a Pellet

Using a Gram-Atic balance from Fisher Scientific, the appropriate amounts of nickel and glass were weighed. The materials were then poured into a plastic tube and a glass bead was inserted to aid the mixing process. The tube was placed into a Spex Industries Incorporated Model 8000 shaking machine and mixed for thirty minutes. The mixture coated the inner surface of the mixing tube so that a clean paintbrush was used to remove the mixture from the container and to deposit it on a clean piece of aluminum foil.

The mixture was poured into an inverted 13 mm Specac mold. In order to make the sample equally dense in all regions, the powder in the mold was continually redistributed with a flat metal bar by alternately sweeping across the sample surface followed by packing any resultant loose powder back into the sample. Every time the loose powder was completely packed into the sample, the mold depth was slightly decreased by removing a piece of paper that helped to support the base of the mold. The sweeping and packing process was repeated until the sample was sufficiently dense everywhere that the loose powder could just barely be compacted back into the body of the sample. The aim of this process was to relocate portions of the mixture until the density variation throughout the sample was minimized.

The powder was then raised out of the mold slightly. The top edge of the mold was tapered and caused a lip to form on a sample. The lip was removed using a bristle of a brush so that the inhomogeneities along the sample edges were minimized. The mixture was lowered into the mold and the second pressing pellet was set on top. A hydraulic press was

used to squeeze each sample under 2500 kg of pressure for about two minutes, after which the sample was carefully removed from the mold. At this stage, the sample was somewhat fragile and could not readily be handled without danger of breaking; the samples seemed to retain their shape because the rough surface structure of the nickel particles allowed them to link together. After the thickness of the sample was measured using a travelling microscope, it was ready for sintering.

§III: 1.3 — Sintering the Samples

The sintering of the samples was done in air at atmospheric pressure. Each sample was placed in a cylindrical stainless steel container during sintering in order to limit thermal fluctuations due to convection currents. The pellet was set flat on the base to allow good thermal contact between sample and container, and their temperature was measured with an alumel-chromel thermocouple that was inserted in a hole in the side of the base. Each lead of thermocouple was soldered to a copper wire (which was connected to a voltmeter). The two junctions were immersed in oil which in turn were immersed in an ice bath. This method resulted in a good, reproducible measurement of the temperature of the base and sample.

The sample holder was slowly inserted into a 3.7 cm diameter quartz tube whose closed end sat at thermal equilibrium in a furnace. The holder was inserted such that the temperature increased at a rate of about 30°C/min until it reached 648°C. The thermocouple voltage was

monitored with a Hewlett Packard 680 Strip Chart Recorder and a Keithley 177 Microvolt Digital Multimeter. Once the target temperature was attained, the measured temperature of the sample varied less than half a degree; it was necessary to occasionally reposition the sample holder in the quartz tube to compensate for slow furnace temperature oscillations. From a previous furnace temperature gradient measurement, the temperature from one edge of the sample to the other was known to be less than $0.1^{\circ}C$. After (63 ± 2) minutes the sample holder was removed at a rate similar to its insertion. Thus each of the samples were given the same reproducible heating treatment. An example of the final degree of sintering can be seen in Figure 2 of §III:2.1 .

§III: 1.4 — Polishing the Samples

For each sample, it was important to have its two faces both flat and parallel to one another. In order to achieve the parallelism, a thin steel disk whose two faces had been machined parallel to within a few thousandths of an inch tolerance was obtained. The sample was mounted in the centre of the disk and attained the parallelism of the disk after the polishing process was completed. The resulting variation in thickness over the 13 mm diameter of a sample was typically ±4 μm.

In the centre of the disk, a hole was machined to be the same diameter as the samples. If the hole was slightly larger than one of the samples, the diameter of the hole was reduced by fastening a brass foil strip with epoxy on the perimeter of the hole. When the hole was

the proper size, the sample was inserted and mounted in the middle of the disk using #70C Lakeside Brand thermoplastic cement. This yellow wax was soaked into the sample in order to help support the internal sample structure during the polishing process. The thickness of the disk was chosen such that both faces of the sample slightly protruded from the steel disk, and a cylindrical disk holder was used to support the steel disk so that it remained as flat as possible while the disk and the sample were polished.

The disk was first coarsely polished with 600A Tri-M-Ite sandpaper that was fastened to a flat block of aluminum. After the surface of a sample attained a uniform finish from the sanding, the next stage of polishing was performed using 6 μm Hyprez diamond compound. The paste was spread on a clean, flat steel plate and the disk was rubbed against it in a circular motion. When the finish on the sample and disk were uniform and the sample appeared to be flat, this process was repeated using 3 μm and 1 μm diamond pastes. A separate flat steel plate was used for each grade of paste in order to minimize contamination from a coarser grade of diamond paste. The final stage of polishing was done using a Hyprocel polishing cloth.

During each stage of polishing, the paste became thick due to the material that had been abraded from the disk. It was thus necessary to polish the sample with the same grade of paste several times and to clean the plate, disk, and sample before each application of diamond paste. It was found that the fastest way of removing the majority of the paste from everything was to use a generous amount of mineral oil, and the easiest way of removing the resulting oil residue from the polishing plate was to use a generous amount of acetone poured directly

onto the plate. A solvent could not be poured onto the polishing disk because the yellow cement (which held the sample fast) was soluble in toluene, acetone, and methanol. The residue on the disk was wiped with a tissue wet with toluene, and the sample itself was wiped only with mineral oil and distilled water. Between each different grade of polish, the sample was cleaned as well as possible and then it was lightly wiped with a very small amount of toluene. This was done to reduce the amount of contamination between the polishing plates for the different grades of polish. After the sample was polished, it was soaked in toluene, acetone, and then methanol in an attempt to free it of all wax and oils. Before being soaked in each solvent, the sample was dried in order to permit each solvent to completely penetrate the sample.

The degree of flatness of a face of a sample could be judged by placing an optical flat over the sample and observing the resultant interference pattern. This pattern was most easily observed when a monochromatic light source (Unilamp from Midwest Scientific Company) was used to illuminate a sample. The more parallel the interference fringes, the more flat was the surface of a sample. A typical deviation from parallelism was about 5 interference fringes (2.5 wavelengths) of green light which corresponds to about 1.3 μm . This variation in flatness of the sample face is sufficiently small to have a negligible effect on the measurements performed.

§III: 1.5 — Etching the Samples

After the samples were polished, the nickel had to be removed from the sample by dissolving it in acid. The sample was placed on a Teflon holder in a Pyrex beaker, and the beaker was then filled with a 1:1 (by volume) HNO_3:H_2O mixture. The reaction rate of oxidated nickel increases with temperature; thus the beaker was warmed to ~70°C on an electric element with the power controlled by a Variac power supply. Loss of acid via evaporation was reduced by placing a watchglass on the beaker to condense the acid vapor; the entire etching process was performed under a fume hood.

It was necessary to leave a sample in the hot acid bath for approximately one week in order to leech out most of the nickel. The required length of time was due to the limitations of circulation of the acid through a sample; fresh acid could not readily circulate to the nickel that remained in a sample due to the small pore size of the sample. Although the reaction occurred faster in heated acid, care had to be taken not to allow the acid to get too hot since a gas bubble could form under a sample and possibly damage it. This was not a difficulty for the sturdier samples, but it proved to be a danger to the more fragile samples of lower glass occupied volume fractions.

Once the nickel was dissolved, the Teflon holder containing the sample was removed from the acid bath using stainless steel tweezers and placed in a distilled water bath to dilute the acid. After an hour or more it was removed from the water and dried in an oven. The preparation stage was complete; the sample was ready for acoustic measurements.

§III: 2 — RATIONALE FOR THE SAMPLE PREPARATION PROCEDURE

The method of sample preparation described in §III:1 was achieved after consideration of the effect of numerous factors, such as the sintering conditions, the sample purity, changes in sample composition, etching and rinsing time, and surface fractures. The rationale of the chosen conditions is described in the following subsections.

§III: 2.1 — Sintering Conditions

When initially preparing a sample, different combinations of times and temperatures were attempted in order to find conditions which would result in an acceptable degree of sintering. Examples of properly sintered and oversintered samples are presented in Figure III-2 . A sample was considered to be properly sintered if its glass beads retained their initial shape and size (Figure III-2a); the bonds between the particles were allowed to grow sufficiently large that the entire sample would be fairly robust. An oversintered sample, in contrast, consisted of conglomerations of several particles that had barely any trace of their initial shape (Figure III-2b) . The conditions under which the samples of Figure III-2 were sintered were rather different so that the difference of the degree of sintering is not unexpected.

The sensitivity of the samples to sintering conditions can be seen in Figure III-3 . For these micrographs, the nickel had not been

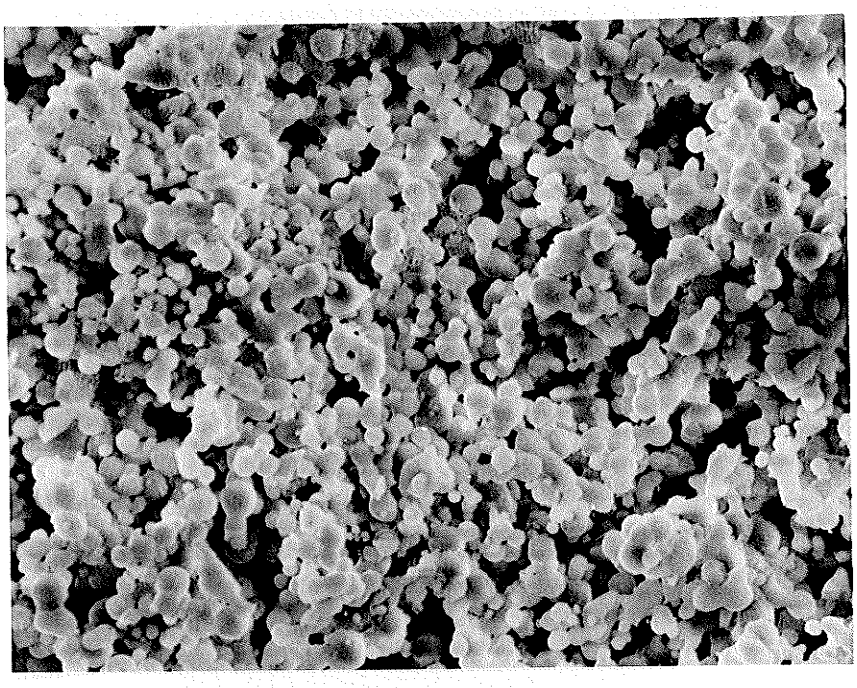

(a) An example of properly sintered sample (645°C, ~1 hour)

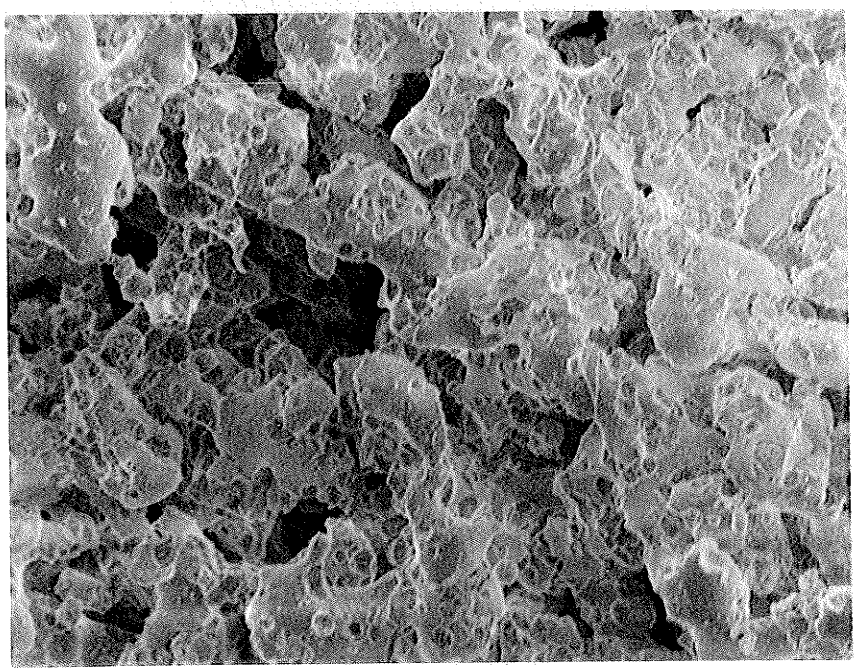

(b) An example of an oversintered sample (720°C, ~2 hours)

Figure III-2: (a) and (b) are micrographs of acid etched glass bead sinters after different heat treatments.

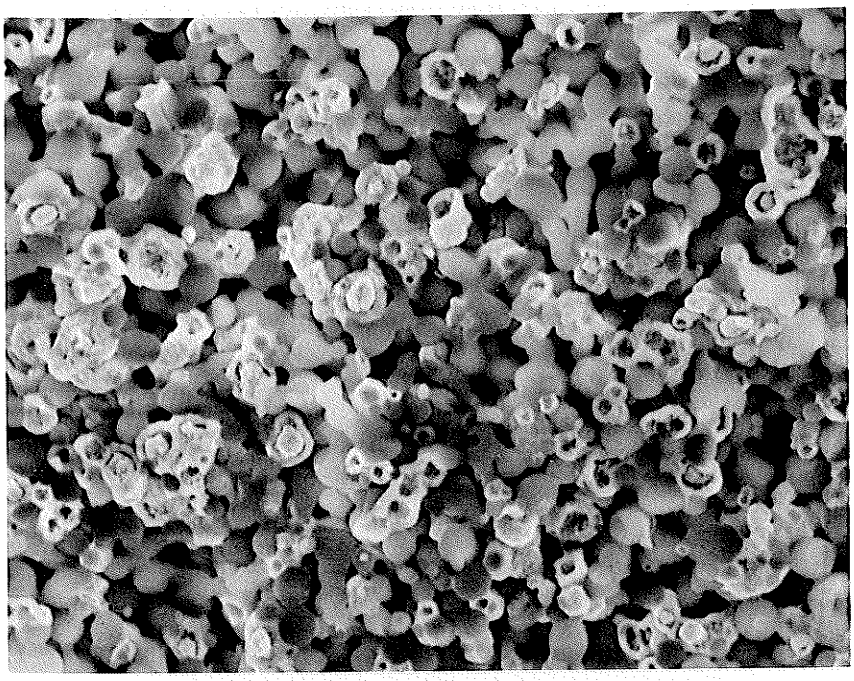

20 μm

(a) Sintering conditions: (644.5 ± 0.5)°C , for 1 hour

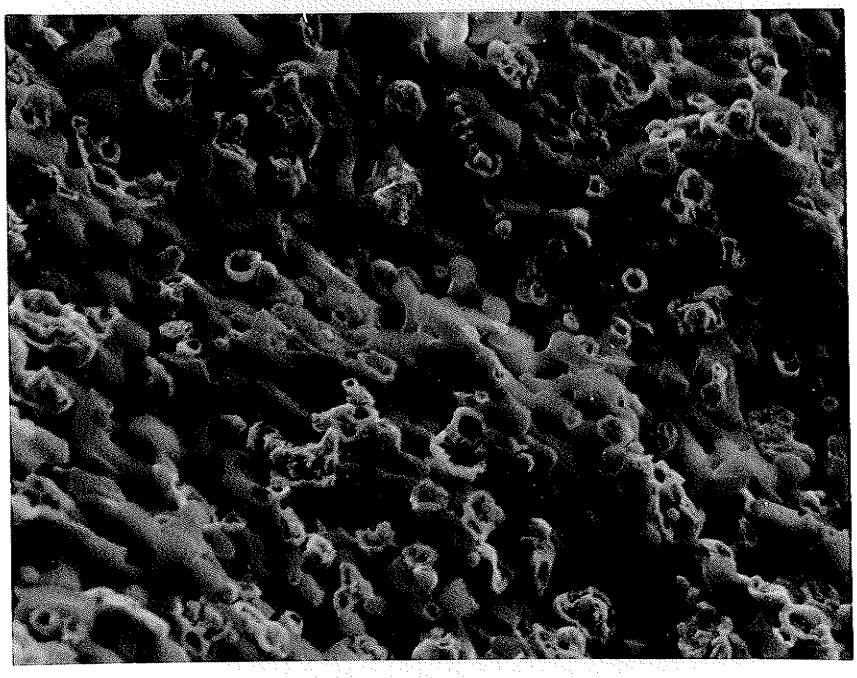

20 μm

(b) Sintering conditions: (650.0 ± 0.5)°C , for 1 hour

Figure III-3: The temperature sensitivity of the sintering of the glass can be seen from these micrographs. Figures (a) and (b) are pieces of the same nickel/glass sample; the rough nickel particles appear as a lighter shade of grey than the smooth glass beads.

etched from the samples, and is seen as the lighter shaded, rougher material. Two pieces of the same sample were heated for about the same period of time, but the piece seen in Figure (a) was sintered at a temperature about 5°C lower than that of Figure (b) . The piece of the sample in Figure (b) can be seen to be noticeably more sintered than that of Figure (a) , and demonstrates the necessity of reproducible temperature conditions for reproducible sample structure.

It was assumed there would be many time and temperature combinations for which an acceptable degree of sintering could be achieved because if the temperature was increased, the time of sintering could be decreased. However in addition to these two variables, it was found that other factors had to be considered in order to choose the conditions that were best for sample preparation.

When sintering the sample, it was necessary to have a sufficient time of constant temperature so that the periods of warming and cooling the sample would not be critical to the degree of sintering. The reason for this was because it was not as easy to warm and cool a sample at a reproducible rate as it was to maintain a constant temperature. The rate of heating and cooling was limited to about 30°C/min in order to reduce potential problems involved with differential thermal expansion of the nickel and glass. Twenty to thirty minutes were required to heat the sample to the target temperature, but in only about the final five minutes (95% of the target temperature) was the temperature sufficiently hot to cause any significant sintering effect. Thus it was decided that the target temperature was to be maintained for a minimum of 45 minutes in order to heat the samples in a reproducible manner.

There were two other factors that were considered in determining the sintering conditions for the samples. First, the nickel powder had a contaminant and the most effective method of purifying it was through heating the entire sample in air at atmospheric pressure. This factor encouraged maximizing the sintering time. However, it was found that the properties of the glass were unsuitably altered with prolonged exposure to high heat. The balance of these two constraints eventually led to sintering conditions of (62 ± 2) minutes at a temperature of (648.5 ± 0.5)°C in air at atmospheric pressure.

Information about the nickel contamination is listed in §III:2.1a, and data outlining the changes in the glass composition are found in §III:2.1b .

§III: 2.1a — Purity of Nickel

With some preliminary samples, it was found that when the nickel/glass sample was sintered under vacuum, and then later etched in acid, a dark material remained in the sinter. As stated in §III:1.1 , the purity of the nickel was 99% . In an attempt to identify the contaminants, some etched samples were cut so that their cross sections could be studied under a scanning electron microscope (SEM) which had an EDAX system to analyze the emitted x-rays (cf. Appendix B). Spectra of the interior of samples, both heated and unheated, did not reveal any unexpected element. This means that the contaminant has an atomic number less than 11 because the detection system was unable to detect elements with a lower atomic number. The only unusual aspects of the

etched contaminated samples were that they were oversintered and that a fair amount of nickel was detected even though the sample had been immersed in acid. It is possible either that the detected nickel had been isolated from the acid by the oversintered glass beads or that the contaminant was an unreactive nickel compound.

A check for unreactive contaminants in the nickel powder was investigated by dissolving untreated nickel powder in nitric acid. The nickel reacted quickly, but there remained a dark substance that would not dissolve. Subsequent attempts to eliminate this contaminant with a ammonia or a variety of acids failed. The fact that the contaminant was black, nonreactive, and had an atomic number less than 11 indicated that it was probably carbon (or possibly Ni_3C). Because carbon is so unreactive, it was decided that the best way to remove the contaminant was to heat the nickel powder in air to oxidize the carbon. Nickel powder alone was placed in the furnace for about 12 hours at 700°C in air at room pressure. The powder mass before and after heating was recorded, and it was calculated that the nickel had virtually all oxidized to NiO. When the powder was placed in hot nitric acid it dissolved more slowly than nickel, but it did dissolve completely: no visible contaminant remained. Thus heating the nickel in air was an effective way to eliminate the contaminant. However, under these conditions the preheated nickel sintered and the resultant nickel particle size was no longer compatible to that of the glass beads. It is possible that heating conditions exist such that the contaminant can be eliminated without significantly sintering the nickel, but finding these conditions was not attempted. The problem was avoided by heating

PAGINATION ERROR.

TEXT COMPLETE.

ERREUR DE PAGINATION.

LE TEXTE EST COMPLET.

NATIONAL LIBRARY OF CANADA.

CANADIAN THESES SERVICE.

BIBLIOTHEQUE NATIONALE DU CANADA.

SERVICE DES THESES CANADIENNES.

Table III-2

Composition of Glass Beads Before and After Heating

	Untreated Glass		Heated Glass*
	Second Batch	First Batch	
Si	(72.8 ± 0.2)%	(75.8 ± 0.3)%	(72.0 ± 0.2)%
Ca	(12.6 ± 0.1)%	(13.2 ± 0.2)%	(5.6 ± 0.1)%
Na	(14.7 ± 0.3)%	(11.1 ± 0.3)%	(22.4 ± 0.3)%

*The glass was heated for 2 hours at 685°C.

The proportion of constituents are listed in terms of *atomic* percentage.

case, nickel tends to absorb the x-rays emitted by the sodium more than the x-rays emitted by the silicon. The analysis program used to compensate for this assumes that the sample is homogeneous on an atomic scale, but the samples studied are made of particles with a size on the order of a micron; therefore the sodium x-rays are not absorbed nearly as much as if the materials were atomically homogeneous. The analysis program overcompensates for the supposedly highly absorbed sodium x-rays and results in a distortion of the actual spectra gathered. Although the apparent constituent proportions of the glass are different with the presence of nickel, qualitative information can still be obtained from these spectra. In Table III-3 the spectra of the interior of two samples are compared, both with the same glass packing fraction of 0.27 . The spectra of the two samples are seen to be consistent with each other, although there appears to be as much sodium as there is silicon.

Table III-3

MIXTURE BEFORE HEATING

	#7	#13
Si	(17.9 ± 0.2) %	(16.4 ± 0.2) %
Na	(17.4 ± 0.6) %	(17.6 ± 0.6) %
Ca	(2.0 ± 0.1) %	(2.2 ± 0.1) %
Ni	(62.7 ± 0.2) %	(63.4 ± 0.2) %

Table III-4

MIXTURE HEATED, NOT ETCHED

	#3 Oversintered*	#18 Sintered†
Si	(19.9 ± 0.6) %	(19.3 ± 0.1) %
Na	(20.9 ± 2.0) %	(20.0 ± 0.5) %
Ca	(1.9 ± 0.1) %	(2.1 ± 0.1) %
Ni	(57.3 ± 0.7) %	(58.7 ± 0.2) %

* 30 min. at 710°C † 60 min. at 645°C

The compositions of samples after heating are seen in Table III-4 . Two different samples are listed in this table, but they both have a glass packing fraction of 0.27 . Column 1 of this table is the spectrum of an oversintered sample, and column 2 is the spectrum of a sample that was sintered approximately to the level desired. The spectra are quite similar to one another. The heated samples listed in

Table III-4 have spectra similar to the unheated samples of Table III-3 , except that the detected sodium and silicon levels have both increased relative to the other constituents. Although the amount of silicon and sodium in these samples is not known exactly due to the influence of the nickel, it is still possible to ascertain that sintering does not reduce the amount of sodium detected. If anything, the amount has increased. However, as seen in Table III-5 , the spectra of sintered (#14) and oversintered (#5, 6 and 13) samples differ after being etched in acid. The interior of the sintered sample has very little nickel remaining, but the interior of the oversintered samples has more. This is an indication that when a sample is oversintered, some nickel particles are probably surrounded by glass and are isolated from the acid.

It is also appears as though the sodium constituent of the glass beads does dissolve in the nitric acid, as studies of glasses have indicated (see for example, Paul [1982] Figures 4.2 and 4.4). It had been earlier noted from Table III-2 that heating the glass beads increased the concentration of sodium on the surface of the glass, but as seen in Table III-5 , the etched beads have less sodium than the untreated beads. There is very little sodium remaining in sample #6 , the sample that had been sintered for a very long period of time and therefore would be expected to have the most sodium on the surface before etching. In contrast, the spectra of samples #13 and 14 , the two least sintered samples, show that the samples have most of their sodium remaining, although it is somewhat reduced. The level of sodium in sample #5 seems anomalous, but this might be explained by a

Table III-5

HEATED and ETCHED

Sample #14 Sintered: 1hr, 640 C°	
Ni	(0.9 ± 0.1) %
Glass	(99.1 ± 0.3) %

Sample #5 Oversintered: 9 hrs, 685°C	
Ni	(6.7 ± 0.2) %
Glass	(93.3 ± 0.6) %

Glass constituents (renormalized to 100 %)	
Si	(77.6 ± 0.2) %
Ca	(14.1 ± 0.1) %
Na	(8.3 ± 0.2) %

Glass constituents (renormalized to 100 %)	
Si	(76.7 ± 0.3) %
Ca	(10.3 ± 0.1) %
Na	(13.0 ± 0.5) %

Sample #6 Oversintered: 112 h, 655°C	
Ni	(2.5 ± 0.2) %
Glass	(97.5 ± 0.6) %

Sample #13 Oversintered:8.75 h, 680°C	
Ni	(5.1 ± 0.1) %
Glass	(94.9 ± 0.5) %

Glass constituents (renormalized to 100 %)	
Si	(89.5 ± 0.4) %
Ca	(9.2 ± 0.2) %
Na	(1.2 ± 0.4) %

Glass constituents (renormalized to 100 %)	
Si	(77.4 ± 0.3) %
Ca	(14.1 ± 0.1) %
Na	(8.4 ± 0.4) %

measurement error due to the larger amount of residual nickel in this sample. As previously described, the presence of nickel tends to increase the calculated amount of sodium detected with respect to the other constituents. Hence, the spectra of Table III-5 support the idea that the surface sodium was etched from the the glass beads. Since this is a surface effect, all of the sinter bonds would be weakened by the etching and it provides a reasonable explanation of why the over-sintered samples were fragile. Hence it was necessary to sinter the samples in as short a time as possible in order to reduce the change in constituent proportions and hence to reduce the amount of damage to the glass due to etching.

In order to further support the idea that heating changed the glass composition, three specimens were heated simultaneously. Some previously untreated glass beads were heated (column 3 of Table III-2) along with pieces of oversintered etched samples from both #5 and 6 . The heat treatment caused the previously unheated glass beads to completely lose their shape and form a puddle, whereas the appearance of the over-sintered samples did not change. The particles of the oversintered samples retained their basic shape even after being heated for 16 hours at 730°C (although some further sintering did occur). Since sodium is added to glasses to reduce the melting temperature (see for example, [Paul, 1982] or [McMillan, 1964]), the detected reduction of sodium in the oversintered samples is consistent with an increased melting temperature of the etched glass. It was desired to keep the properties of the glass constant for the purpose of having reproducible sintering conditions; thus the change in glass composition due to extended heat treatment of the samples was unacceptable.

§III: 2.2 — Etching the Samples

The rate that nickel or its oxide dissolves in nitric acid is much greater in heated acid than room temperature acid. This increased rate was necessary in order to remove the nickel particles from the samples in a reasonable amount of time. Although nickel dissolves fast in nitric acid, its oxide dissolves much more slowly. This slow reaction, compounded with the fact that the circulation of the acid within a sample was low due to the fine pore size of the sample, caused the interior of the sample to etch more slowly than the exterior.

The time required to etch the oxidized nickel from a sample was determined from preliminary measurements. An oversintered sample ($f_{glass} = 0.36$) was broken into two pieces; one piece was etched for 143 hours (Table III-6a) while the other piece was etched for a much shorter time of 47 hours (Table III-6b) . The first obvious difference between these two sets of spectra is that there is a much greater amount of nickel (oxide) remaining in the sample that was etched for a shorter period of time. In Table III-6b , there is also a noticeable difference between the amount of nickel detected at the central and the outer region while there is no such distinction in Table III-6a . From these observations, we can see that the longer etching time decreased the amount of nickel detected. Using the values from Table III-6a and Equation (B-1) from Appendix B , we see that the volume occupied by the nickel oxide is about 2% of the material in the sample. The packing fraction of the glass is about 0.36 , so that $f_{NiO} \cong 0.007$ after etching.

Table III-6a

T_{ACID} = **143 hours** T_{RINSE} = **117 hours**

	Centre	Edge
Si	(89.9 ± 0.3) %	(90.2 ± 0.3) %
Ca	(5.9 ± 0.1) %	(5.7 ± 0.1) %
Ni	(4.2 ± 0.1) %	(4.2 ± 0.1) %

f_{glass} = 0.36

Table III-6b

T_{ACID} = **46 hours** T_{RINSE} = **150 hours**

	Centre	Edge
Si	(76.5 ± 0.3) %	(78.4 ± 0.3) %
Ca	(12.2 ± 0.1) %	(11.8 ± 0.1) %
Ni	(11.9 ± 0.1) %	(9.8 ± 0.1) %

f_{glass} = 0.36

Table III-6c

T_{ACID} = **143 hours** T_{RINSE} = **1.5 hours**

	Centre	Edge
Si	(90.7 ± 0.3) %	(90.4 ± 0.3) %
Ca	(5.6 ± 0.1) %	(6.0 ± 0.1) %
Ni	(3.4 ± 0.1) %	(3.6 ± 0.1) %

f_{glass} = 0.25

It was possible that an even longer etching time would have further decreased the amount of nickel detected, but this had to be balanced with other factors. The main point of concern was that the extra time required to achieve a significant reward in nickel loss was an unacceptably long period of time. Additionally, as previously mentioned in §III:2.1a , it was possible that this detected nickel was either Ni_3C , or else nickel completely surrounded by glass so that extra etching time would have been fruitless. A third consideration was that further leaching would extract more sodium from the glass and possibly weaken it further.

It was also possible that nickel ions in solution were deposited in the sample after the sample was dried. In order to reduce this potential problem, the sample was placed in a distilled water bath immediately after it was etched in order to greatly dilute the acid remaining in the sample. To determine the effectiveness of the rinsing, one oversintered sample (f_{SiO}= 0.36) was etched in acid for a relatively long period of time (143 hours) and rinsed for a relatively long time (117 hours). This was compared with a sample (f_{SiO}= 0.25) that had been sintered and etched for the same period of time, but rinsed in distilled water for only $1\frac{1}{2}$ hours. The gathered spectra correspond to Tables III-6a and c respectively and show that the considerably longer period of rinsing resulted in only a very small difference in the detected nickel. It is also possible that the small reduction of nickel was not due to the extended rinsing time but to the better circulation of acid and rinse water in the more porous sample. Whether this was the case or not, the difference in nickel content is not large and did not warrant the extra time.

§III: 2.3 — Measurement of Glass Density

The density of the glass microspheres were known to be (2.45 ± 0.05)g/cm^3 according to the information supplied from Duke Scientific. In order to reduce the uncertainty of the density of the glass, the following method was prepared and performed by Gary Cosby. A series of liquids of carefully measured densities were prepared. The two chemicals used to prepare this series were carbon tetrachloride (CCl_4, also known as tetrachloromethane) and tetrabromoethane ($Br_2CHCHBr_2$). The densities of these chemicals at 20°C are [Weast, 1989]

$$\rho_B = \rho_{Br_2CHCHBr_2} = 2.9656 \text{ g/cm}^3$$

$$\rho_C = \rho_{CCl_4} = 1.5940 \text{ g/cm}^3 \quad .$$

A mixture of the two liquids resulted in a liquid whose density was intermediate to the two constituents. The density of the mixture can be calculated by

$$\rho_{mixture} = (m_B + m_C)\left(\frac{m_B}{\rho_B} + \frac{m_C}{\rho_C}\right)^{-1} \qquad \text{(III-4)}$$

where m_B is the mass of the tetrabromoethane

and m_C is the mass of the carbon tetrachloride.

In order to attain a mixture of a certain density ρ, the appropriate masses of the constituents had to be combined. For a given mass of tetrabromoethane, the required mass of CCl_4 was calculated by

$$m_C = m_B \left(\frac{1 - \frac{\rho}{\rho_B}}{\frac{\rho}{\rho_C} - 1} \right) . \qquad \text{(III-5)}$$

The vials in which the series of density mixtures were contained had to be sealed with vacuum grease because CCl_4 is a very volatile liquid: the density of the mixtures otherwise increased with time. The glass beads were placed in each mixture and left overnight to reach equilibrium. For the mixtures whose densities were greater than that of the glass beads, the beads floated; for the mixtures whose densities were less than that of the glass beads, the beads sank. The closer the density of the mixture to that of the glass beads, the less defined the point of floating and sinking became. Through this method, the density of the glass microspheres was found to be (2.475 ± 0.015) gm/cm^3, a considerably more accurate value than the number supplied by the manufacturer.

§III: 2.4 — Homogeneity Improvement

An investigation was done to test if the homogeneity of the sample at long length scales could be improved by grinding the sample [Lee *et al*, 1985]. After a nickel/glass mixture was shaken, levelled, and pressed, the sample was placed in a mortar and broken with a pestle. The sample was ground for about ten minutes and then regathered (using a magnet and steel rod to reduce the loss of material), and the pellet-making process was repeated. The entire grinding process was repeated

numerous times and a small piece of the sample was removed before each grinding. Figure III-4 consists of four SEM micrographs of the sample at various stages of grinding. Initially, after mixing the glass beads and nickel powder (a), nickel clusters of up to ~10 μm long can be seen; the nickel particles were jagged and tended to stick together somewhat. Grinding the sample smoothed the jagged edges of the nickel particles (b , two grindings), and the homogeneity was most improved after the fourth grinding (c): glass beads can be seen to be imbedded in the smoothed, partially broken nickel clusters. Further grinding tended to break the nickel particles into smaller, irregular pieces (d) . Before sintering, the ground pellets were more fragile than unground pellets, presumably due to the change of the surface features of the nickel particles. In order to test the improvement of the homogeneity through grinding, it would be necessary to create two similar sets of samples, one set ground, the other not. Time did not permit this investigation and only the latter set was created.

When the grinding technique was attempted with a NiO/glass mixture, the particle size distribution and shape of the NiO were considerably degraded after only one grinding. The micron-sized particles were frequently seen to have relatively sharp edges and there was a multitude of submicron particles observed. These observations imply that the oxidized particles were brittle; the micron-sized particles broke instead of deforming, and the submicron particles probably originated from the rough surface features of the virgin nickel particles. Also, the oxidized nickel could not be gathered using a magnet so that a fair amount of the mixture was lost after each stage of grinding. Thus

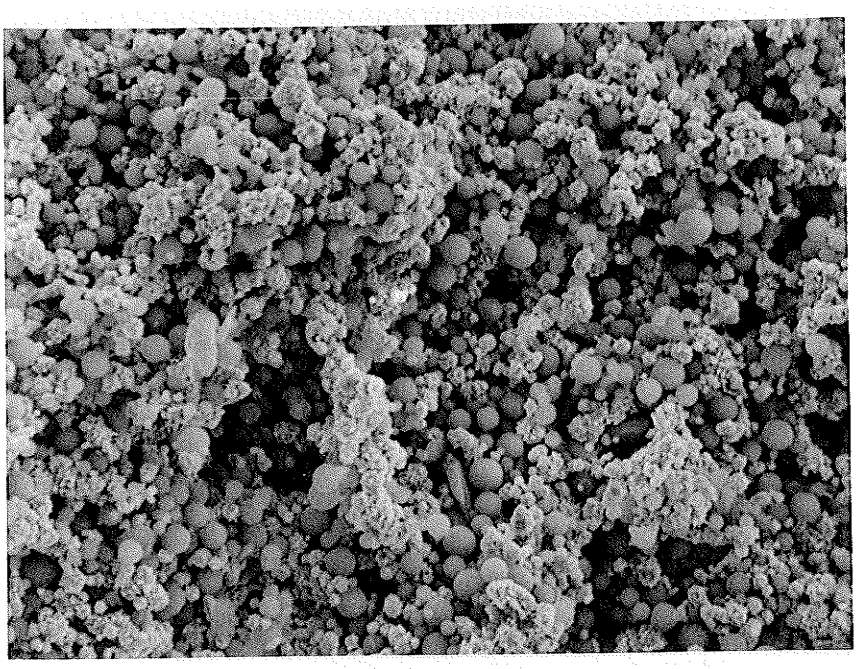

20 μm

(a) No grinding

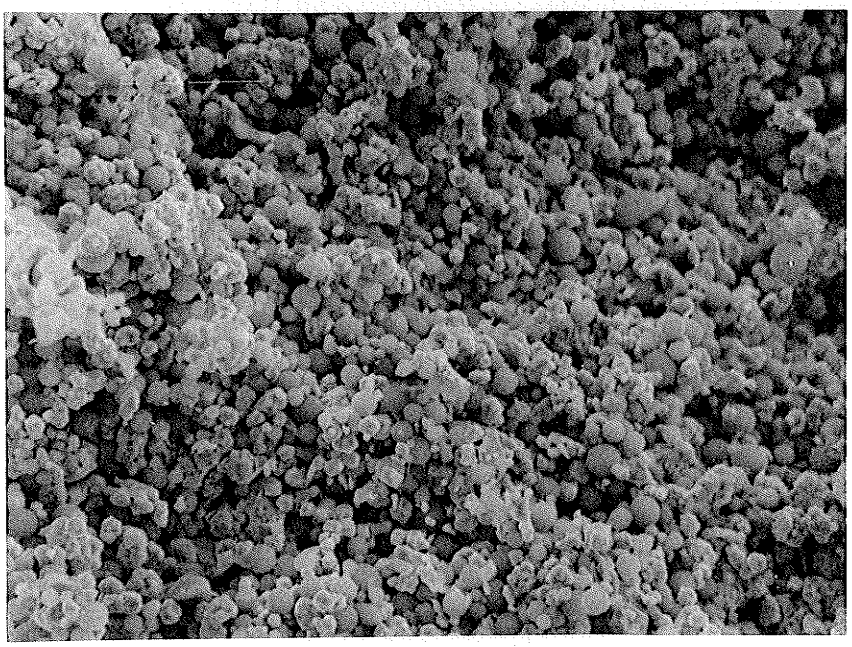

20 μm

(b) 2 grindings

Figure III-4: The effect of grinding on sample homogeneity is seen in figures (a)-(d). Chains of nickel powder up to about 10 μm long can be seen in (a). In (b), the nickel powder has begun to lose some of its rough surface features so that the chains are shorter.

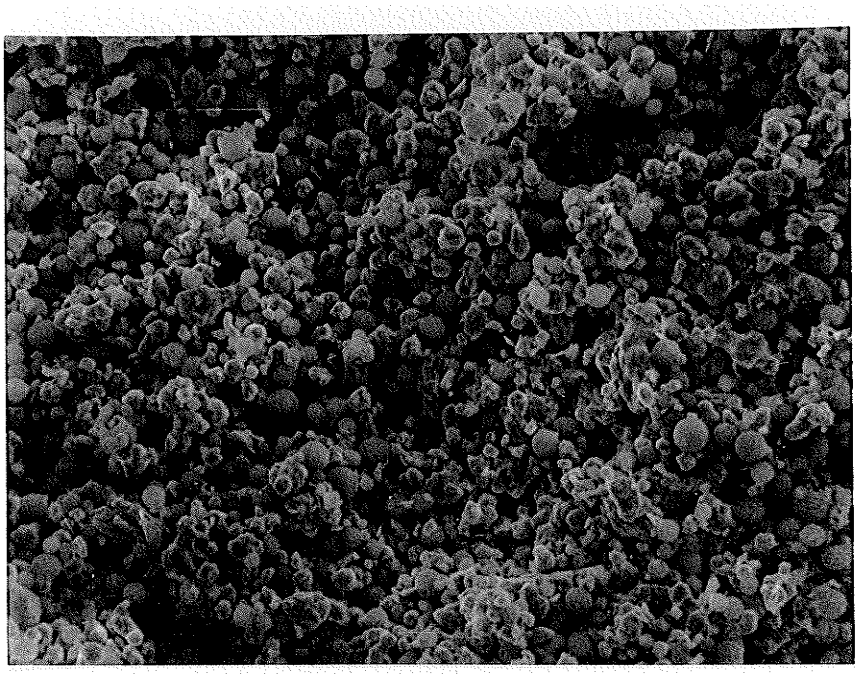

(c) 4 grindings

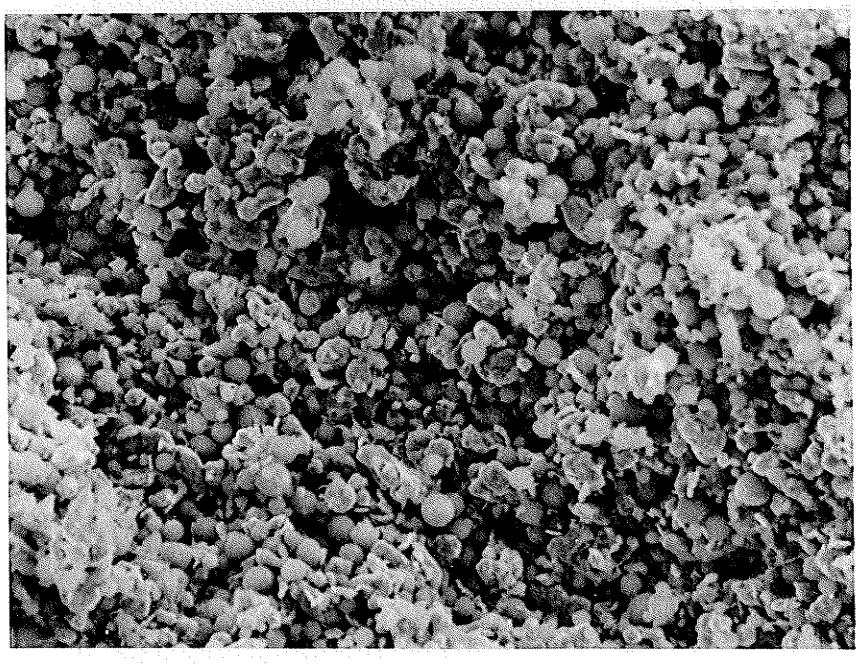

(d) 6 grindings

Figure III-4 (continued): In figure (c), glass beads can be seen within the nickel clusters. In (d), the nickel particles appear to have been badly deformed. Of the different stages of grinding, the homogeneity of (c) was considered to be the best.

it is not possible to have both a sample made using oxidized, uncontaminated nickel and a sample having improved homogeneity using the methods illustrated in this section.

§III: 2.5 — Sample Fractures

When samples were prepared, one chronic problem which occurred was that cracks formed in the sample. Hairline fissures could be seen on one face of the pellet, and they often continued on to the edge of the sample. The location of the fissures were consistently on the pellet's top face (with the mold right-side up). The pellet did not split into two pieces, although beyond that, the extent of these cracks could not be seen. Most samples maintained their integrity after the nickel was etched although the cracks were still visible. Sample #20 lost a long wedge, leaving a large portion of the sample face non-parallel and unpolished.

A sample that lost a wedge can be considered to be an extreme case of a crack in a sample: to have a severe crack would be as though a portion of the sample did not exist since nothing would be transmitted past the fissure. Attenuation measurements, explained and analyzed in §V:3 , were performed on sample #20 . After these measurements, the sample was cut with a diamond saw to remove the portions which were wedge-shaped. Attenuation measurements were repeated, and the results of both trials are displayed in Figure III-5 . The first set of data has a kink in the curve, presumably from interference effects of the

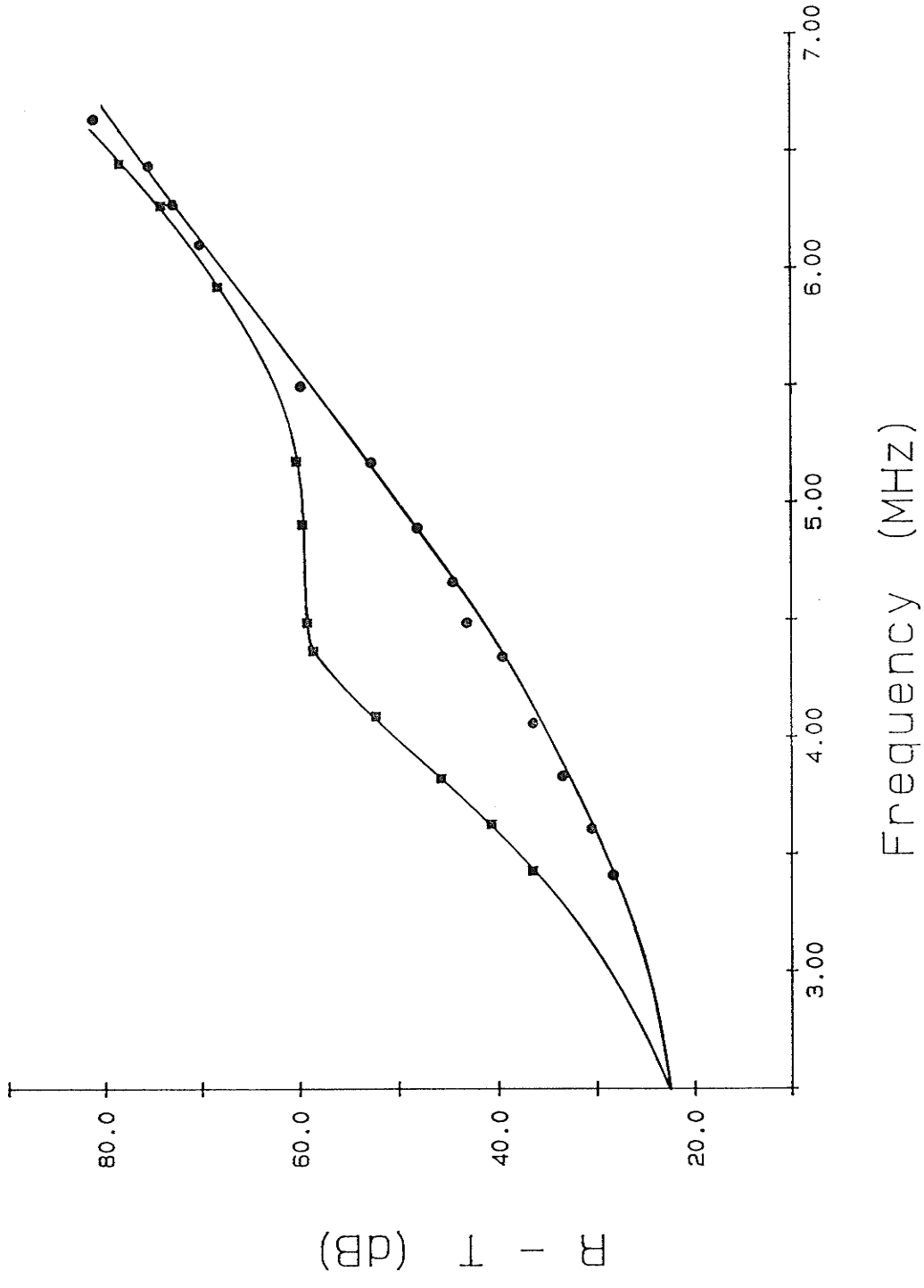

Figure III-5: The effect of severe sample cracks on the measured relative attenuation of sample #20 . The measured frequency-dependent attenuation of a wedge-shaped sample (■) curves irregularly due to phase cancellation. When the wedged portion is cut from the sample, the measured attenuation (●) rises smoothly with frequency.

reflected wave due to the nonparallel surface, in contrast with the smooth curve formed by the second set of data. This figure shows the effect of the most severe crack possible. The other samples did not exhibit a similar effect which means that the extent of their cracks was not nearly as severe.

The cause of the cracks is not clear. Possible contributions may have been a non-ideal value of compression pressure, inhomogeneities due to humidity in the sample, or relatively rough areas of the mold to which the pressed sample might stick. Further investigation is required to resolve this problem.

CHAPTER IV: APPARATUS AND EXPERIMENTAL PROCEDURE

The vibrational modes of a structural percolation system were investigated by studying the propagation of ultrasonic waves through the glass-bead samples described in Chapter III . Each sample was sandwiched between two piezoelectric transducers. An electromagnetic (EM) radio-frequency (RF) signal of frequency range 1 to 20 MHz was triggered and modulated by a pulse ~2 μs long. This RF pulse was transmitted to one of the bonded transducers which transformed the EM pulse to an acoustic pulse. At the transducer/sample interface, the pulse was partially transmitted (and detected by the transducer on the opposite face of the sample), and partially reflected (and detected by the generating transducer). The two transducers reconverted the acoustic pulses back to EM pulses, and the output signals were amplified and displayed on an oscilloscope. Ideally, the transmitted and reflected pulses had identical shapes and there were only two differences between them at the recording device: their time of arrival and their amplitude.

The transmitted pulse was delayed with respect to the reflected wave due to its acoustic transit time through the sample. In order to measure the time delay, the RF oscillations contained within the two pulses were precisely aligned by introducing a known time delay to the reflected pulse. The pulse shape was the guide as to *which* oscillations were to be aligned for the measurements. This delay, in conjunction with the sample thickness, yields the velocity of sound through the sample. The relative amplitudes of the transmitted and reflected pulses

were measured using calibrated attenuators. From these data, the frequency dependence of the ultrasonic attenuation in the samples was determined.

§IV: 1 — APPARATUS

A block diagram of the apparatus is presented in Figure IV-1 , the details of which are described in this section. A pulse generator (PG) triggered and modulated a radio-frequency output from the MATEC (M), and the amplitude of the pulse was controlled by a variable Alan attenuator (A). The signal passed through a power divider (PD) and was sent to the transducers and sample (S). The amplitude of the transmitted signal was controlled by a variable attenuator (T); the reflected pulse was divided by PD (half the pulse directed towards the detection system and the other half directed towards the source of the initial pulse) and its amplitude was controlled by another variable attenuator (R) plus a 3 dB attenuator. For each measurement, either the transmitted or reflected signal was magnified by an amplifier (X). The amplifier was either the MATEC or a Keithley 107 , depending on the measurement being performed. The signal was then sent to an output display device (O) which was either an oscilloscope or a digital signal averager.

§IV: 1.1 — The Transducers

§IV: 1.1a — Principle of Operation

The ultrasonic vibrations were produced using piezoelectric transducers. If an EM RF pulse is applied to a piezoelectric material, the driving voltage oscillations cause a mechanical vibration on the piezoelectric surface: its surface vibrates at the same

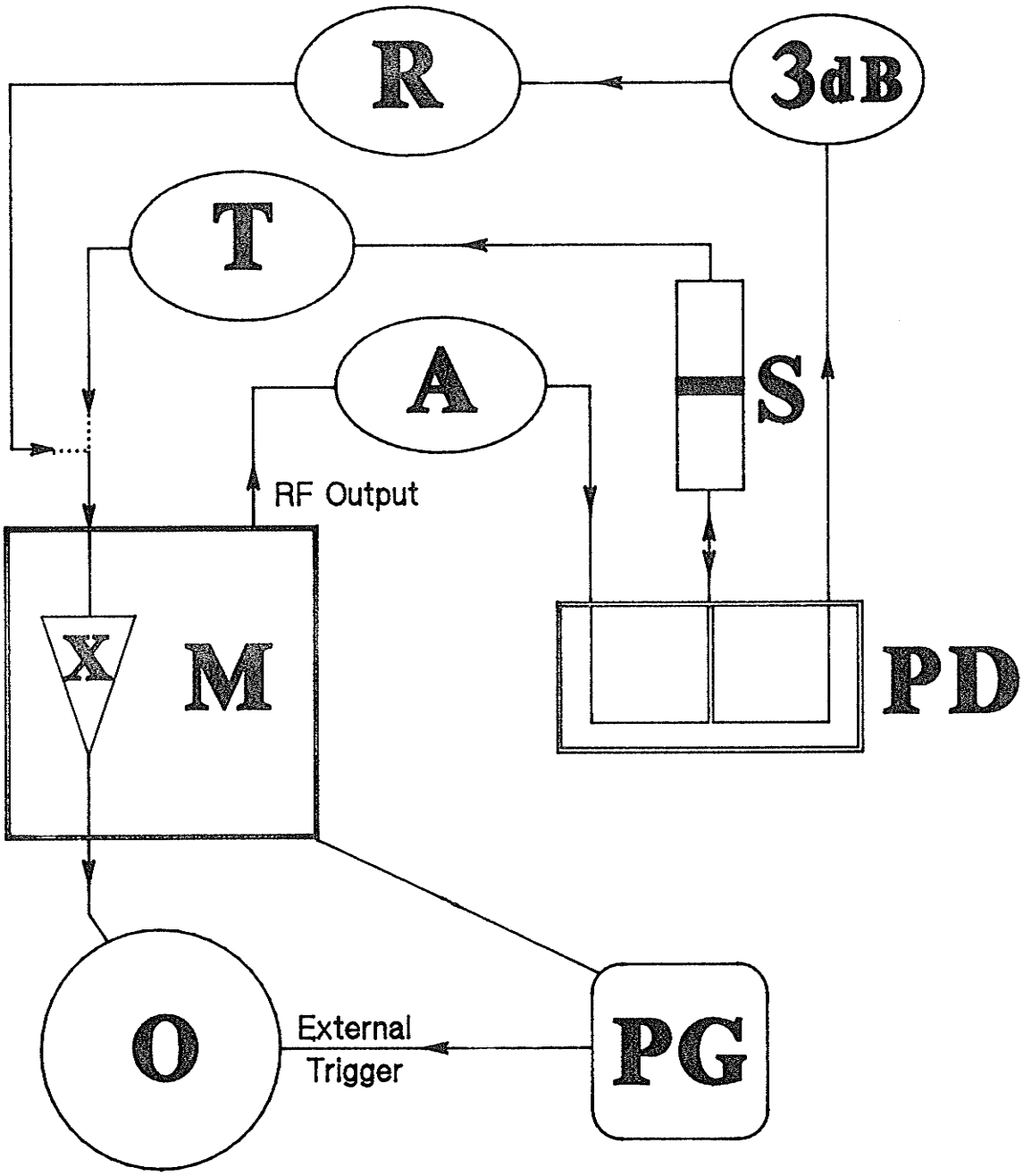

Figure 4-1

M:	MATEC RF source	3 dB:	Attenuator
PD:	Power Divider	R:	Reflected pulse attenuator
X:	Amplifier (MATEC or Keithley)	A:	Alan attenuator
PG:	Pulse Generator	T:	Transmitted pulse attenuator
O:	Output Display	S:	Sample and Transducers

frequency as the RF signal and causes acoustic waves to propagate through the transducer material. Piezoelectric materials can be used to both produce and detect vibrations. They operate most efficiently when the driving frequency excites a mechanical resonance in the transducer; the fundamental wavelength of the transducer is twice its thickness, and all the odd harmonics can be produced by driving it at the appropriate resonant frequencies.

The transducer was bonded with epoxy to a quartz delay rod, as shown later in Figure IV-2a . The purpose of this rod is to create a time delay between the initial pulse and subsequent pulses that are multiply reflected between a sample and the transducer. Without the rod, the delay between such pulses would otherwise be so small that it would be difficult to resolve the individual pulses. In addition, the impedance of the quartz is well matched to the piezoelectric material. If the piezoelectric material is well bonded to the quartz rod, the vibrational energy produced by it is almost completely transmitted through to the rod and the piezoelectric material does not continue to resonate after the initial driving pulse.

In this experiment, pairs of transducers and delay rods were used together. One transducer delivered the pulse to the sample, and it also detected the signal that was reflected from the sample (after travelling through the quartz delay rod). On the other side of the sample, there was another transducer and quartz delay rod used to detect the transmitted signal. The two transducers supplied the information about the attenuation and sound velocity of acoustic waves in the sample.

§IV: 1.1b — Transducer Characteristics

Four different pairs of transducers were used in this experiment. Three of the pairs produce longitudinal waves while one produces transverse waves. One pair of longitudinal transducers was made from a polymer piezoelectric material, the 2 MHz longitudinal and the 1 MHz transverse pairs were made from PZT (lead zirconium titanate compound), and the 1 MHz longitudinal set was made from lead metaniobate. The main properties of the transducers are summarized in Table IV-1 , with a further explanation of the table described in the remainder of this subsection.

"Response Diff." is a description of the difference of the output voltage of a pair of transducers for identical input pulses. If one transducer outputs a larger voltage than the other, averaging the two sets of attenuation measurements gives the true value (as shown in Appendix A). That is, it is necessary to collect two sets of attenuation measurements for a pair of transducers with mismatched outputs, with the roles of the two transducers exchanged for the second set.

"Ringing" describes the oscillations of the transducer that can persist after the 2 μs driving EM pulse. In the generating transducer path, the first interface that the ultrasonic pulse encountered was the transducer/delay rod interface. Part of the wave was reflected back into the piezoelectric material, but most of the pulse transmitted into the delay rod. Ideally the reflected portion was minimal and insignificant. However, if the transducer was not optimally bonded to the delay rod or there was a large impedance mismatch between the transducer and delay rod, the transducer continued to vibrate and

Table IV-1

Transducer Characteristics

Transducer	Longitudinal			PZT Shear
	2 MHz	Polymer	1 MHz	1 MHz
Response Diff.	——	4-18 dB	< 2 dB	< 2 dB
Ringing	no	no	yes	no
Alan Att'n	13-19 dB	0-16 dB	6-22 dB	10-32 dB
Band Width	0.8 MHz	3-15 MHz	0.3 MHz	0.6 MHz
Resonances	2,6,10,..	4-14 MHz	1,3,5,...	1,3,5,...

generate a signal (with decreasing amplitude) after the driving oscillation stopped. This signal was sometimes large enough to interfere with the first reflected echo from the sample.

"Alan Att'n." states the number of decibels that are needed in the Alan attenuator (described in §IV:1.4) to prevent a transducer from either being overdriven or having its gold conducting layer destroyed. An occurrence of the latter was audible, and the output voltage was distorted in the event of the former. The higher values of the listed attenuation range were usually needed for lower frequency measurements. The value listed does not include a 3 dB attenuator which was always inserted between the output of the MATEC and the Alan attenuator.

"Band Width" is the frequency range (centered on a frequency resonance) over which an undistorted pulse containing a single frequency signal exists. The longitudinal polymer transducers are exceptional

because the band width is very large which allows data collection at any frequency in the range listed.

"Resonances" is a description of the approximate resonant frequencies of each of the transducers. For the polymer transducers, the range over which the signal remains within 3 dB of the maximum signal is listed.

§IV: 1.2 — The Delay Rod Supports

The delay rods were supported with a holder system which allowed precise control over the delay rod separation. The glass sinters were prone to compression, but the strain applied to the samples could be chosen and limited with use of this holder. The control of the separation was especially useful when performing measurements on a sample of low occupied volume fraction of glass since there was always a danger of straining it beyond its elastic limit.

The transducer support system (see Figure IV-2) consists of a top and bottom brass holder. Each holder has a mounted brass ring which clamps a delay rod in place. There are three equidistant screws (as shown in Figure IV2b) with springs along the perimeter which fasten the two portions together. The springs supply a force which vastly improves the sample bond and also helps prevent the delay rods from moving laterally with respect to one another. On the top portion there are also three mounted graduated support posts which are equidistantly spaced. They are used to measure and control the separation of the delay rods.

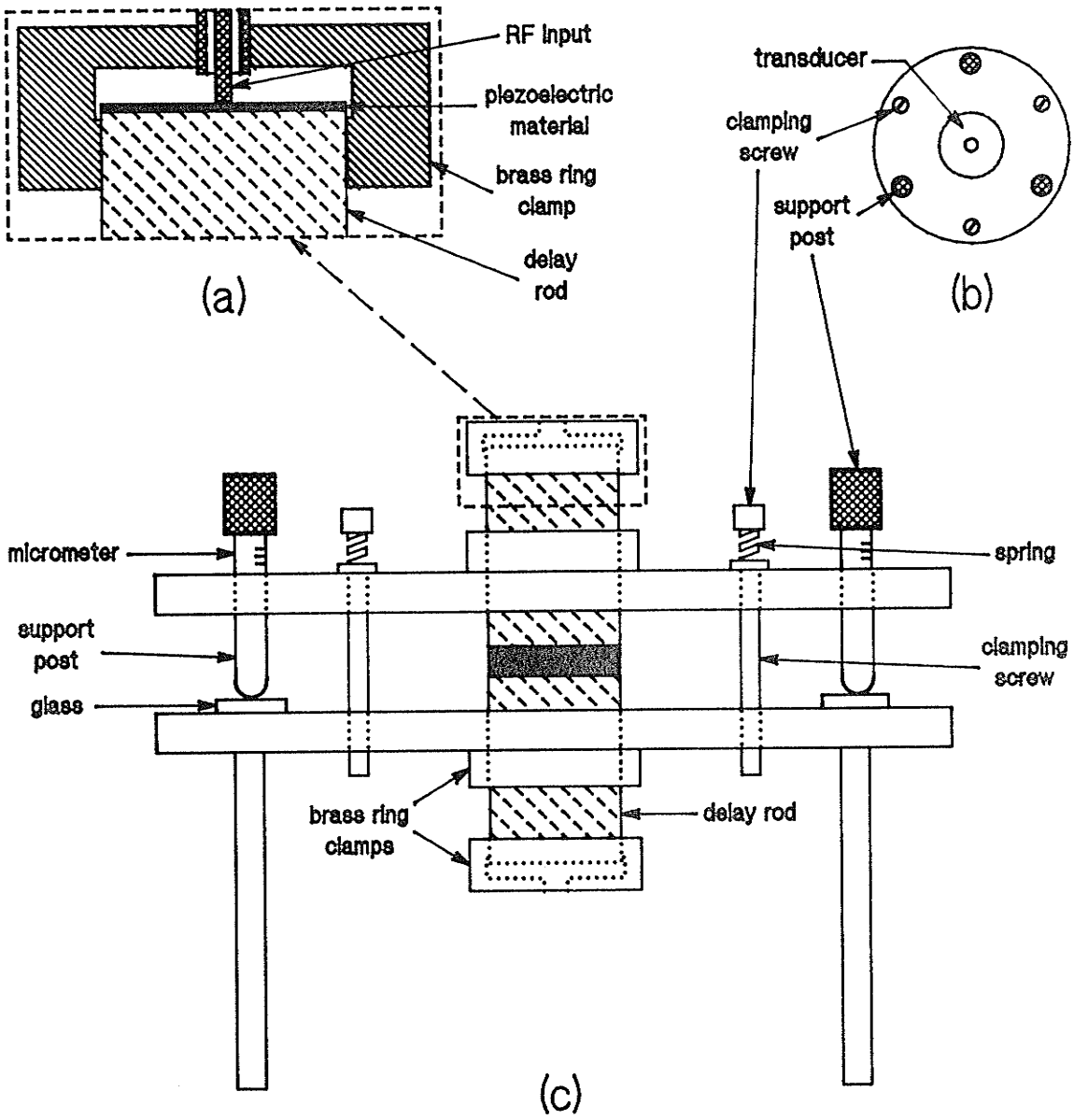

Figure IV-2

(a) Cross section of piezoelectric transducer and delay rod.

(b) Overhead view of sample holder

(c) Side view of sample holder

On the bottom holder (opposite the support posts), flat pieces of glass are fastened to the brass holder with epoxy; the hard surface of the glass ensures that the posts have a reliable reference surface which does not deform under pressure.

The micrometer posts initially supported the full pressure of the springs. Whenever the delay rod separation was altered, the posts were adjusted so as to keep the faces of the delay rods parallel to one another. The top delay rod was lowered until a signal was transmitted through the sample. The rod was further lowered until either the amplitude of the transmitted signal did not increase, or one of the posts was no longer supporting the top portion. If the latter was the case, the forces from the springs were not evenly distributed on the posts and the screws were adjusted accordingly. The posts and screws were alternately adjusted until either the sample essentially took the entire force of the springs, or until it seemed as though lowering the top delay rod did not improve the transmitted signal.

With the more fragile samples, the force upon them was very cautiously administered and a portion of the force of the springs was always supported by the micrometer posts. It was difficult to judge the maximum force that could be applied to these samples because it was difficult to judge if a sample was being crushed; the surfaces of samples #18 and 19 had crumbled somewhat (and #20 to a lesser extent) after etching the samples but before mounting them, so that the exact initial thicknesses of these samples were not known. An increased pressure tended to improve the bond and increase the signal transmitted through the more robust samples (#21 and 22), with no detrimental effects to the samples. With the more porous samples, however, there

was always a danger that the pressure that could potentially improve the bond could also crush the sample. It was necessary to apply pressure in order to have a transmitted signal with a sufficient amplitude for measurements while attempting to minimize the effects of sample compression on the data. The extent of the compression of the samples is later discussed in §V:2.3c .

§IV: 1.3 — Pulse Generation

The radio-frequency signals were produced using a Model 6600 MATEC Pulse Modulator and Receiver which outputs a peak power of 1 kW when terminated at 50Ω . The frequencies produced by a Model 755 MATEC plug-in range from 1 to 20 MHz . The generated signal was modulated and triggered with an external pulse generator. The pulse that was output from this device was typically 2 μs ; this gave sufficient time for the transducers to respond, yet was usually sufficiently short to resolve multiple reflections (cf. §IV:2.2) in the sample.

§IV: 1.4 — The Attenuators

The signal from the MATEC was passed through an Alan Industries variable attenuator which had a range from 0 to 42 dB in 1 dB increments. The attenuator was used to limit the amount of power

delivered to the transducers so that they were not overdriven and the gold film on the transducer (used to deliver the EM potential difference to the piezoelectric material) was not destroyed. In addition, the Alan attenuator was used to eliminate an unwanted stray signal. The reflected wave was divided in two after it was reconverted from an acoustic signal back to an EM signal. Half the signal was sent to the detection system, while the other half was returned to the output of the RF generator. This second signal had to be damped with the Alan attenuator, otherwise it leaked into the MATEC receiver and gave a false signal.

The reflected and transmitted signals produced by the transducers were passed through precision Telonic Altair model 8143S attenuators. These attenuators have a range of 0 to 110 dB , measure in 1 dB steps, and are precise to within ±0.2 dB . They were used to adjust the amplitude of the output voltage of the two transducers. A minimum setting of these attenuators was required in order to help eliminate false signals which originated from leakage from the MATEC receiver. These leakages are small but they can be significant when the transmitted pulse is very highly attenuated in the sample (≅ 100 dB or more).

§IV: 1.5 — The Amplifiers

The EM pulses produced by the transducers were fed to either one or two receiver amplifiers, depending on the measurement method used (as

described in §IV:2.4a). The amplifier usually used was the MATEC receiver which has a gain of ~60 dB . However, it is incapable of amplifying 1 MHz signals and its response time is so slow for a 3 MHz signal that it distorts the leading edge of a pulse.

The other amplifier used was a 107 Pulse Amplifier from Keithley Instruments. It has two available stages of amplification, each of which amplify the input voltage by 20 dB . Its output signals are cleaner than those of the MATEC amplifier, but its use was limited due to the large attenuations of the transmitted signals at higher frequencies. It was used to amplify 1 and 3 MHz signals and to amplify the reflected pulse when both it and the transmitted pulse were simultaneously viewed on the oscilloscope.

§IV: 1.6 — The Band-Pass Filters

When operating at high harmonics, the transducers do not produce only the frequency induced by the driving RF signal; there is also a component of small amplitude at the lower resonant frequencies. The MATEC amplifier does not detect a 1 MHz signal, but it is capable of magnifying 3 MHz signals. For the most part, this frequency component is completely insignificant, but it became important when signals were passed through the samples that had lower packing fractions of glass. For these samples, the frequency at which the transducer was driven was highly attenuated by the sample, but the lower frequency component was much less attenuated. Although the initial amplitude of the lower

frequency component was much less than the driving frequency, it was the lower frequency that was dominant at the receiving transducer. A band-pass filter was used to eliminate both the lower frequency component and most of the background noise.

By use of a variable capacitor, the band-pass filter could be tuned to any frequency between 2.5 to 7.1 MHz with its quality factor ranging from Q=4 to Q=16 . The filter was connected to the oscilloscope input after the selected frequency was set by using a Wavetek Sweep/Signal Generator. A Fluke 6060B Synthesized RF Signal Generator was used as a reference marker.

§IV: 1.7 — The Display Devices

The signals were viewed in one of two ways: either using an oscilloscope or a signal averaging system. For the first method, a Hewlett Packard 1725A Oscilloscope was used to view the signals. It has a "ΔT" time delay function that delays one of its inputs with respect to the other, and this time delay was displayed on a Fluke 8840A digital multimeter. The other system used to display the data was a LeCroy 3500 data acquisition system. It was used to signal average a 5 μs portion of the sweep in channels of 10 ns width. In order to signal average the desired part of the waveform, the LeCroy signal averager was delay-triggered using a Stanford Research System Model DG535 Four Channel Digital Delay/Pulse Generator.

§IV: 2 — EXPERIMENTAL PROCEDURE

In this section, we describe the general form of the ultrasonic wave train arising from a pulse incident on a sample that is sandwiched between two transducers. The details of how the ultrasonic velocity and attenuation were determined from the first pulse of the wave train are discussed. In order to propagate ultrasonic waves through the sample, it was necessary to couple it acoustically to the quartz delay rods; in the first subsection we describe the bonding technique that was used to accomplish this.

§IV: 2.1 — The Bond

A sample was placed between two delay rods. In order to transmit transverse or longitudinal vibrations through a sample, the sample had to be physically joined to the quartz delay rods. This was accomplished by using a very thin layer of oil or grease to bond the polished sample to the rod. To create this layer, a few drops of grease the size of a pin point were placed on the surface of one delay rod and spread over its surface with the other delay rod. The amount of grease applied was just sufficient to cover the entire surface of both delay rods. It was of utmost importance to have the surfaces of the delay rods completely free of any dust or residue before applying the grease since a blemish could act as a wedge between the sample and the delay rod, resulting in a very low transmitted signal.

Different substances were used as the bonding agent. Nonaq Stopcock Grease from Fisher Scientific was initially used on the preliminary samples; it formed a good bond but it appeared as though it was absorbed by the porous samples. Although it was believed that the quantity of Nonaq used was so small that it should not have a significant effect on the data, high vacuum grease from Dow Corning was attempted as the bonding agent because it was considerably more viscous than the stopcock grease. However, the high vacuum grease was difficult to spread into a thin layer, and it was later found to be difficult to remove from a sample after ultrasonic measurements had been completed; measured mass changes revealed that it had also been absorbed by the sample. Silicone oil was the next bonding agent used. It was relatively easy to spread and it left very little residue after it was dissolved in methanol; like the Nonaq, small quantities of it were absorbed, but most of it could be removed. The remainder of the work was done using silicone oil as the bonding agent, although the Nonaq (soluble in toluene) could have also been used.

§IV: 2.2 — The Detected Echo Train

The resultant output from a transducer pair depends upon numerous factors, including the type of transducer used, the width of the pulse, the impedance mismatch between the sample and the delay rod, and the thickness and attenuation of the sample. However, the detected wave train for each sample has the same basic structure because the incident

pulse always passes through the same number of impedance interfaces. A wave incident on an interface produces both a reflected and transmitted pulse, but the amplitude of each pulse is dependent upon the impedance mismatch of the two materials. As seen schematically in Figure IV-3 , the initial pulse divides into many pulses. There are two type of echoes: sample echoes and quartz echoes, and they are discussed next.

At the first sample/delay rod interface ("A" in the figure), a portion of the pulse is reflected from the sample (r_{11}) and a portion is transmitted completely through it (t_{11}). However, a portion of the signal which is transmitted through the first interface is reflected at the second interface and undergoes multiple reflections within the sample, resulting in pulses (sample echoes) that return to both the generating transducer (r_{12}, r_{13}, r_{14},...) and the receiving transducer (t_{12}, t_{13}, t_{14},...), but delayed relative to the first pulses (r_{11} and t_{11}). For highly attenuating samples (such as samples #18-21), the amplitude of the sample echoes are greatly reduced compared to the pulses r_{11} and t_{11} and are frequently too small to be detected.

The other type of echo, the quartz echo, results from reflections in the quartz delay rods. The number of times that a pulse made a round trip through a delay rod (or once through both rods) is denoted by the first subscript of the pulse labels. Each of the quartz echoes is followed by a set of sample echoes similar to the echoes produced from the initial pulse. If the sample is sufficiently attenuating, the sample echoes following the first quartz echo (r_{11}, t_{11}) are small by the time the second quartz echo (r_{21}, t_{21}) arrives at the transducer.

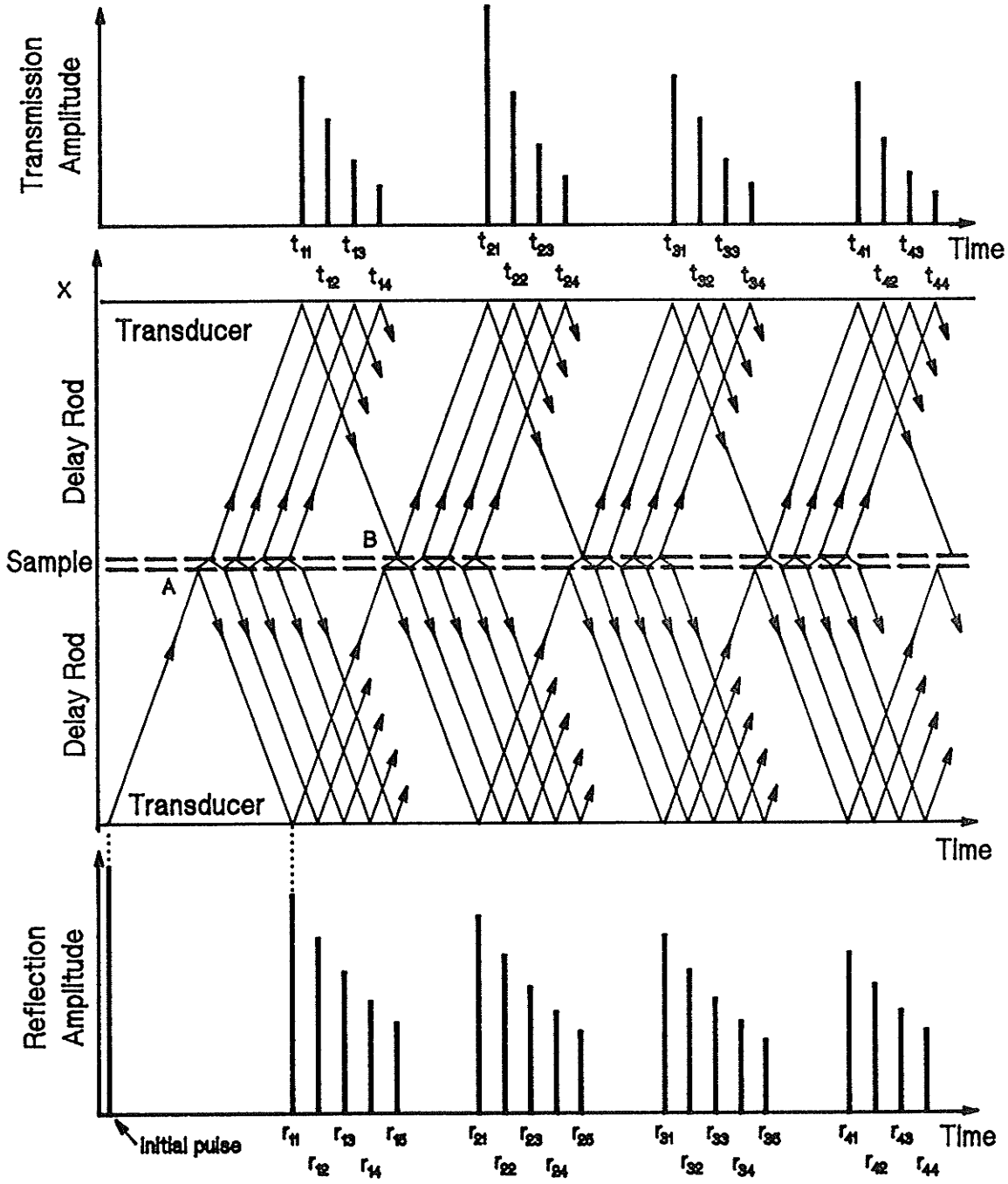

Figure IV-3: Schematic of a wavetrain produced by a pair of transducers that are bonded to a sample. The propagating wave undergoes multiple reflections ($r_{(ij)}$, $t_{(ij)}$) within the sample (j=2,3,4,..) and within the quartz delay rods (i=2,3,4,..). The amplitude of the transmitted wave is much smaller that that of the reflected wave due to the attenuation of the sample. The only the first pulses ($r_{(11)}$, $t_{(11)}$) were used for the velocity and attenuation measurements.

Although the quartz has a higher sound velocity than the samples measured, the quartz echoes are separated by a larger time interval than the sample echoes because the quartz delay rods are much thicker than the samples (~25 mm versus ~1 mm).

The amplitude of the later quartz echoes detected by the receiving transducer (t_{21}, t_{31}, t_{41},...) depends upon the reflection and transmission coefficients at the sample interfaces. As can be seen from Figure III-3 , the pulse t_{21} (at point "B") results from the constructive interference of two signals which have travelled two separate but equivalent paths. One signal makes $1\frac{1}{2}$ round trips in the first delay rod, then travels through the sample and once through the second delay rod. The second signal travels once through the first delay rod, once through the sample, and then makes $1\frac{1}{2}$ round trips through the second delay rod. Ignoring attenuation in the delay rods and sample, and assuming unit probability of reflection at the transducer interfaces, the amplitude of the pulse t_{21} will then be $2TR^{1/2}$, where T and R are respectively the transmission and reflection coefficients at the sample/delay rod interfaces (cf. Appendix C). For pulses $t_{n+1,1}$ that have reflected from the sample interface n times, it follows that the pulse amplitude is $T(n+1)R^{n/2}$. This means that the amplitude of pulse $t_{n+1,1}$ ($n \geq 1$) may be greater than that of pulse t_{11} , depending upon the value of R at the interfaces; an example of the amplitudes of a transmission wave train is shown in Figure III-3 and is similar to wave trains that have been observed for some samples.

§IV: 2.3 — Pulse Distortion

In order to measure the time delay, the RF oscillations were precisely aligned by introducing a measured time delay, but it was the pulse shape that was the guide as to *which* oscillations were to be aligned. The proper alignment of the RF signal was not always obvious because the pulses were not always identical in shape to each other, especially at higher frequencies. This is due to the fact that in order to have a pulse shape, the leading and falling edges of the pulse necessarily consist of a superposition of different frequency components. Since a sample attenuates higher frequencies more than lower frequencies, the edges of the transmitted pulse distort with respect to the initial pulse. This is why it is important to do both time delay and attenuation measurements using only the central region of the pulse.

In order to compensate for the possibility of having the delay measurement offset by one or more periods, delay measurements were recorded not only for the assumed proper alignment of the pulses, but for alignments that were displaced by one or more RF signal period in both the increased and decreased delay directions. This ensured that the proper alignment was achieved for each frequency. Later analysis, described in §V:2.1 , eliminated the phase dependence of the measured time delay.

§IV: 2.4 — Measurement Techniques

§IV: 2.4a — The Oscilloscope

To determine the ultrasonic velocity and attenuation at selected frequencies, it was necessary to measure the period, time delay, and relative heights of the pulses. In order to measure the period when the oscilloscope was used, the reflected pulse was displayed on both channels of the oscilloscope. One channel was delayed with respect to the other using the "ΔT" time delay function of the Hewlett-Packard oscilloscope, and its oscillations were precisely aligned with the display of the reflected pulse. In order to minimize the uncertainty of the measured frequency, the second pulse was delayed by the maximum number of periods that kept it within the flat central region of the pulse.

Three different methods were used to perform the measurements of the relative time delays and attenuations of the pulses, two of which involved an oscilloscope. When both signals were displayed simultaneously on the oscilloscope, the transmitted signal was passed through the MATEC amplifier and the relatively larger reflected signal was passed through the Keithley amplifier. The relative time delay of each frequency (plus two other measurements offset by ±1 period) was measured to within ~0.5% precision by adjusting the "ΔT" time delay function until the transmission signal was aligned with the reflected signal. This method permits direct comparison of the shape of the pulses, but the attenuation cannot easily be measured in this configuration because the amplifiers have different frequency responses. It was

also necessary to correct the measured time delays of the transmitted signal because the time delays through the two different amplifier paths were frequency dependent. This method of time delay measurement was used only for the preliminary samples (#5,6 and 13); the delays of the standardized samples (#18-22) were measured using a method which did not require delay corrections, as described next.

If only one signal was displayed at a time, the same amplifier (usually the MATEC) was used for both the reflected and transmitted signals. Reference marks on the oscilloscope were used to align the pulses for time delay measurements. For the delay data, the pulses were centered about a chosen horizontal axis, and usually the zero crossover point of a chosen oscillation was aligned at the reference point so long as the pulse was symmetric about the horizontal reference. Sometimes instead, if the background noise badly obscured the signal, delay measurements were performed by centering a peak or valley on a vertical reference line, but it was important for the chosen oscillation to be symmetric about the vertical reference axis. In order to measure the attenuation of the transmitted signal with respect to the reflected signal, the precision Telonic attenuators were used to adjust the height of the pulses to some reference voltage. The transmitted pulse was first adjusted to be as near the reference voltage height as possible. The reflected pulse height was then adjusted and recorded twice, once just above and once just below the reference voltage. The attenuation necessary to make the reflected pulse equal in amplitude to the transmitted pulse (and the reference voltage) was interpolated.

Besides its convenience for the attenuation measurements, this method of displaying one signal at a time has an added advantage over

using two amplifiers. Since only one amplifier and the same coaxial cables are used, nearly the same electrical paths are used for both transmitted and reflected pulses. The signals did pass through two different semi-rigid cable paths from transducer to a Telonic attenuators, but the path length was only about 1 ns longer along the transmitted signal path than the reflected signal path. The power divider through which only the incident and reflected signal passed caused an approximately 1 ns delay in the reflected signal path at 10 MHz . These 1 ns delays in both paths cancel so that the correction factor for the different paths is negligible when this method was used.

§IV: 2.4b — Signal Averaging

The other method of displaying the signal was to digitize the pulses using the LeCroy signal averager. This technique is useful if the signal-to-noise ratio is small; the instrument adds successive sweeps of a repetitive signal and on average the random background noise cancels, while any real signal does not.

There is also the added convenience that the digitized data can be can be analyzed with a computer. Although the resolution of the digitizer is 10 ns , a program was used to improve the precision of the extrema of the pulse oscillations by fitting a parabola to each peak and valley of the wave train. The time delay of the aligned pulses is calculated by averaging the time delay for each corresponding peak and valley of the reflected and transmitted pulses over the entire flat central region of the pulse. This process reduces the uncertainty of

the measured frequency and time delay to a few nanoseconds. Bearing in mind the restriction of using only the central region of the pulse, usually a time delay for a period offset of up to about ±4 or 5 periods was calculated with the program. The program also interpolates the relative attenuations using the extrema of the fitted parabolas. By using all of the peaks within the flat area for the calculation, the resultant variation of the attenuation indicates the degree of pulse shape distortion.

Chapter V: Data and Analysis

Ultrasonic experiments were performed on three preliminary samples and five standardized samples. In §V:1 , the dependence of the sample density on occupied volume is shown to be well described by percolation theory. In the following section, both the longitudinal and transverse acoustic velocity are calculated from extrapolations of time delay measurements, and their dependence on $f-f_c$ is compared to predictions for a percolating system. In the final section, the attenuation data of the samples are condensed to a single curve using scaling arguments, and the resultant scaled frequency dependence is compared to the models discussed in §II:4 .

§V: 1 — OCCUPIED VOLUME FRACTION AND DENSITY

The occupied volume f and density ρ of each sample were calculated from the measured sample mass and volume. The scaling of the density with $f-f_c$ is shown to be in very good agreement with percolation theory.

§V: 1.1 — Occupied Volume Fraction

The thickness of the sample was measured with a travelling microscope before heating so that the sample volume could be calculated. The fraction of the sample volume occupied by the glass beads was calculated using the following formula, and the value of each sample is listed in Table V-1:

$$f_{glass} = \frac{m_{tot}}{M_{tot}} \frac{M_{glass}}{\rho_{glass} V} \qquad (V\text{-}1)$$

where f_{glass} is the occupied volume fraction of glass,

m_{tot} is the total mass of the pellet,

M_{tot} is the total mass of the mixture

(m_{tot} / M_{tot} is the fraction of the total mixture that was used for the sample),

ρ_{glass} is the density of the glass,

M_{glass} is the total mass of the glass in the mixture, and

V is the volume of the pellet .

Table V-1

Packing Fraction of Glass

Sample #	Thickness (±10 μm)	M_{glass} (g)	f_{glass}
5	738	0.0819	0.270
6	808	0.0828	0.271
13	1360	0.1272	0.263
18	1080	0.1200	0.280
19	1230	0.1448	0.314
20	1140	0.1622	0.354
21	1110	0.1818	0.400
22	1080	0.2058	0.486

The measured density of the glass is (2.475 ± 0.0015) g/m as found in §III:2.3 .

A different set of glass-bead sinters were prepared by G. Cosby. These samples were prepared under the same sintering conditions as those outlined in §III:1 , but the occupied volume fraction of the glass beads was made lower than those of samples #19-22 . From these samples, the percolation threshold f_c was estimated to be $f_c = 0.187 \pm 0.008$ from the fact that one sample with $f = 0.180$ disintegrated when the nickel was etched from it while another sample of packing fraction $f = 0.195$ remained (mostly) intact.

§V: 1.2 — Sample Density

The density of each sample (Table V-2) was calculated after they were sintered and polished flat and parallel. Before a sample was immersed in acid, its thickness was measured with a micrometer and found to have a thickness variation of ±2 μm or less. Each sample was weighed after its nickel (oxide) was etched and the resultant densities of the samples are listed in Table V-2 . Samples #5, 6, 13 and 18 lost pieces after etching; their irregular shapes prevented precise measurement of the volumes and hence the densities were not calculated.

Table V-2

Density of Samples

Sample #	*Thickness (μm)	Mass (g)	Density (kg/m^3)
19	810 ± 1	0.0778	724
20	921 ± 2	0.0973	796
21	984 ± 1	0.1230	942
22	974 ± 2	0.1158	†1050

* ⟶ Thicknesses listed were measured with a micrometer *after* the samples were sintered and polished, but *before* being etched. The samples were weighed *after* etching. Any small pieces that crumbled from edges were also included in the mass measurements.

† ⟶ A segment of chord length 1.09 cm had been cut from sample #22 ; the density calculation accounts for this.

§V: 1.3 — Scaling of the Density with Occupied Volume Fraction

A logarithmic plot of density versus $f-f_c$ is shown in Figure V-1 . The slope obtained is 0.44 ± 0.03 in comparison with the theoretical value of $\beta = 0.44$ previously mentioned in §II:2.4 . Thus the experimental value is in very good agreement with the theoretical exponent and seems to indicate that percolation scaling laws apply even up to rather large values of $f-f_c$.

During the preparation of the lower density samples (by G. Cosby), the packing fraction and density of the samples were measured after the samples were heated, as opposed to samples #18-22 whose thicknesses were measured only before heating. The thickness of each of the low density samples could be measured over a very small surface area because a 5 mm diameter glass bead was mounted on one face of the micrometer. It was found that the sample thickness variations were significant (~5%), presumably due to volume changes caused by nickel oxidation, heat expansion, or sintering.

Because of the local thickness variations, an alternate method of volume measurement was performed on the low density set of samples which involved saturating the pores of the sample with oil and measuring the volume of water displaced by the sample. The volume measured from the water displacement method was found to yield a value about 4% less than the volume calculated using travelling microscope measurements. This not unexpected since the latter method registers only the thickest part of the sample so that the calculated volume is overestimated. This calculated correction however, can not be directly applied to the previous volume measurements of the samples listed in Table V-1

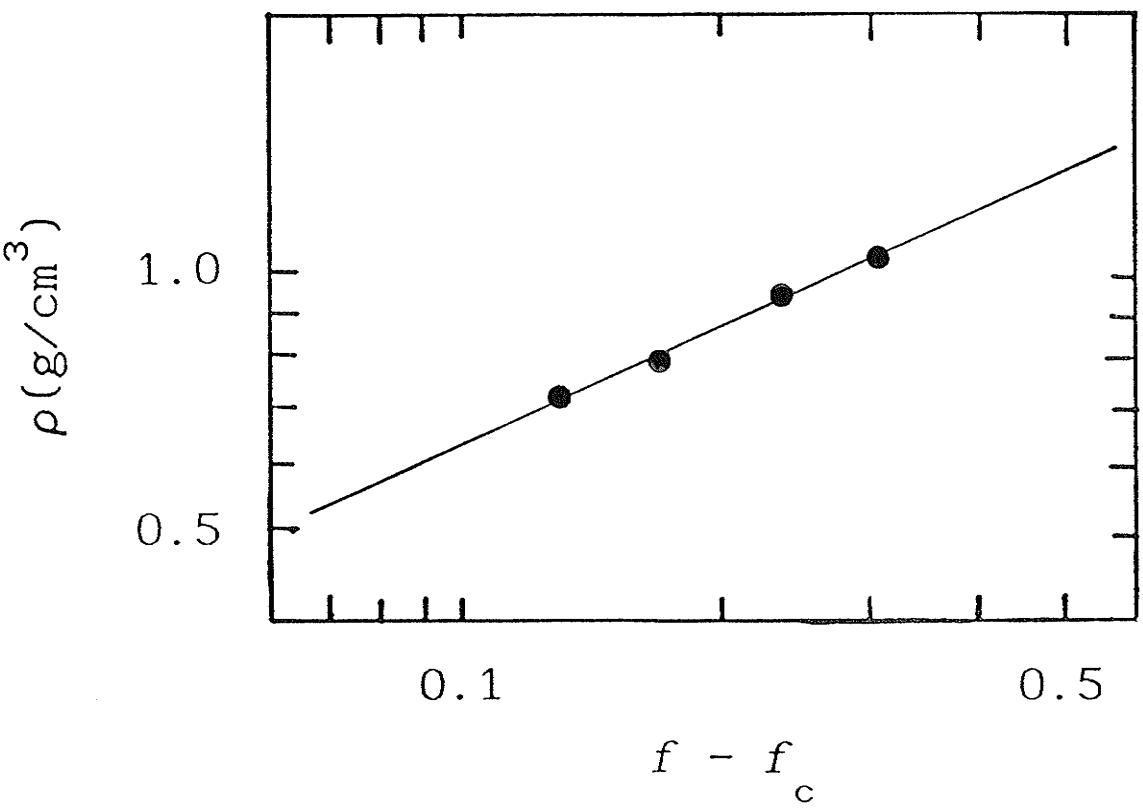

Figure V-1: Logarithmic plot of density versus $f-f_c$ yields a slope of 0.44 ± 0.03 , in comparison with the theoretical value of $\beta = 0.44$.

because their thickness measurements were measured *before* the sample was sintered (with a travelling microscope), whereas volume measurements of the other set were performed only after the samples were sintered. The heating of the samples could have caused the measured volume to either increase due to oxidation of the nickel or to decrease due to sintering shrinkage.

§V: 2 — VELOCITY MEASUREMENTS

The ultrasonic velocity was calculated from the measured transit time (equal to the delay of the transmitted pulse with respect to the reflected pulse) of an acoustic pulse through each sample. These measurements were performed with both longitudinal and transverse pulses, over as large a frequency range as could be transmitted through the samples. For each sample, the collection of delay data was extrapolated to its zero-period limit so that any delay contributions caused by phase differences between the two wave trains were eliminated. The velocity through each sample was easily calculated once the thickness of the sample was measured, and the magnitude of compression and its effect on the sample velocities were also considered. The scaling of the velocities with $f-f_c$ was investigated and the best fit line was found to yield an exponent in better agreement with the tensorial bond-bending model than the scalar Born model, in contrast with results found by Courtens *et al* [1987] for aerogels.

§V: 2.1 — Time Delay Measurements

The method of measurements of the time delays was described generally in the introduction to §IV and in further detail in §IV:2.4 . The measurements were analyzed so that timing errors (between the transmitted and reflected pulses) due both to an offset of one or

more periods in the Δt measurements and to phase shifts arising at the quartz rod/sample interfaces were eliminated. If we assume that these phase shifts are independent of frequency, a plot of time delay versus the period forms a straight line and the true transit time through the sample can be obtained by an extrapolation to zero period. Furthermore, errors due to an offset of one or more periods can also be eliminated by this extrapolation since for a set of delay measurements of transmitted pulses that are properly overlapped with the reflected pulses, a plot of the time delay versus the period yields a straight line of approximately zero slope. For a set of time delays offset by one or more periods, the measurements are still linearly dependent on the period but have a steeper slope. All the lines should extrapolate to the same delay at zero period and thus the transit time through the sample can be unambiguously determined from the intercepts.

For all samples, the time delay of the transmitted signal with respect to the reflected signal was recorded for different frequencies over a range of period offsets. The complete set of data is found in Appendix D , but an example of one of the graphs, the measured time delay versus the period for longitudinal waves travelling through sample #20 , is shown in Figure V-2 . An unweighted least-squares fit was performed on the data for each period offset to obtain the equations of the best fit lines. The data was linear to a very good approximation, indicating that the assumption of a constant phase shift versus frequency is reasonable. However, each fitted line did not yield the exact same zero-period extrapolation. The calculated intercepts of Figure V-2 , along with their uncertainties arising from the scatter of fitted

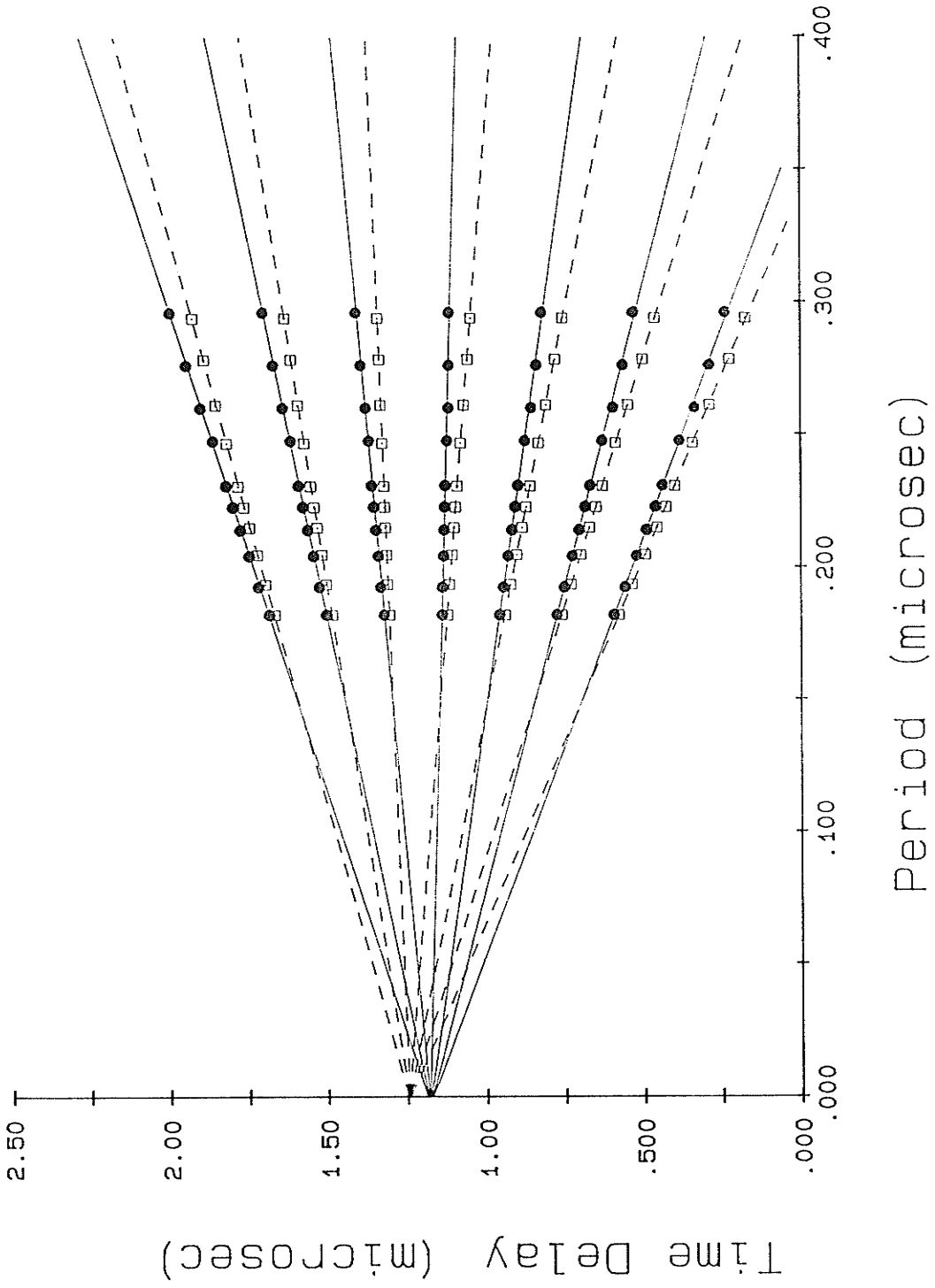

Figure V-2: Longitudinal delay measurements versus period for sample #20 , with PZT transducer #1 (——,●) and #2 (----,□) as the generator. The most horizontal line corresponds to the zero-period offset.

Table V-3

Sample 20: Y-intercepts of Figure V-2
With Each Transducer as the Generating Transducer
(Longitudinal Polymer Transducers)

#1 Generating		#2 Generating	
Period Offset	Time Delay (μs)	Period Offset	Time Delay (μs)
+3	1.189 ± 0.005	+3	——
+2	1.186 ± 0.004	+2	1.248 ± 0.004
+1	1.184 ± 0.004	+1	1.246 ± 0.002
0	**1.181 ± 0.004**	**0**	**1.246 ± 0.002**
-1	1.178 ± 0.006	-1	1.246 ± 0.002
-2	1.175 ± 0.008	-2	1.245 ± 0.002
-3	1.173 ± 0.010	-3	1.245 ± 0.002
-4	——	-4	1.242 ± 0.004

Note that the difference of intercept for the two different orientations is attributed to a difference in transit time through the two delay rods and does not contribute to the precision of the calculated time delay through the sample. The actual transit time through the sample is the average of the two extrapolated values.

Therefore, the actual time delay is $\langle \Delta t \rangle = (1.214 \pm 0.003)\ \mu s$.

points, are listed in Table V-3 ; they show a small but systematic increase with increase of period offset.

The systematic error could arise from the measurement of the periods. As described in §IV:2.4 , the methods used to measure the periods allow a period precision of ~0.5% , which could in turn could cause a systematic contribution to the zero-period extrapolation of ~0.5 ns per period offset. The effect of pulse edge distortions could make an additional contribution of ~1 ns per period offset, as more

fully explained in the next paragraph. When considered in conjunction with the statistical uncertainties of the extrapolations, these systematic error contributions are sufficient to explain the small discrepancies of the zero-period extrapolations of the different offset data. Since the systematic error is smallest for the data with a period offset of zero, the transit time through the sample and its uncertainty is considered to be the zero-period extrapolation of the data with the period offset equal to zero.

A systematic error in the period measurement existed for a range of frequencies due to distortion caused by the leading and falling edges of the pulse. For the highest frequencies that were propagated through the samples, the period was calculated from the cycles within the flat central region of the pulse and any systematic error arising from pulse distortion was completely negligible. However at the lowest frequencies, there were very few cycles contained within a pulse so that peaks near the edge of the pulses were included in the period calculation. For example, when $T > 0.3\ \mu s$ for sample #22 with the polymer transducers, there is approximately a 3% difference between the period calculated from a single period in the middle region of the pulse and the period calculated from multiple cycles extending from the leading edge to the falling edge of the pulse. Since the least-squares fit was unweighted, these less accurate points were omitted from the calculation. The limited edge distortion of the remaining data that was included in the least-square fit affected the zero-period extrapolation by less than ~1 ns per period offset.

The extrapolations have been corrected for a small frequency-dependent phase delay which exists. As shown in Appendix C , waves

propagating through an attenuating medium undergo a phase shift at an impedance interface, and the size of this phase change is dependent upon the magnitude of the frequency-dependent attenuation. Correction factors for the samples were calculated and are found in the same appendix. The delay data and extrapolations of all the samples are listed in Appendix D , the results of which are summarized in Table 4b of §V:2.3a .

§V: 2.2 — Thickness Measurements and Compression

The micrometer posts of the delay rod support system were used to measure the thickness of a sample while the velocity or attenuation measurements were being made. The zero settings of the posts were noted when the delay rods were bonded to one another with no sample present. The micrometer vernier scale of each post had a precision of about 2 μm , but the zero setting of the posts were reproducible only to within about ± 10 μm (± 0.0005") for the bonded delay rods. The precision of the sample thickness was better however since the error of each post setting was random: the delay rods would be at a slight angle with each other. Since the distance between the posts was about 6.5 cm and the sample diameter was about 1.3 cm , the uncertainty across the sample was only about ± 3 μm (± 0.0001"). The listed uncertainties of some thickness measurements in Table V-4 were greater if the delay rods were (unintentionally) not made optimally parallel.

After the samples were polished but before the nickel was removed, the thicknesses of the samples had been initially measured with a micrometer (listed in Table V-4). The measurements of sample thickness during the ultrasonic measurements show that it was necessary to appreciably compress several of the samples in order to obtain an adequate bond for a transmitted signal. Generally, the more porous the sample, the more it was subject to compression. The thickness of the (compressed) samples during the ultrasonic experiments are found in the same table. Note the substantial compression of the preliminary samples (#6, 5, and 13), as well as that of the most porous of the standardized samples (#18, 19, and 20).

§V: 2.3 — Ultrasonic Velocity Data

§V: 2.3a — Velocity Calculations and Compression Effects

The longitudinal and transverse velocities are easily obtained from the measured time delays and thicknesses, and they are summarized in Table V-4 .

Samples #6, 5, and 13 , made before the sample preparation techniques had been standardized, had a range of measured sound velocities greater than would be expected from the difference in occupied volume fractions alone. In particular the longitudinal velocity of sample #13 is much greater than those of samples #5 or 6 , although the occupied volume fraction of sample #13 is slightly less (Table V-1). This

result shows the extreme sensitivity of sample elasticity to preparation conditions, and emphasizes the need for the reproducible sintering procedure that was followed for samples #18-22 .

The measurements of the longitudinal ultrasonic velocities in each of samples #5, 6, and 13 were repeated with different compressions of the samples in the ultrasonic propagation direction so that the significance of sample strain on the ultrasonic velocity could be studied.

Table V-4a

Velocity Data: Preliminary Samples

#	Transducer	d (μm)	Δt (μs)	v_L (m/s)	v_T (m/s)
6	—	* 808 ± 10	—	—	—
	1 MHz shear	813 ± 3	no signal	—	—
	2 MHz long.	† 639 ± 7	1.65 ± 0.10	390 ± 20†	—
	2 MHz long.	605 ± 10	1.64 ± 0.02	369 ± 8	—
5	—	* 738 ± 10	—	—	—
	2 MHz long.	635 ± 3	1.75 ± 0.10	360 ± 20	—
	2 MHz long.	584 ± 3	1.90 ± 0.15	310 ± 30	—
13	—	*1360 ± 10	—	—	—
	2 MHz long.	1339 ± 3	2.04 ± 0.05	660 ± 20	—
	polymer	†1180 ± 30	1.85 ± 0.10	640 ± 30†	—

* ——→ This was the initial thickness *after* polishing, measured with a micrometer.

† ——→ The surface of the sample had previously crumbled so that the decrease in thickness does not *necessarily* indicate compression.

Table V-4b

Velocity Data: Standardized Samples

#	transducer	d (μm)	Δt (μs)	v_L (m/s)	v_T (m/s)
18	——	* 360 ± 10	——	——	——
	polymer	330 ± 10	no signal	——	——
19	——	* 810 ± 1	——	——	——
	polymer	787 ± 4	1.41 ± 0.04	560 ± 20	——
	1 MHz shear	† 762 ± 5	2.9 ± 0.2	——	260 ± 20†
	1 MHz long.	**774 ± 3	not measured**	——	——
20	——	* 921 ± 2	——	——	——
	polymer	894 ± 10	1.205 ± 0.003	742 ± 9	——
	1 MHz shear	831 ± 4	1.68 ± 0.02	——	495 ± 6
	1 MHz long.	**311 ± 3	not measured**	——	——
21	——	* 984 ± 1	——	——	——
	polymer	987 ± 4	0.850 ± 0.004	1161 ± 7	——
	1 MHz shear	974 ± 15	1.22 ± 0.02	——	800 ± 20
	1 MHz shear	979 ± 3	1.19 ± 0.04	——	820 ± 30
22	——	* 974 ± 2	——	——	——
	polymer	973 ± 3	0.628 ± 0.007	1550 ± 20	——
	1 MHz shear	973 ± 4	0.904 ± 0.010	——	1076 ± 13

* ——→ This was the initial thickness *after* polishing, measured with a micrometer.

† ——→ The surface of the sample had previously crumbled so that the decrease in thickness does not *necessarily* indicate compression.

** ——→ Velocity measurements were not performed with the 1 MHz longitudinal transducers; this was the sample thickness during attenuation measurements.

Although the uncertainties are large, it can be seen in Table V-4a that sample compression seems to have resulted in a decrease of longitudinal velocity.

The possible decrease of acoustic velocity with strain is in agreement with a recent investigation performed by Xhonneux *et al* [1989]. They measured the effect of uniaxial stress on acoustic velocity of aerogels and found that there is a decrease of velocity when a stress was applied to the sample, although the strain was kept sufficiently small to keep the deformations within the elastic limit of the samples. It is also possible, however, that with strains as large as those applied to samples #5 and 13 , the compression not only stressed the sample bonds, but broke some of the weaker ones. This would result in a less rigid sample that has a lower, "softened" sound velocity.

The strain applied to sample #6 during its longitudinal velocity measurements is not known because the sample surface had previously partially crumbled to an unmeasured thickness after a prior attempt to measure its transverse velocity. However, the applied strain is easily calculated for samples #5 and 13 and is seen (Table V-4a) to range from about 1 to 20% . It is seen that the effect of the changes in the strain on the longitudinal velocity was only on the order of 10% over this range of strains, comparable to their large velocity uncertainties. In contrast, the strains applied to samples #19-22 were typically five to ten times less than those applied to the preliminary samples (except for the transverse velocity measurements of sample #19 and 20 whose strains were of the same order). This suggests that the possible effect of the strain on the velocity measurements in samples #19-22 would typically be on the order of only 1% (apart from the transverse

measurements previously noted), assuming the effect was linearly dependent on the strain. This amount is no greater than the uncertainty of most of the velocity measurements.

§V: 2.3b — Scaling of the Ultrasonic Velocity with Occupied Volume Fraction

Examination of the velocity values listed in Table V-4b reveals that the ultrasonic velocity varies strongly with the occupied volume fraction of a sample. A logarithmic plot of the shear and longitudinal velocities versus $f-f_c$ is presented in Figure V-3 and shows the slopes of the best fit lines are found to be 1.25 ± 0.10 . Equation (II-13) and this slope can be combined to calculate the value of the fracton dimension $\tilde{d}$:

$$\nu(D/\tilde{d} - 1) = 0.88(2.5/\tilde{d} - 1) = 1.25 \pm 0.10$$

Therefore $$\tilde{d} = 1.0 \pm 0.1 \quad .$$

The value of D used in the calculation was obtained from theoretical values (§II:1.2a), the value of which is supported (over a limited length range) by autocorrelation measurements performed on a two dimensional cross section of sample #20 (Chapter VI). The measured value of $\tilde{d}$ is in closer agreement with the bond-bending model ($\tilde{d}_{b\text{-}b} = 0.89$) than the scalar Born model ($\tilde{d}_{Born} = 1.33$).

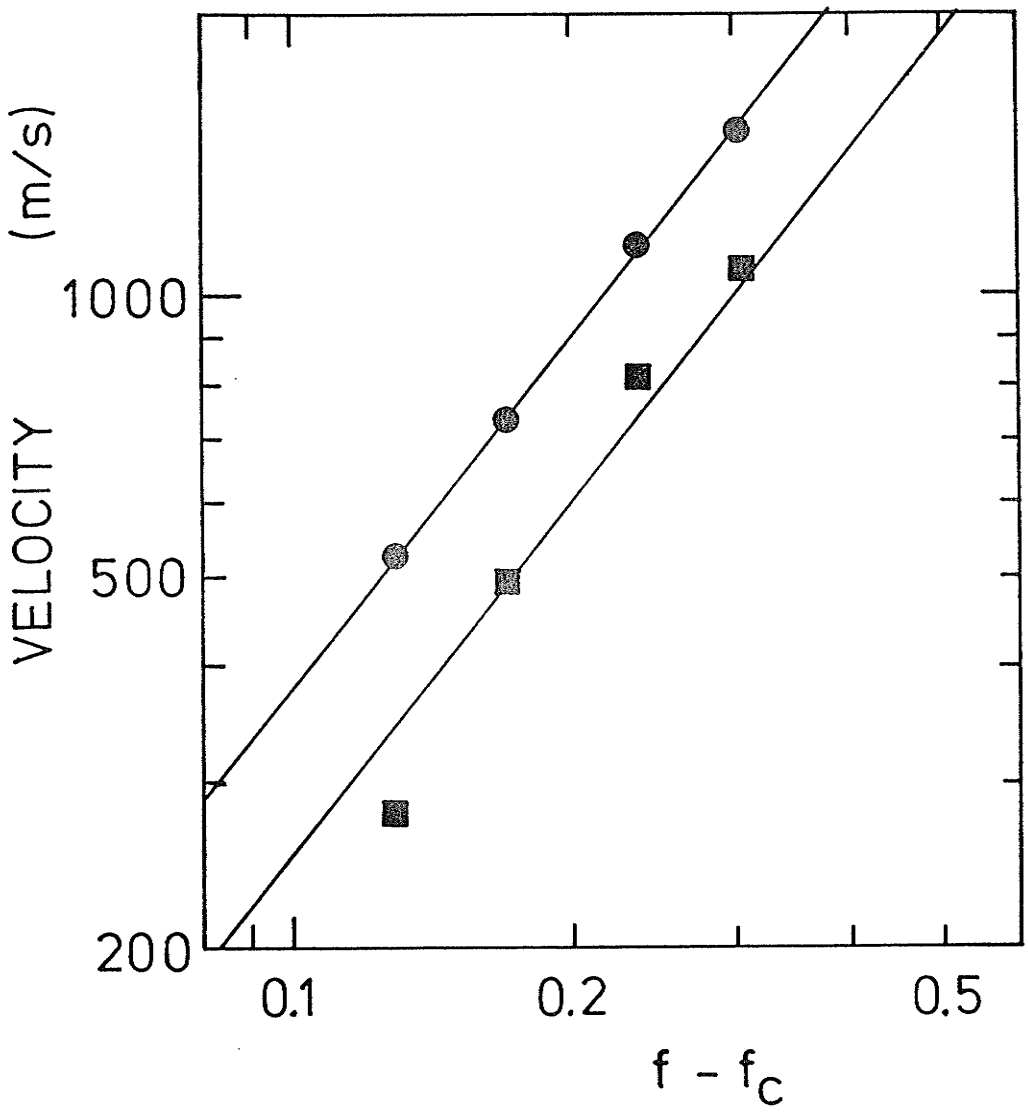

Figure V-3: Logarithmic plot of the transverse (■) and longitudinal (●) velocities versus $f-f_c$. The slopes of the best fit lines are 1.25 ± 0.10 , which gives the result that the fracton dimension of the samples is $\tilde{d} = 1.0 \pm 0.1$.

§V: 3 — ATTENUATION MEASUREMENTS

The ultrasonic attenuation of each sample is calculated from the relative heights of the pulse that transmitted through a sample and the pulse which reflected from the delay rod/sample interface. This data was gathered over as large a frequency as possible for both longitudinal and transverse modes. To quantitatively compare the frequency-dependent attenuation curve of each sample, it is necessary to extrapolate a zero-frequency baseline for each curve. Once the curves are all plotted with a common (absolute) origin, the validity of single-variable scaling arguments is then investigated and used to condense all of the attenuation data to a common curve. The frequency dependence of the attenuation is extracted from the data and compared to theory.

§V: 3.1 — Baseline of the Attenuation Curves

The relative amplitude of the reflected (R) and transmitted (T) pulse voltage were measured for both longitudinal and transverse waves, and all of the measured values of the samples are presented in Figure V-4 . Note that two different longitudinal attenuation curves over two different frequency ranges (from two different pairs of transducers) were obtained for each of samples #19 and 20 . In order to obtain a continuous frequency-dependent attenuation curve for these two samples, and also to allow quantitative comparison of all the attenuation curves

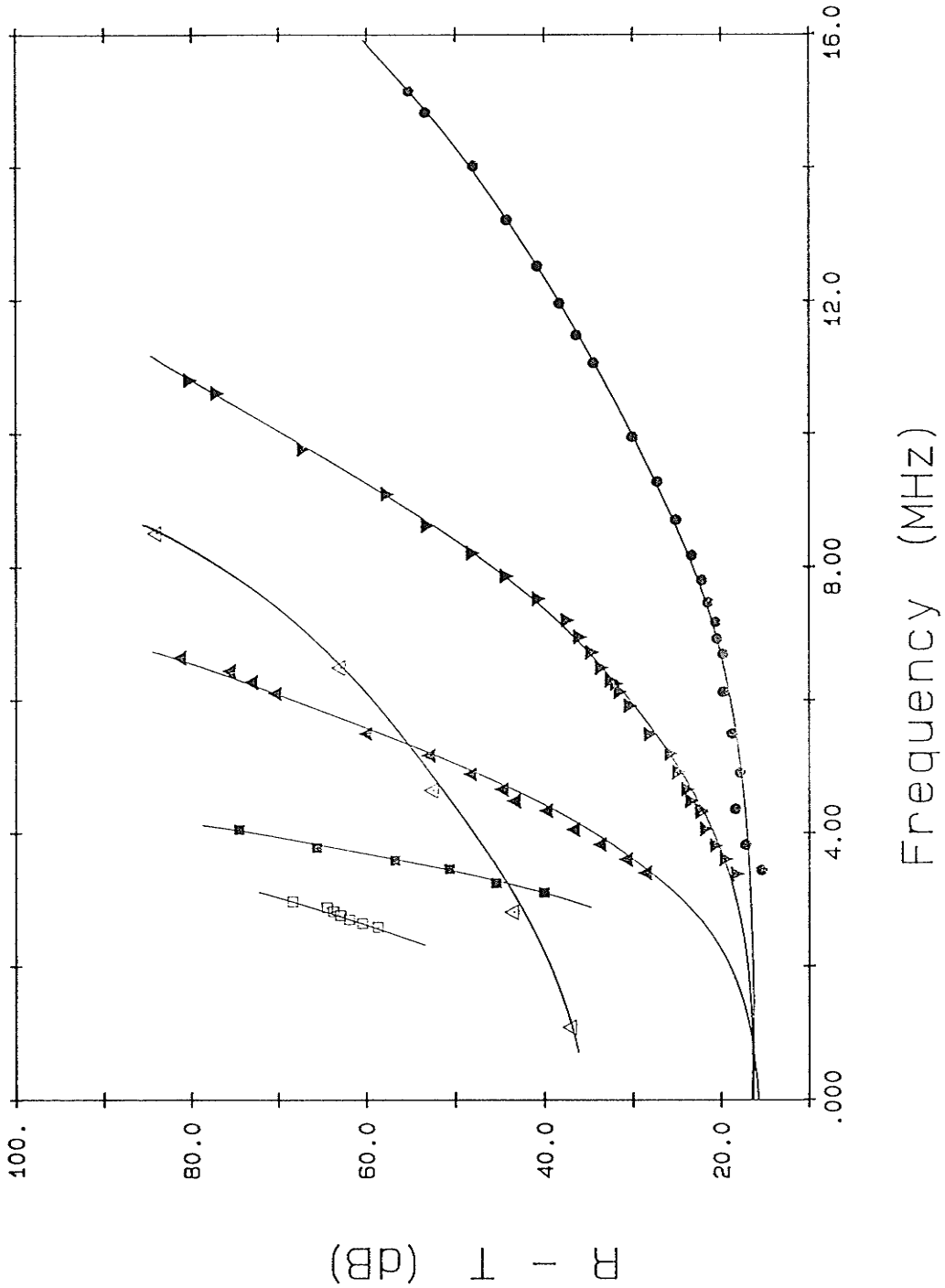

Figure V-4a: Longitudinal pulses: relative amplitude difference of the reflected (R) and transmitted (T) pulse heights versus frequency. Four of the sets of data points were gathered with the polymer transducers: #22 (●), #21 (▼), #20 (▲), and #19 (■); one set was gathered with the PZT pair: #19 (□); sample #20 was thinned and the 1 MHz transducers were used for ultrasonic measurements (Δ).

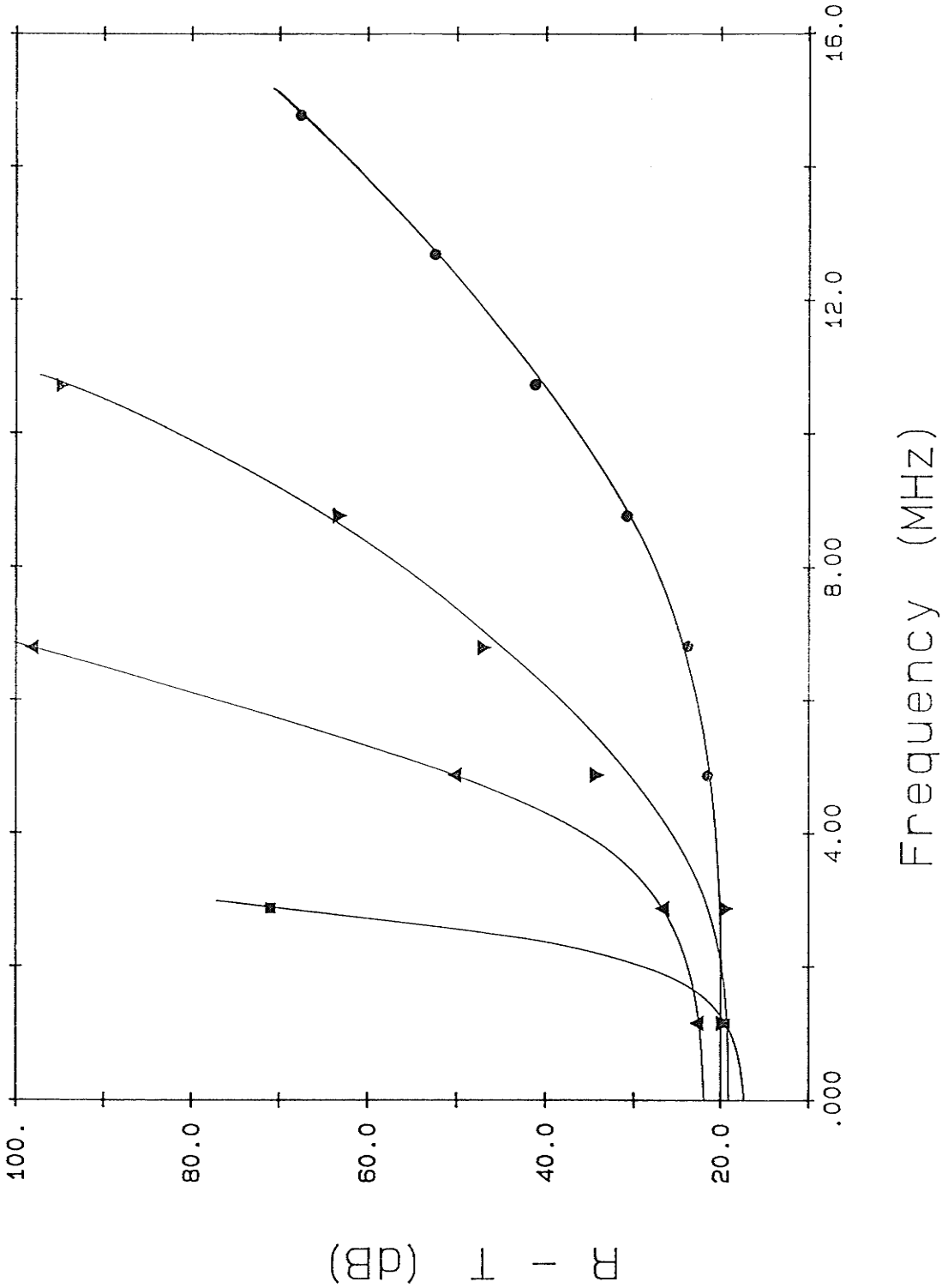

Figure V-4b: Transverse pulses: relative amplitude difference of the reflected (R) and transmitted (T) pulse heights versus frequency. The data points were gathered with the 1 MHz PZT transducers: #22 (●), #21 (▼), #20 (▲), and #19 (■).

of all the samples, it is necessary for each curve to have both an independence of sample thickness and a common baseline.

Each sample was of a different thickness, and even different measurements performed on the same sample usually resulted in a variation of thickness due to some compression. The variable of sample thickness is eliminated by dividing the measured attenuation curves of the samples by the measured sample thicknesses. This assumes that the attenuation of a sample is inversely proportional to the sample thickness, as indeed is found to be the case for sample #20 as shown in Figure V-5 . The attenuation curve in this figure is a composite of attenuation data of sample #20 at two different thicknesses. For the first set of attenuation measurements, the thickness of sample #20 was 894 μm ; it was then thinned to 311 μm for the second set of attenuation measurements in order to extend the frequency range of the attenuation data. Figure V-5 shows that the shapes of the two attenuation curves are well matched (after subtracting baselines as discussed next), and therefore dividing the attenuation curves of each sample by its thickness is a good representation of the measured attenuation.

Each of the attenuation curves of Figure V-4 have been extrapolated to zero frequency to determine the attenuation offset of each baseline. The extrapolated baselines were expected to be different for each curve due to various factors contributing to the offset of each, the most prominent factor of which was the impedance mismatch between the samples and the quartz delay rods. The acoustic impedance Z_i of a material at zero frequency and attenuation is related to the material density ρ_i and velocity v_i such that $Z_i = \rho_i v_i$, as stated in Appendix C . The longitudinal and transverse acoustic impedance for

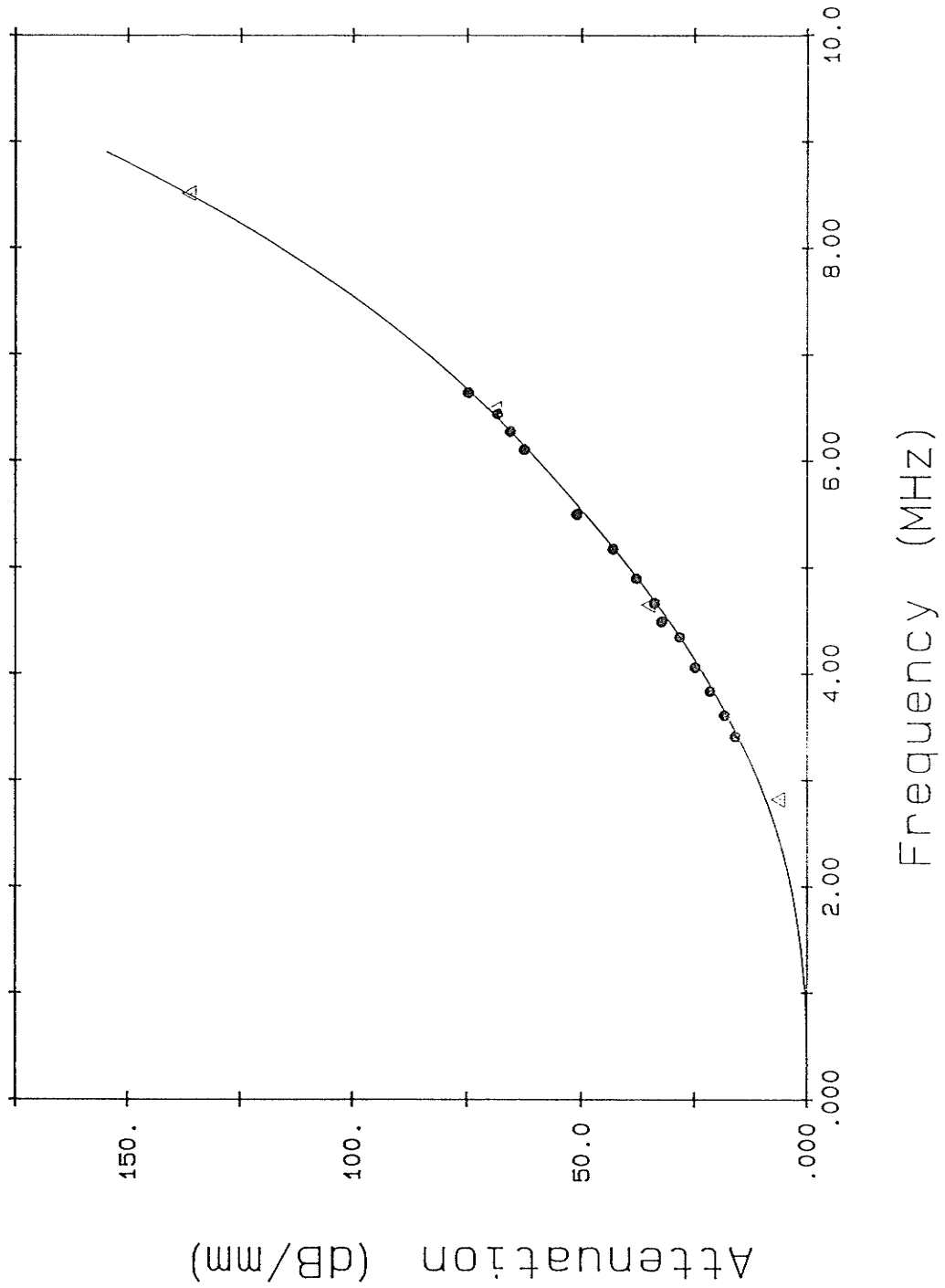

Figure V-5: The frequency dependence of the attenuation curve is shown to be independent of sample thickness in this figure. Polymer transducers were used to measure the attenuation of longitudinal ultrasonic pulses through sample #20 , thickness 0.894 mm (●). The sample was thinned to 0.311 mm , and 1 MHz longitudinal transducers were used to repeat the attenuation measurements (Δ). Note that a different baseline was subtracted from each curve.

each sample, as calculated from the measured density and velocities, are listed in Table V-5 . The impedances of the fused quartz delay rods are also included in this table, as calculated from values in literature [Weast, 1989].

There is a large impedance difference between the quartz delay rods and the samples, and this causes a large portion of the incident wave to be reflected. However, the size of the mismatch varies for each sample and it affects the relative amplitude of the reflected and transmitted pulse. The fraction of the power reflected from the first interface (R) and transmitted through both interfaces (T) is given by the coefficients that have been calculated in Appendix C (Equations (C-43 and 44)) for a short pulse and equal the following when there is no attenuation:

$$R = \left\{ \frac{1 - z}{1 + z} \right\}^2 \qquad \text{(V-2)}$$

and

$$T = \frac{16z^2}{(1 + z)^4} \qquad \text{(V-3)}$$

where $z = Z_{sample} / Z_{delayrod}$. The power differences of the reflected and transmitted pulses relative to the incident pulse arising from the impedance mismatch are listed (in decibels) in Table V-6 (10 log R and 10 log T).

Another contribution to the offset of the attenuation curves is the fraction of the area of the transducer which was bonded to a sample. At the first interface, the portions of the transducer not in contact with the sample essentially completely reflect the incident wave. Thus the ratio of the sample to transducer areas is the fraction by which the transmitted signal is reduced relative to the incident wave. Most

Table V-5a

Acoustic Impedances at Zero Frequency and Attenuation for Longitudinal Waves

Sample	Density (kg/m^3)	Velocity (m/s)	Impedance ($\times 10^6 kg \cdot s^{-1} m^{-2}$)
19	724	560 ± 20	0.405 ± 0.014
20	796	742 ± 9	0.591 ± 0.007
21	942	1161 ± 7	1.04 ± 0.006
22	1050	1550 ± 20	1.63 ± 0.02
Fused Quartz	2200	5900	13.0

Table V-5b

Acoustic Impedances at Zero Frequency and Attenuation for Transverse Waves

Sample	Density (kg/m^3)	Velocity (m/s)	Impedance ($\times 10^6 kg \cdot s^{-1} m^{-2}$)
19	724	260 ± 10	0.188 ± 0.007
20	796	495 ± 6	0.394 ± 0.005
21	942	815 ± 20	0.77 ± 0.02
22	1050	1076 ± 13	1.13 ± 0.02
Fused Quartz	2200	3750	8.3

Table V-6a

Contribution of Impedance Mismatch and Area Mismatch to the Attenuation Offset of Longitudinal Waves

#	$\frac{Z_2}{Z_1}$	10 × log R	10 × log T	$\frac{A_s}{A_t}$	$20\log\frac{A_s}{A_t}$	$20\log\frac{V_R}{V_I}$	$20\log\frac{V_T}{V_I}$	Calc. Offset (dB)	Extrap. Offset (dB)
19	0.0312	-0.54	-18.6	0.25	-12	-0.12	-31	31	13.9
				0.07	-23	-0.13	-42	42	41
20	0.0455	-0.79	-15.6	0.20	-14	-0.15	-30	30	15.1
				0.05	-26	-0.04	-42	42	40.6
21	0.0800	-1.39	-11.2	1.00	0	-1.42	-11.1	9.7	16.3
22	0.125	-2.18	-8.07	0.85	-1.4	-1.78	-9.6	8.8	16.1

Table V-6b

Contribution of Impedance Mismatch and Area Mismatch to the Attenuation Offset of Transverse Waves

#	$\frac{Z_2}{Z_1}$	10 × log R	10 × log T	$\frac{A_s}{A_t}$	$20\log\frac{A_s}{A_t}$	$20\log\frac{V_R}{V_I}$	$20\log\frac{V_T}{V_I}$	Calc. Offset (dB)	Extrap. Offset (dB)
19	0.0227	-0.39	-21.2	0.25	-12	-0.10	-33	33	16
20	0.0475	-0.83	-15.2	0.20	-14	-0.16	-29	29	22
21	0.0928	-1.62	-10.1	1.00	0	-1.62	-10.1	8.6	19
22	0.136	-2.38	-7.50	0.85	-1.4	-2.0	-8.9	6.9	20

samples had a different cross sectional area than the transducer because in the sample preparation process, pieces sometimes either broke or were

cut from the samples. At the second interface, the voltage detected by the transmission transducer is

$$V_T = \frac{A_s}{A_t} T^{1/2} V_I \qquad \text{(V-4)}$$

where V_T is the voltage of the transmitted signal, V_I is the incident voltage, A_s is the cross sectional area of the sample, and A_t is the cross sectional area of the transducers. The relative size of the transmitted voltage to the incident voltage can be expressed in decibels:

$$20 \log\left\{\frac{V_T}{V_I}\right\} = 20 \log\left\{\frac{A_s}{A_t}\right\} + 10 \log T \, . \qquad \text{(V-5)}$$

If we consider the reflected wave at the first interface, the region of the transducer which is not in contact with the sample essentially completely reflects the incident voltage, while the portion which is in contact is dependent upon the reflection coefficient. Therefore the detected reflected voltage is

$$V_R = \left\{1 - \frac{A_s}{A_t}\right\} V_I + \left\{\frac{A_s}{A_t}\right\} R^{1/2} V_I \, , \qquad \text{(V-6)}$$

with the assumption that there is no interference due to a possible relative phase shift between the two terms (see §C:5) . The detected reflected voltage relative to the incident voltage (in decibels) is then

$$20 \log\left\{\frac{V_R}{V_I}\right\} = 20 \log\left\{1 - \frac{A_s}{A_t}(1 - R^{1/2})\right\} \, . \qquad \text{(V-7)}$$

As it can be seen from Table V-6 , the offsets obtained from these calculated factors are in considerable disagreement with the offsets extrapolated from the graphs, although it can be noted that the baseline extrapolation obtained from each curve is approximately constant for each set of transducers. This density independence of the baseline does not correspond with the calculations and must be attributed to other causes. One contributing factor to the offset may be mode conversions from longitudinal to shear ultrasonic waves or vice versa, but the magnitude of this factor has not been measured. Another contributing factor is the degree of parallelism of the delay rod faces, but as shown next, it cannot account for the discrepancies noted in Table V-6 .

Consider a circular transducer of radius r_o that is non-parallel to a sample. If the maximum difference of separation between the transducer and the sample is a distance of $\pm\delta_o$ (at the edge), then at a distance x from the centre, the phase of the wave differs by $\phi(x) = 2\pi\delta_o x/(r_o\lambda)$ so that the total amplitude A_T detected by the entire transducer is

$$A_T = A\int_{-r_o}^{r_o} \cos\{2\pi\delta_o x/\lambda r_o\}\left\{r_o^2 - x^2\right\}^{1/2} dx$$

$$\cong A(\pi\delta_o/\lambda r_o)^2\int_{-r_o}^{r_o} x^2\left\{r_o^2 - x^2\right\}^{1/2} dx$$

$$\cong A\pi r_o^2[1 - (\pi\delta_o/16\lambda)^2] \qquad \text{(V-8)}$$

which is proportional to the amplitude A of the wave and the surface area πr_o^2 of the transducer. The shortest wavelength, and hence the

candidate for the greatest phase cancellation, of all the ultrasonic measurements was $\lambda \cong 100\ \mu m$. With $\delta_o = 4\ \mu m$, the greatest reduction of the detected amplitude due to phase cancellation is only ~0.07 dB , insufficient to explain any of the discrepancies of Table V-6 .

Another possible contributing factor is bond losses, since the quality of the bond could strongly affect the amount of signal transmitted. Damping by bulk quantities of a viscous material would be expected to vary as the square of the frequency, but when ultrasonic vibrations were passed through bonded delay rods alone, the bonds were routinely made sufficiently thin so as to cause nearly no attenuation. The quality of a sample/delay rod bond may not be as good as that of two delay rods since the sample surfaces are porous and more resilient, and the applied pressure must be limited to prevent destruction of the samples. The bonding agent may have provided only a relatively weak coupling for vibrational transmission across the delay rod/sample interface although investigation of this possibility is difficult. If the bond loss factor was significant, a smaller fraction of the pulse would be transmitted resulting in a positive contribution to the calculated offset. One might expect this effect to be most significant for the less dense, more fragile samples, but the opposite is found to be the case when the calculated and extrapolated baselines are compared. Therefore there is some other contributing factor which has not been identified. Further analysis of the attenuation data was done using the values of the extrapolated baselines since most of the calculated values are highly unlikely if compared to the attenuation data curves.

The attenuation of the samples is expected to be zero at zero frequency so that the extrapolated baseline found for a sample was

subtracted from its attenuation curve, giving all the curves a common origin (Figures V-6 and 7). The attenuation of each curve increases strongly with frequency, and the sharpness of the curve increases as $f-f_c$ decreases. At the highest attenuations of each curve, the mean free path $\ell(\omega) = \alpha^{-1}(\omega)$ is less than the wavelength of the pulse. This is indicative of a breakdown of a propagating wave description and is suggestive of a crossover to localized vibrations.

§V: 3.2 — Scaling of the Ultrasonic Attenuation

The correlation length ξ is a characteristic length scale of a sample; it marks the boundary between Euclidean and fractal space and is a measure of the average hole size of a sample. Single-parameter scaling states that any property that depends on length scale for lengths greater than the correlation length should scale with ξ. As mentioned in §II:2.1 , the ultrasonic attenuation consists of inelastic and elastic components. If the inelastic portion is insignificant relative to the elastic portion, then the attenuation $\alpha(\omega)$ can be associated with the elastic mean free path of the system $\ell(\omega)$ such that $\alpha(\omega) = \ell(\omega)^{-1}$, and it would be expected that $\ell(\omega)$ should scale with the correlation length. This means that if each attenuation curve was scaled with the correlation length of the corresponding sample, a single attenuation curve would be expected.

Independent measurements of the correlation length have not been performed, making it necessary to find an alternative scaling length

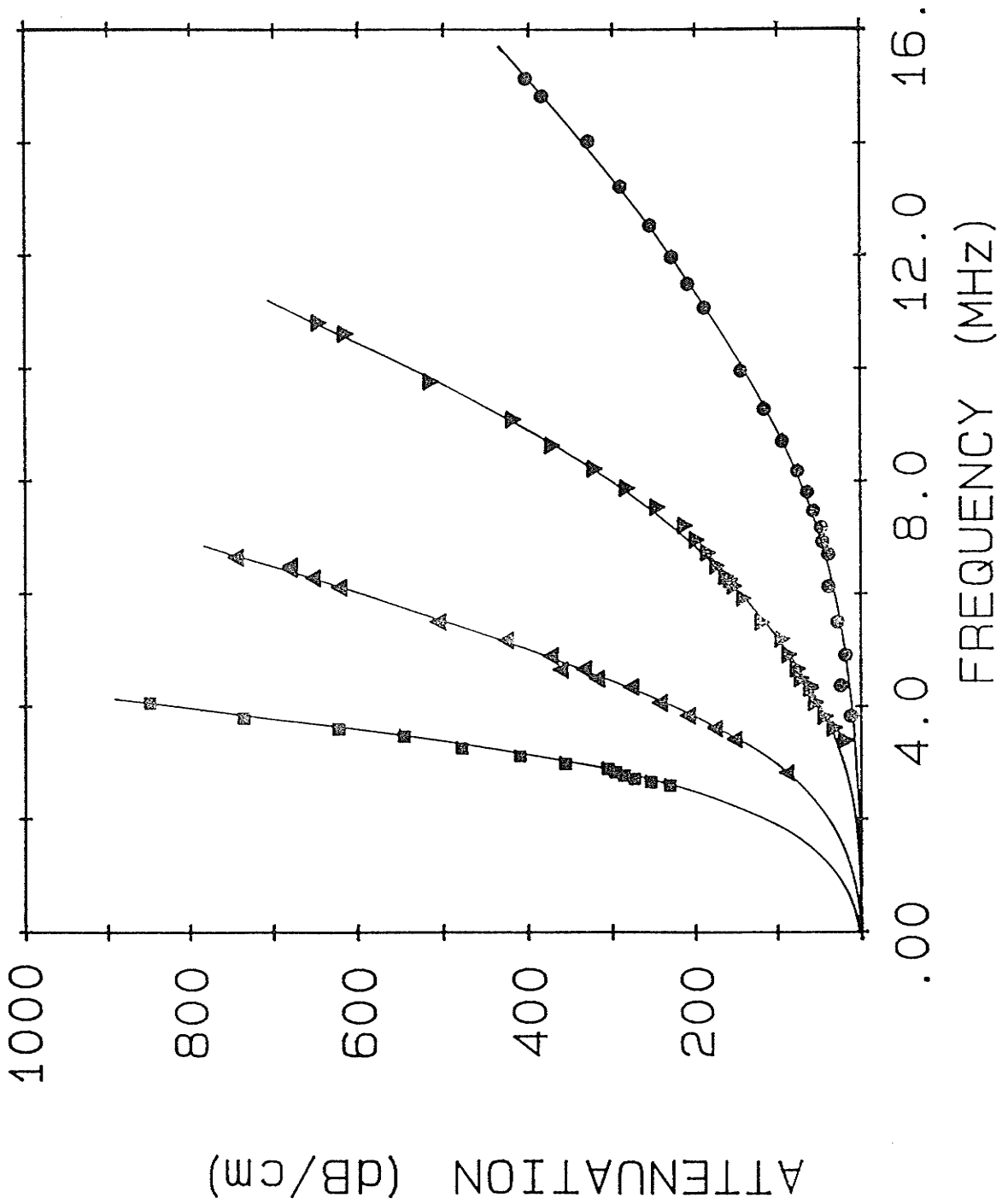

Figure V-6: The longitudinal attenuation data of Figure V-4a expressed in absolute units. The attenuation curves (#22 (●), #21 (▼), #20 (▲), and #19 (■)) have a common origin and are independent of sample thickness.

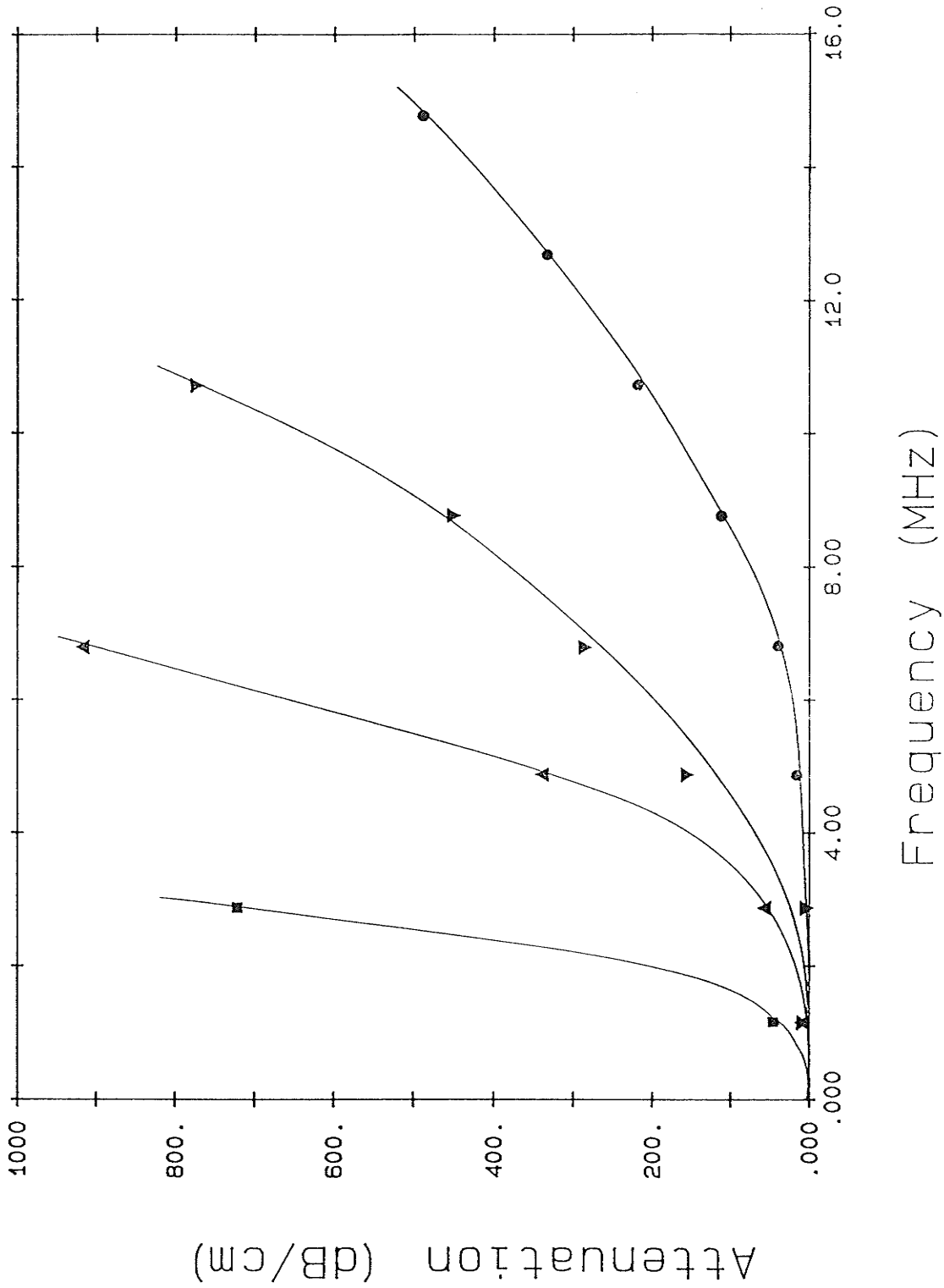

Figure V-7: The transverse attenuation data of Figure V-4b expressed in absolute units. The attenuation curves (#22 (●), #21 (▼), #20 (▲), and #19 (■)) have a common origin and are independent of sample thickness.

with which to scale all of the attenuation data. An empirical scaling length that can be determined directly from the data is the value of the mean free path at frequency ω^* such that the mean free path and wavelength are equal. At this frequency, the intensity of the ultrasonic wave drops to 1/e of its value as the wave propagates a single wavelength, a condition suggestive of a crossover to localized modes; it differs from the Ioffe-Regel condition discussed in §II:2.1 by a factor of 2π. For samples with different packing fractions f_i, this scaling length, ℓ_f^*, is defined by $\ell_f^* \equiv \ell(\omega_f^*) = \lambda(\omega_f^*)$, where $\lambda(\omega_f^*) = 2\pi v/\omega_f^*$. If single-parameter scaling arguments hold and if the measured attenuation is caused predominantly by elastic scattering, then the values $\ell^*(f_i)$ (and $\lambda^*(f_i)$) extracted from the measured attenuation curves should be proportional to $\xi(f_i)$ and can themselves be used as scaling factors. If the attenuation curves are scaled by ℓ_f^* and the curves collapse to a single curve, then both assumptions hold and all of the data has been unified for further analysis.

The scaling lengths $\ell^*(f_i)$ are easily obtained from the attenuation curves if the attenuation α of Figures V-6 and 7 is expressed in terms of inverse length and if the frequency axes are converted to units of inverse wavelength by dividing by the sample velocities, done for Figures V-8 and 9. The point at which the line $\alpha = \lambda^{-1}$ intercepts the attenuation curves corresponds to the chosen scaling length ℓ_f^* and the values obtained for each attenuation curve are listed in Table V-7. The uncertainties of the extracted scaling lengths arise from the uncertainty of the extrapolated baselines.

The validity of this scaling procedure is shown in Figure 10 where both the attenuation α and the inverse wavelength λ^{-1} for each

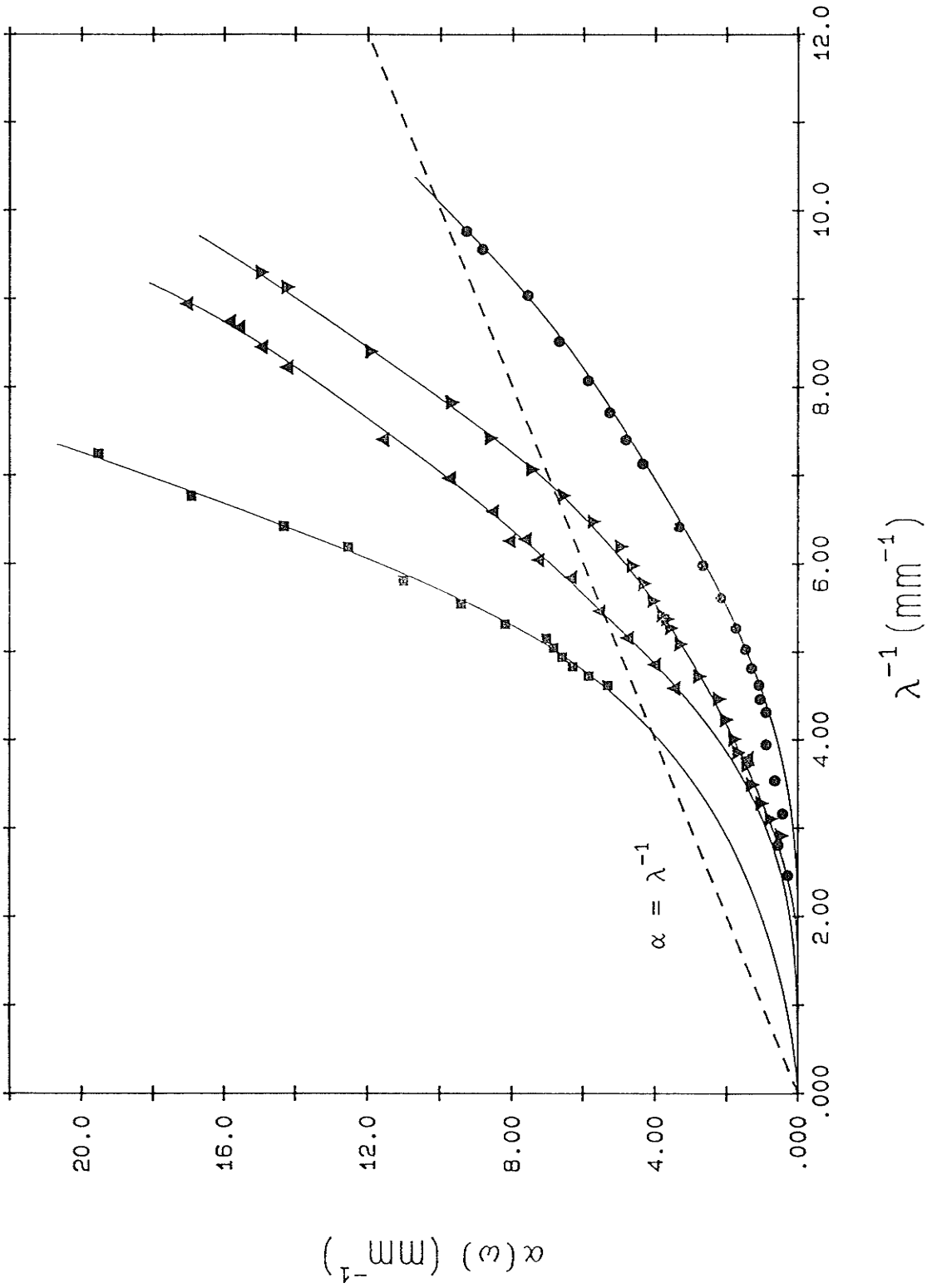

Figure V-8: Extraction of the scaling lengths $\ell^*=\lambda$ for the longitudinal attenuation data of Figure V-6 for each sample (#22 (●), #21 (▼), #20 (▲), and #19 (■)).

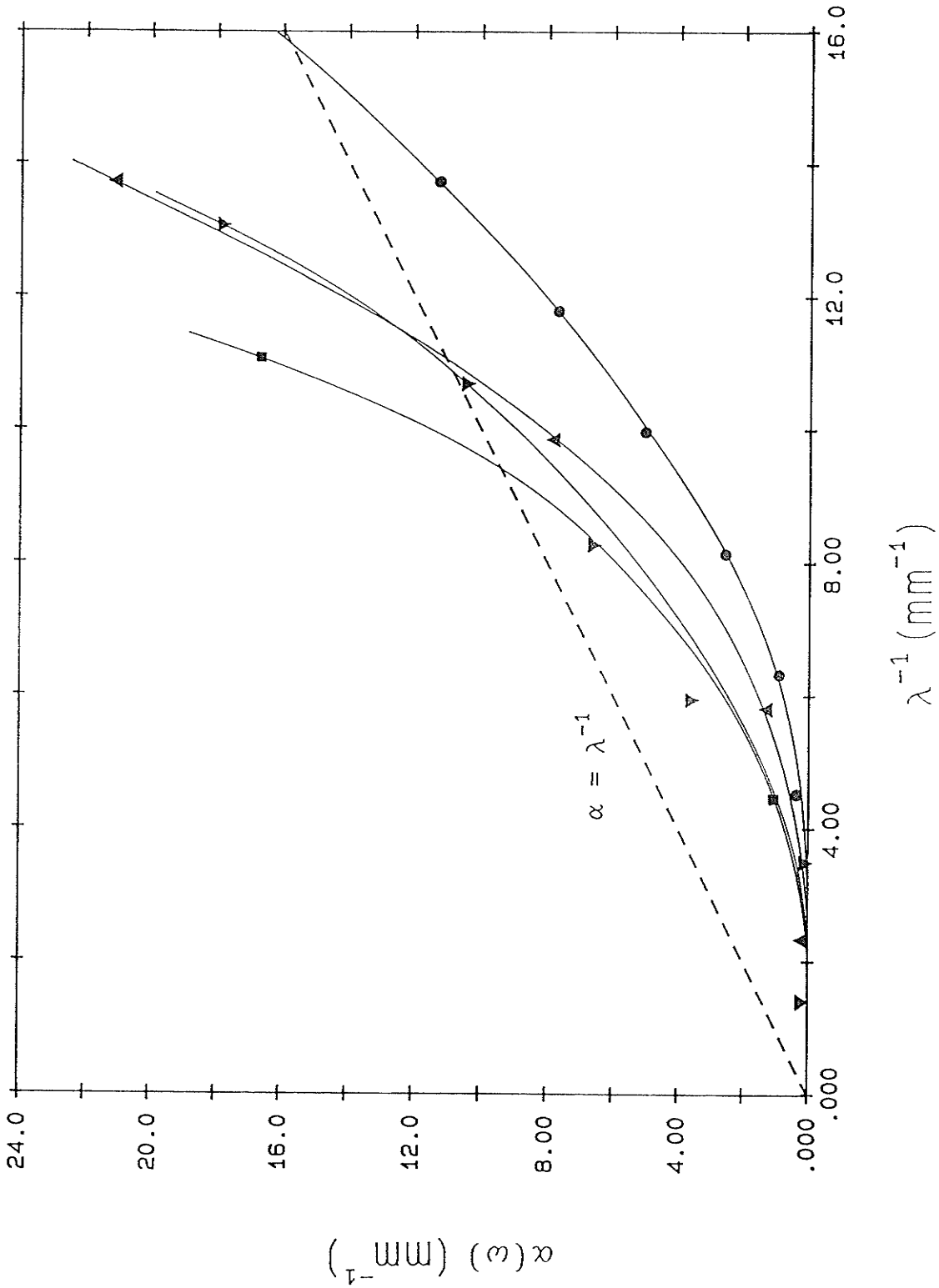

Figure V-9: Extraction of the scaling lengths $\ell^* = \lambda$ for the transverse attenuation data of Figure V-7 for each sample (#22 (●), #21 (▼), #20 (▲), and #19 (■)).

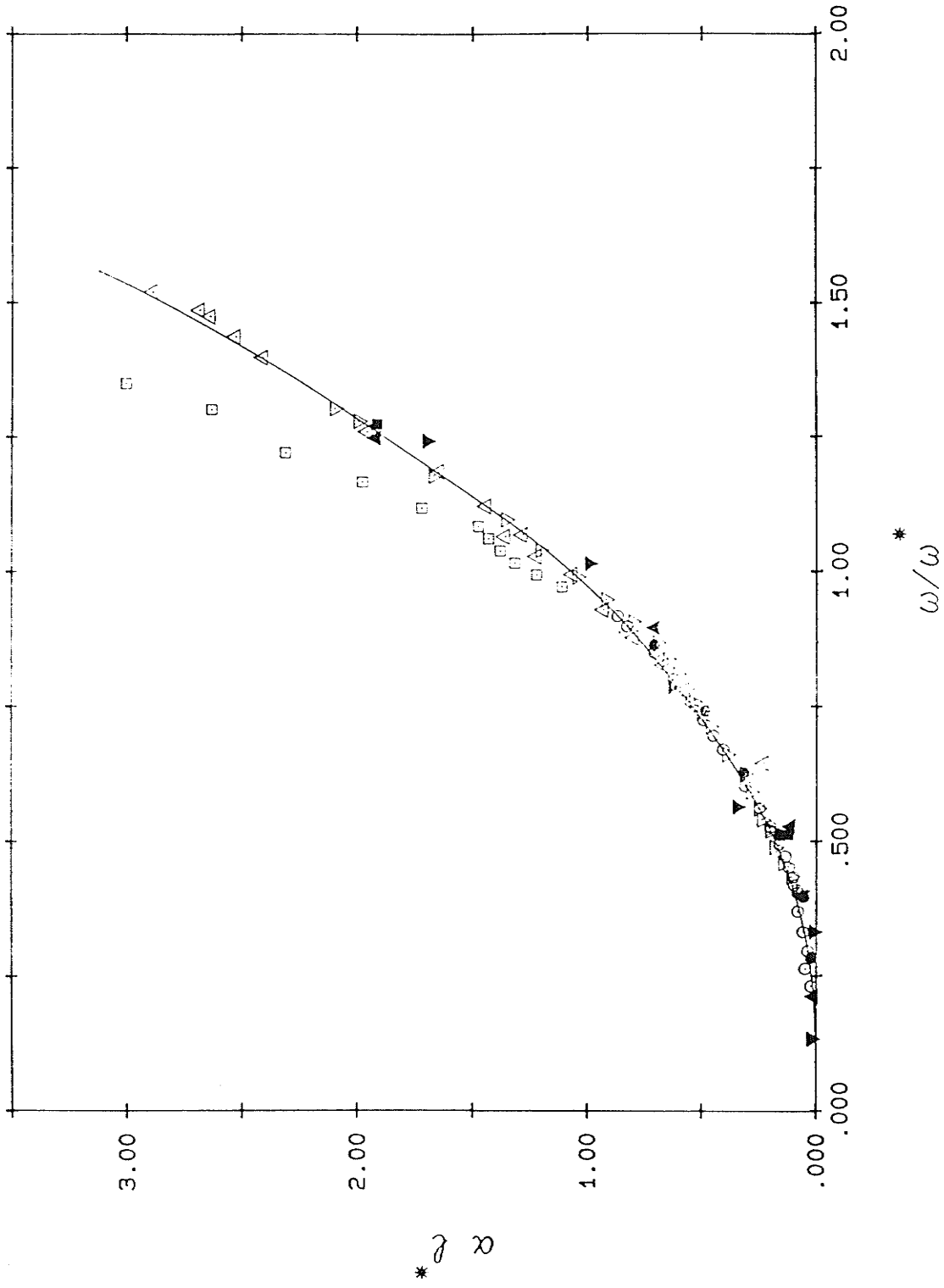

Figure V-10: The longitudinal (open,○) and transverse (solid,●) attenuation data of Figures V-8 and 9 scaled by ℓ^* for each sample (#22 (●), #21 (▼), #20 (▲), and #19 (■)). Note that for the abscissa, $\ell^*\lambda^{-1} = \omega/\omega^*$.

Table V-7

Scaling Lengths and Frequencies

of Samples #19-22

Sample #	ℓ_f^*		$\omega_f^*/(2\pi)$	
	Long. (μm)	Shear (μm)	Long. (MHz)	Shear (MHz)
19	210 ± 60	115 ± 10	2.4 ± 0.7	2.4 ± 0.2
20	170 ± 20	91 ± 5	4.2 ± 0.5	5.4 ± 0.3
21	140 ± 10	95 ± 10	8.2 ± 0.6	8.6 ± 0.9
22	94 ± 4	63 ± 4	16.0 ± 0.7	17 ± 1

curve are multiplied by the corresponding value of ℓ^* . The scaled data of both vibrational modes of all the samples can be seen to fall on the same curve and therefore support the single variable scaling arguments for ℓ_f^* , although the longitudinal attenuation data of sample #19 does not scale as well as those of the other samples.

The frequency dependence of the scaled attenuation can be obtained by plotting the data on logarithmic axes (Figure V-11) . As described in §II:2.2 , it would be expected that at low frequencies, when the wavelength is much larger than the typical inhomogeneity, Raleigh scattering would be dominant and the attenuation would be expected to be proportional to ω^4 . It is certainly plausible to draw a line of slope 4.0 as a fit of the data for the lower scaled frequencies; the scatter of the points reflects the uncertainty of the extrapolated baselines. At the higher frequencies, the data is best described by a line of slope 2.35 ± 0.10 and the fitted lines of the two regions intersect when $\omega/\omega^* \cong 0.5$.

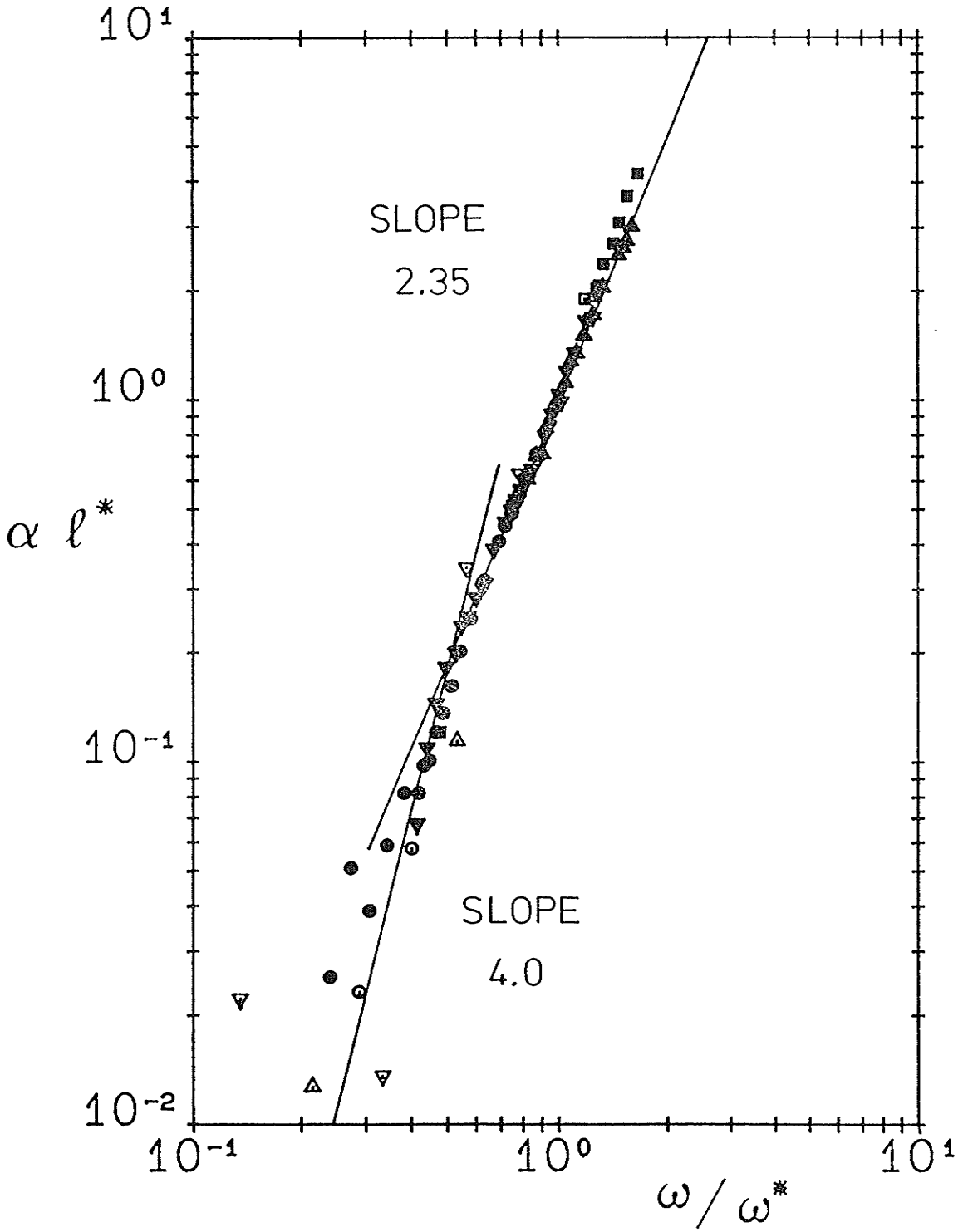

Figure V-11: Logarithmic plot of the longitudinal (solid,●) and transverse (open,⊙) attenuation data of Figures V-8 and 9 scaled by ℓ_f^* for each sample (#22 (●), #21 (▼), #20 (▲), and #19 (■)). Note that for the abscissa, $\ell^* \lambda^{-1} = \omega/\omega^*$.

The slope change is rather surprising considering that even at the highest scaled frequency (through sample #20 after thinning), the wavelength (~90 μm) remained much greater than the measured correlation length (~5 μm , from Chapter VI) so that it would be expected that Raleigh scattering would still dominate. Furthermore, since $\lambda \gg \xi$, it is unlikely that the $\omega^{2.35}$ frequency dependence is related to fracton behaviour. It is curious that the observed frequency dependence is the same as that predicted for the fracton relaxation time in the weakly localized fracton regime discussed in §II:2.2 ($1/\tau \propto \omega^{5-3\tilde{d}} \sim \omega^{2.3}$ when d=0.9). However, Equation (II-27b) shows that the predicted frequency dependence of the attenuation in this region is not consistent with our data since $\alpha \sim \omega^{4-\tilde{d}(3-1/D)} \sim \omega^{1.7}$ when $\tilde{d} = 0.9$. Also, at frequencies higher than the observed crossover point $\omega/\omega^{*} \cong 0.5$, there is no corresponding frequency dependence of the velocity as indicated by the delay curves of Appendix D .

The most probable cause of the frequency dependence of the attenuation is the existence of sample inhomogeneities of a length scale larger than ξ . Raleigh scattering holds only if $\lambda \gg d$ where d is the size of the scatterers. Thus a weaker than ω^{4} dependence will occur if there are sample inhomogeneities that are comparable to the ultrasonic wavelength. A micrograph of the surface of sample #20 (prepared as described in §VI:3.1) is presented in Figure V-12 and reveals large scale inhomogeneities on the order of 100 μm , despite the care taken in packing the sample powder before pressing. Previous ultrasonic work on copper sinters by Page and McCulloch [1985] yielded attenuation curves which had a frequency dependence that followed an approximate power law ranging from 1.6 to 2.4 . The longitudinal attenuation

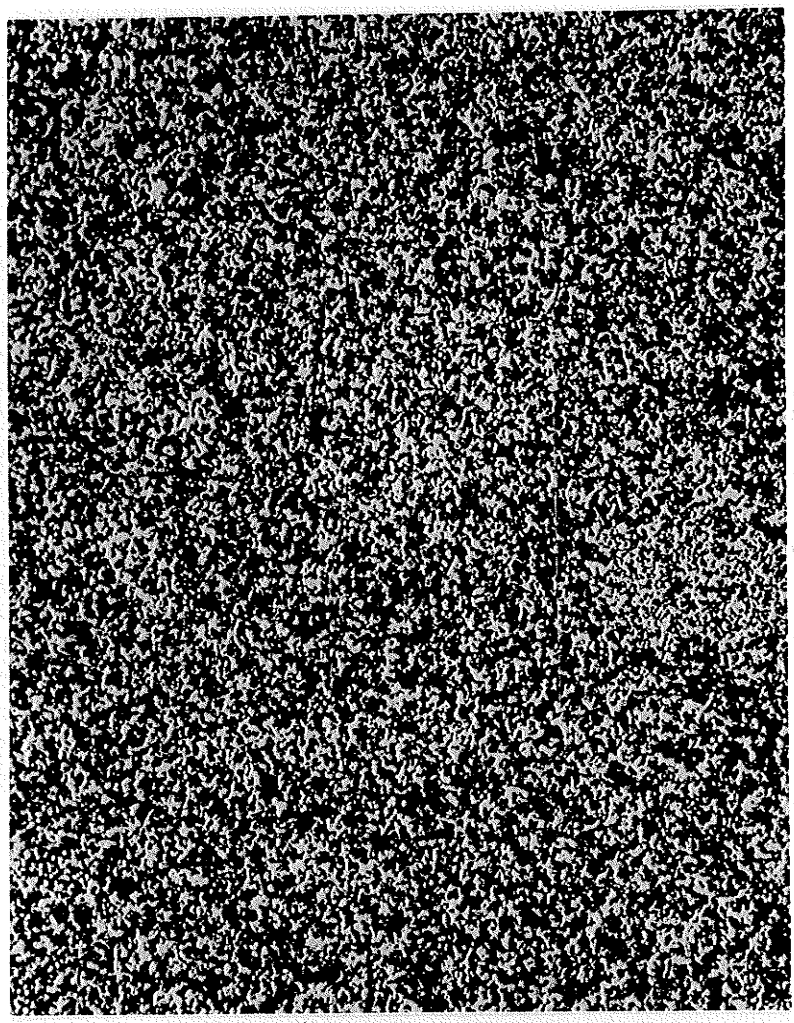

100 μm

Figure V-12: A two dimensional cross section micrograph of sample #20. Large scale inhomogeneities up to a length of about 100 micrometers can be seen.

curves of the samples prepared for this thesis each separately followed a frequency power law within the range $\omega^{2.4 \pm 0.2}$. This means that the homogeneity of the samples was sufficiently consistent that the power law of each sample is essentially the same, and the strength of the frequency dependence of *each* sample was as great as the strongest power law measured by Page and McCulloch. Thus it can be said that although the sample preparation technique did not yield an ideal sample, the method employed did improve the quality of the samples compared to previous techniques.

If the measured values of ℓ_f^* do actually scale with the correlation lengths ξ_f, then from Equation (II-2) it is seen that a graph of $\log(\ell_f^*)$ versus $\log(f-f_c)$ (Figure V-13) should be linear with a slope of $-\nu = -0.88$. The limited number of data points lack adequate precision to meaningfully fit a straight line to them. Instead, lines of the predicted slope were drawn as guides to the eye to show that such lines are certainly plausible although there is considerable scatter. What is startling is the fact that the extracted values of ℓ_f^* (Table V-7) differ for the longitudinal and transverse curves of each sample. This result is counterintuitive since ℓ_f^* is expected to be proportional to ξ_f, independent of the mode of the propagating wave.

From the scaling lengths obtained for each sample, one observes that at the same wavelength, the attenuation of the longitudinal wave is greater than that of the transverse wave. One might be tempted to explain the scaling length discrepancy by the difference of strains applied to the samples for the two different modes, but this would require a sample to be sufficiently compressed that the attenuation per unit length was seriously reduced. It is true that the samples of lower

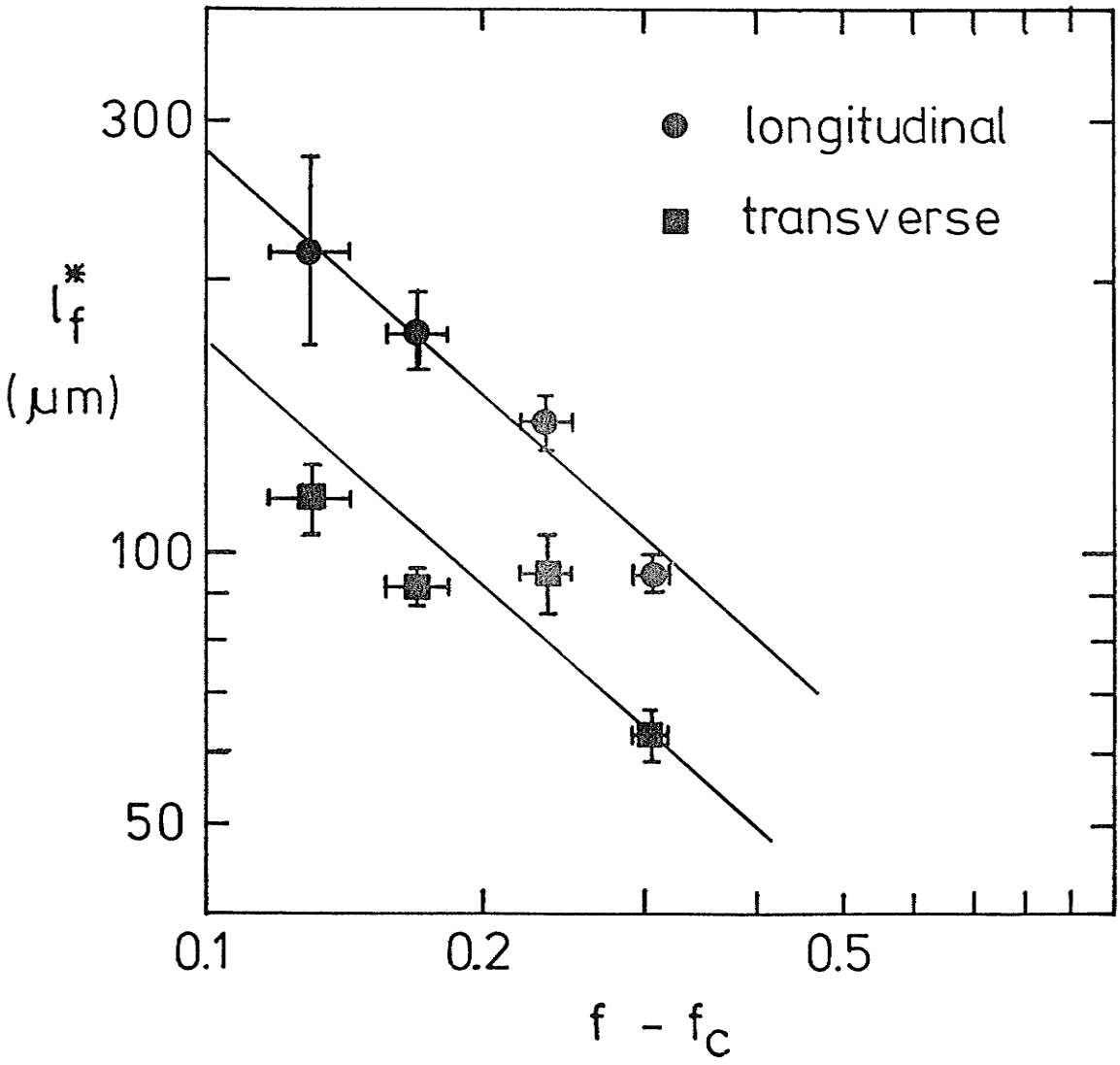

Figure 13: Logarithmic plot of scaling length ℓ_f^* versus $f-f_c$ for longitudinal (●) and transverse (■) data. The slope predicted by theory ($-\nu = -0.88$) is drawn as a guide to the eye.

packing fraction were compressed more when collecting transverse data than for longitudinal, but this was not the case for the two samples of higher packing fraction. However the discrepancy of the scaling lengths exists for *all* of the samples; thus the difference of strain is an inadequate or at very most an incomplete explanation for the scaling factor discrepancy.

When the f-f_c dependence of the corresponding values ω_f^* are considered (Table V-7 and Figure V-14), it can be seen that ω_f^* does *not* seem dependent on the mode of the ultrasonic wave. Taken at face value, these data appear to suggest that there may be a unique scaling frequency $\omega_c \propto \omega_f^*$ that is independent of polarization mode. Alternatively, it can be observed that the calculations of ω_f^* are not dependent upon the velocity v whereas the extrapolated values of $\ell_f^* = \lambda^* = 2\pi v/\omega_f^*$ are, suggesting that the measured velocities could somehow be involved in the offset discrepancy of the measured scaling lengths (without changing their dependence on f-f_c). Since the wavelengths of the highest transverse frequencies were shorter than those of the longitudinal pulses, sample inhomogeneities would have a greater effect on those delay points and could influence the zero-period extrapolations. However if the transverse delay curves of Appendix D are studied, it is seen that the extrapolated transit time would change only by a small amount if the greatest period points are omitted from the fit. A transverse transit time decreased by ~20% cannot possibly be extracted from the curves, as would be required to account for the scaling length discrepancy. Thus the delay extrapolations are reliable and the mode-dependent scaling length cannot be attributed to inaccurate velocity measurements.

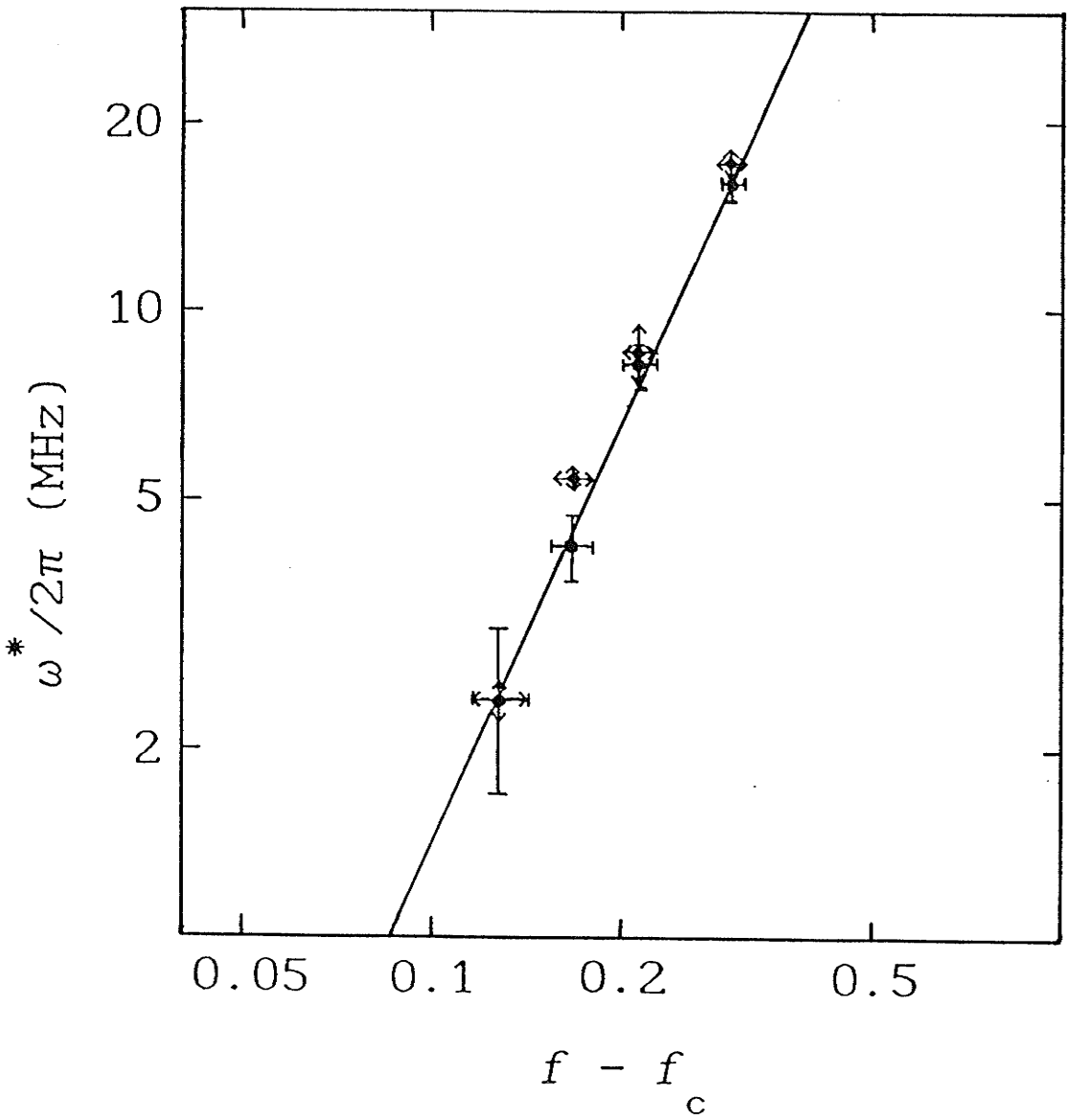

Figure 14: Logarithmic plot of scaling length ω_f^* versus $f-f_c$ for longitudinal (|—●—|) and transverse (←◆→) data. Unlike the dependence of the scaling length ℓ_f^* (cf. Figure 13), the corresponding frequency ω_f^* is independent of the mode of wave propagation.

One disturbing possibility for the scaling length discrepancy is if the measured attenuation actually contains a significant inelastic component. From the scaling lengths obtained for each sample, one observes that the attenuation curves of the longitudinal data rise more sharply than that of the transverse data and it would therefore be necessary for this inelastic mechanism to attenuate longitudinal ultrasonic waves more than transverse. It would *also* be necessary for this inelastic scattering to scale with ℓ^* in the same way as the elastic scattering since the scaling lengths follow the same power law for each mode. One can imagine that if the surface of the glass beads were badly attacked by the acid and the surface became rough, some sort of intergranular friction could occur upon propagation of shear or compressional waves. The magnitude and the frequency dependence of this absorption mechanism would involve many factors dealing with the microstructure of each sample.

Chapter VI: Measurement of the Correlation Length and the Fractal Dimension

An experiment complimentary to the acoustic measurements was conducted to determine the crossover length ξ and the fractal dimension D of the sinters. The method that was used involved measuring the intensity of light transmitted through two identical transparencies made from a micrograph of a sample cross section. When one transparency is displaced a distance R with respect to the other transparency, the transmitted intensity is proportional to the area autocorrelation function which is shown to be proportional to R^{D-3} for $a \ll R \ll \xi$ (where a is the particle radius) and to be independent of R for $R \gg \xi$.

This chapter is self-contained and contains the theory, experimental procedure, and data analysis used to procure the values ξ and D.

§VI: 1 — THEORY

Following the notation of Cusack [1987], consider N fixed particles located at site $\underline{r}_i$ in a volume V. The single-particle density function is describe by a delta function:

$$\nu(\underline{r}) \equiv \sum_{i=1}^{N} \delta(\underline{r} - \underline{r}_i) \qquad \text{(VI-1)}$$

so that the total number of particles is given by integrating the single-particle density function over the volume V:

$$\int_V \nu(\underline{r})d\underline{r} = N \quad . \qquad \text{(VI-2)}$$

The normalized autocorrelation function of the particle positions in a two-dimensional cross section is given by

$$P_a^{(2)}(\underline{r}) = \frac{1}{N}\int \nu(\underline{r}')\nu(\underline{r}'+ \underline{r})d^2r' \quad . \qquad \text{(VI-3)}$$

It represents the fraction of the total number of particles N that are separated by a distance $\underline{r}$, since $\nu(\underline{r}')\nu(\underline{r}'+ \underline{r})d\underline{r}' = 1$ only if both sites $\underline{r}'$ and $\underline{r}'+\underline{r}$ are occupied, and the integral of $\underline{r}'$ over the two-dimensional cross section of the sample averages over all the initial sites $\underline{r}'$.

The number of particles within a circle of radius R, $N^{(2)}(R)$, is found by summing all the pairs of particles that are separated by r for all $r \leq R$; that is

$$\mathcal{N}^{(2)}(R) = \int_0^R P_a^{(2)}(\underline{r})d\underline{r} \quad . \tag{VI-4}$$

Since $\mathcal{N}^{(2)}(R)$ is proportional to the mass contained in this region

$$\mathcal{N}^{(2)}(R) \propto M^{(2)}(R) \ , \tag{VI-5}$$

then for a fractal distribution of particles (from Equation (II-3b)),

$$\mathcal{N}^{(2)}(R) = C\, R^{D_A} \tag{VI-6}$$

where C is a constant and D_A describes the distribution of particles in the two-dimensional cross section. To relate $P_a^{(2)}(R)$ to D_A, we note that from Equation (VI-4)

$$\begin{aligned} \mathcal{N}^{(2)}(R+\Delta R) - \mathcal{N}^{(2)}(R) &= \int_R^{R+\Delta R} P_a^{(2)}(\underline{r})d^2r \\ &\propto P_a^{(2)}(R)\, R\, \Delta R \end{aligned} \tag{VI-7}$$

and from Equation (VI-6) we obtain

$$\begin{aligned} \mathcal{N}^{(2)}(R+\Delta R) - \mathcal{N}^{(2)}(R) &= C\left\{(R+\Delta R)^{D_A} - R^{D_A}\right\} \\ &\cong C\, D_A\, R^{D_A-1}\, \Delta R \quad . \end{aligned} \tag{VI-8}$$

Thus the autocorrelation function $P_a^{(2)}(R)$ varies with R as

$$P_a^{(2)}(R) \propto R^{D_A-2} \ . \tag{VI-9}$$

The fractal dimension D that describes the distribution of particles in three dimensions ($\mathcal{N}^{(3)}(R) \propto R^D$) is simply related to D_A

of a two-dimensional cross section of the structure. Since $N^{(2)}(R)$ is independent of the orientation of the cross section defined in spherical polar coordinates by $\delta(\theta-\theta_o)$, the number of particles contained within a sphere of radius R is

$$N^{(3)}(R) = \int_0^{\pi} d\theta \int_0^{R} dr\ r \frac{\partial N^{(2)}(r)}{\partial r}$$

$$\propto R^{D_A+1} . \qquad \text{(VI-10)}$$

Thus

$$D = D_A + 1 \qquad \text{(VI-11)}$$

and the autocorrelation function $P_a^{(2)}(R)$ can be written in terms of D:

$$P_a^{(2)}(R) \propto R^{D-3} . \qquad \text{(VI-12)}$$

The particle autocorrelation function of a two-dimensional cross section, $P_a^{(2)}(R)$, can be measured experimentally by the area autocorrelation function (the two-dimensional density autocorrelation function).

The fractal dimension D ($d=3$) and the correlation length ξ can be found experimentally from the area autocorrelation function dependence since for a percolating structure,

$$P_a^{(2)}(R) \propto R^{D-3} , \quad a \ll R \ll \xi \qquad \text{(VI-13a)}$$

$$P_a^{(2)}(R) \propto R^{0} , \quad R \gg \xi . \qquad \text{(VI-13b)}$$

Within the length scale regime $R \ll a$ (where a is the particle radius), the individual particle structure dictates the power dependence of $P_a^{(2)}(R)$. For length scales $R \gg \xi$, the sample is homogeneous and the autocorrelation function is independent of length scale. Between these two regimes lies the length scale range for which the mass of the percolating system follows a fractal power dependence.

§VI: 2 — APPARATUS

Figure VI-1 is a schematic diagram of the apparatus used to measure the area autocorrelation function of the samples. A parallel beam of light was passed through two transparencies of a cross section of a sample and the change of total transmitted intensity was measured with respect to the lag between them. The light source was a 3 mW Spectra-Physics laser of wavelength 6328 Å and a spatial filter was attached to the laser with a threaded screw mount. The stationary transparency holder held metal plates which had a hole cut their center, and razor blades were fastened around the hole so as to form a rectangular hole with well-defined edges. Light passed through this hole and on through the transparencies. The mobile transparency holder was mounted on a travelling microscope stand which could measure displacements to the nearest 0.01 mm. The phototransistor had a maximum output voltage of around 23 V and was powered by a 24 V source.

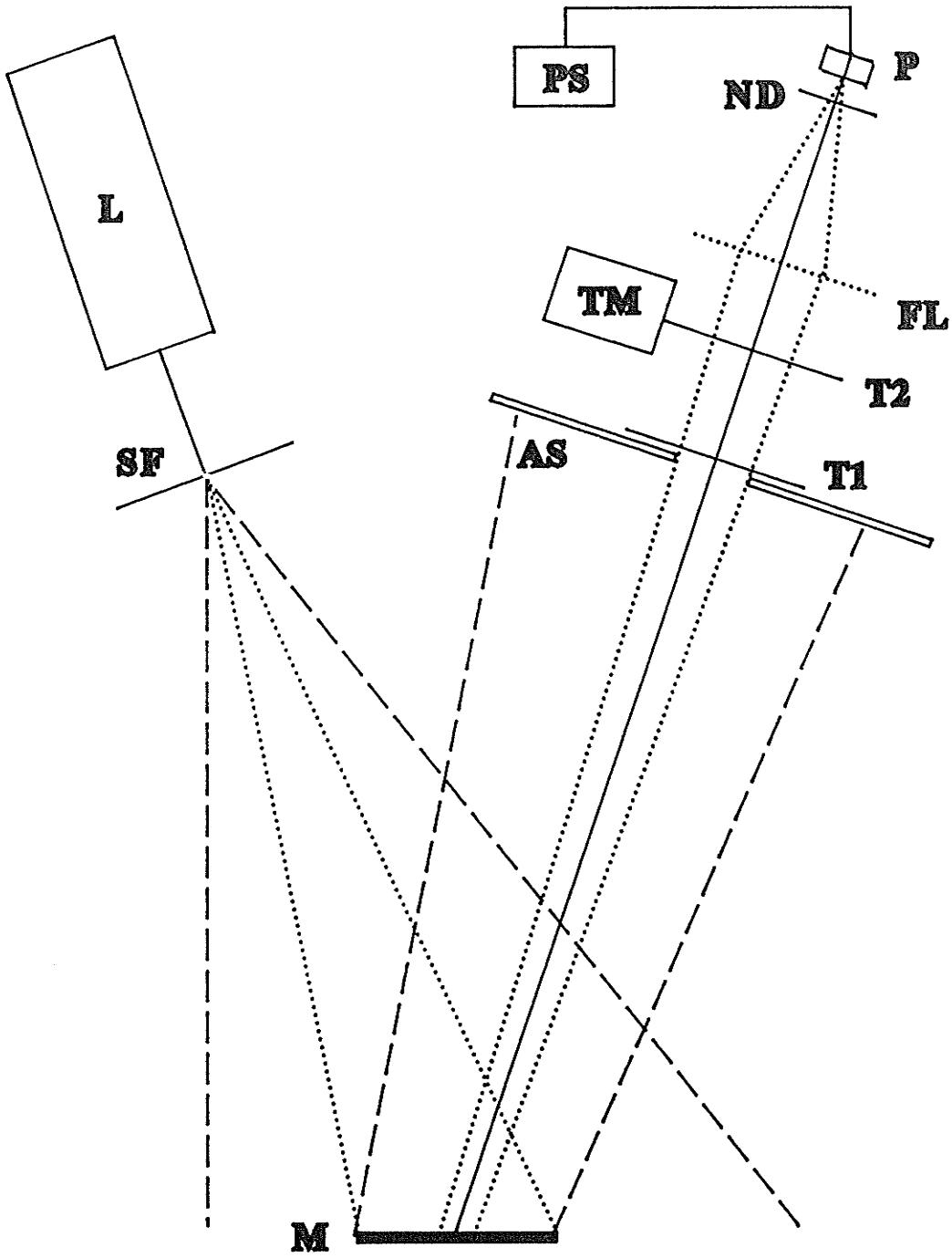

Figure VI-1
Autocorrelation Apparatus

L: Laser
SF: Spatial filter
M: Mirror
AS: Aperture stop
TM: Travelling microscope stand
T1: First transparency
T2: Second transparency
FL: Focusing lens
ND: Neutral density filter
P: Phototransistor
PS: Power supply

§VI: 3 — PROCEDURE

§VI: 3.1 — Sample Preparation

In order to prepare a two-dimensional cross section of the samples, the holes in the samples had to be filled with some substance so that the underlying structure would not be detected in the SEM micrographs. It was found that yellow thermoplastic cement and low temperature red Crown Sticky-Wax were not appropriate materials because they were eroded from the surface pores of the sample during polishing. It was found that Stycast 1266 clear epoxy (Emerson and Cuming Incorporated) was sufficiently hard to remain flat during polishing, and thus it was suitable to impregnate a sample with this substance. However, the epoxy cannot be removed from a sample after the micrographs were taken so that measurements were done on pieces of sample #20 that had already broken from the main body.

A small quantity of epoxy and hardener were weighed and well mixed; bubbles in the epoxy were not of concern as the epoxy was to be placed under vacuum before the sample was immersed. An aluminum foil container was molded to fit at the bottom of a test tube and the epoxy was poured into the foil. A two hole stopper was used to seal the test tube: a rotary pump was connected to one hole and into the other hole a lubricated steel rod was inserted. Attached to this rod was a brass foil platform on which the sample was placed. The pump valve was slowly opened and the epoxy bubbled and foamed until all the bubbles in the

epoxy were liberated and a pressure of about 0.3 torr was registered by the Edwards Pirani 11 gauge. It was at this point that the rod was lowered and the attached brass foil holding the sample was immersed in the epoxy. The immersed sample was left under vacuum overnight while the epoxy cured.

The block of clear epoxy was removed from the test tube and filed until the sample was near the surface. The face of the epoxy opposite the sample was then filed approximately parallel to the sample face. Low temperature red wax was used to mount the block of epoxy on a Model 150 hand lapping fixture from South Bay Technology Incorporated. The impregnated sample was then polished to a 1 μm finish using a procedure similar to that of §III:1.4 .

After polishing, the surface of the sample was cleaned with a soapy solution of Sparkleen (Fisher Scientific) to dissolve the remaining mineral oil without leaving a residue. It was necessary to coat the sample with a thin conducting layer in order to micrograph the sample with the SEM. Without this layer, a charge built up on the sample and details of the surface structure were obscured. A thin carbon coating proved to be a suitable conducting material for obtaining a clear micrograph of the sample.

The micrograph of the sample cross section that was used for measurements (Figure VI-2a) was copied to paper, with the photocopier set on high contrast so that the copy had a limited amount of intermediate grey shades; this made the copy a closer representation of the object described in the theory section. Low contrast areas arising from visible underlying sample details very near the surface were retouched with black and white ink. The retouched, high contrast picture was

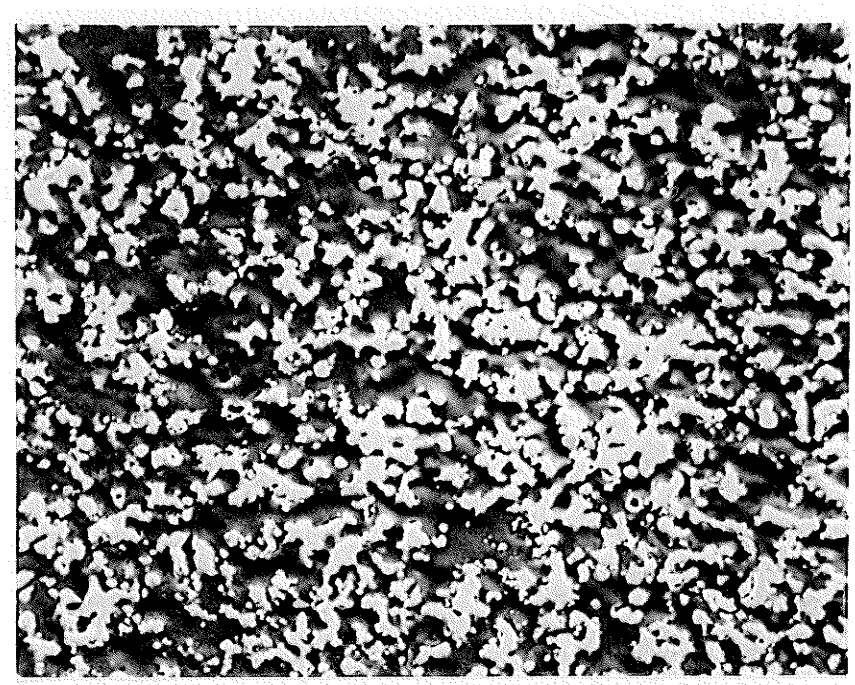

(a) Micrograph of a two dimensional cross section of sample #20

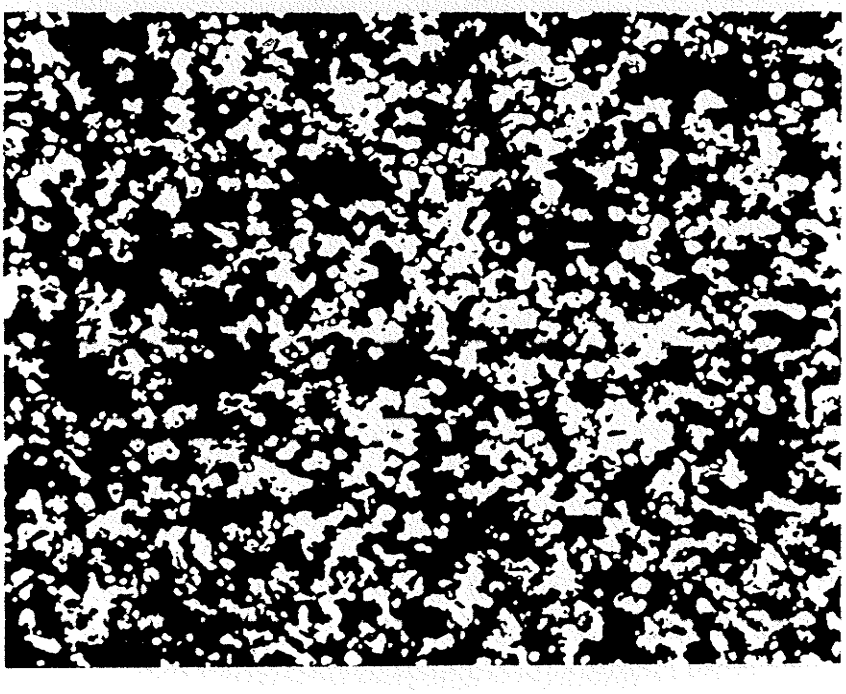

(b) High contrast, retouched photocopy of sample #20 micrograph

Figure VI-2: These figures show a two dimensional cross section of sample #20 . Autocorrelation measurements of figure (b) measured over several sample regions (60 μm × 70 μm) and averaged.

photocopied onto transparency sheets and were used for the area auto-correlation function measurements. A copy of the retouched micrograph can be seen in Figure VI-2b .

§VI: 3.2 — Experimental Preparations

The apparatus was arranged as described in §VI:2 . The laser was turned on about an hour before data was collected to permit its output to stabilize. It was also important to perform the experiment in a room with no air currents. Neglecting either of these factors caused relatively large intensity fluctuations of the measured beam intensity (>5% variation). It was necessary to diverge the laser beam such that cross section transmitted by the aperture stop was illuminated with uniform intensity. Expansion by use of an optical lens was inadequate because lens scratches and dust caused local intensity variations that were unacceptable. Instead, the beam was passed through a spatial filter which consists of a lens with a focal length of about 4mm and a circular pinhole of diameter 70 μm . The pinhole was positioned so that it was placed at the point at which the laser beam was focused. The emerging light was Fraunhofer diffracted and caused any intensity inhomogeneities to be filtered. However, there was still a radial dependence of the emerging circular diffraction pattern. Thus it was necessary to allow the beam to diverge over a sufficient distance so that the radius of the Airy disk (the central maximum) became large enough that the intensity variation over the transparencies was accept-

ably small (≤5%). A mirror was required to achieve the necessary path length even though its optical surface contributed to the registered local intensity variations.

The diverged laser light passed through the two transparencies. Both the angle of divergence of the beam and the distance between the transparencies were sufficiently small that the light could be considered parallel between the transparencies. One transparency was mounted on a stationary holder while the other was mounted on a travelling microscope stand. After transmitting through the two transparencies, the beam was focused by an 11 cm diameter, 20 cm focal length convex lens onto a phototransistor. It was necessary to pass the beam through neutral density filters to prevent the phototransistor from saturating.

The first transparency holder, the converging lens, and the phototransistor were all mounted on an optical bench. Alignment of the two transparencies was achieved by initially superposing them by eye followed by a more precise alignment by adjusting them vertically, horizontally, and rotationally until the transmitted intensity measured by the phototransistor was maximized.

§VI: 3.3 — Data Collection

The area of constant light intensity was limited, making it necessary to limit the transmission through the transparencies to an aperture stop of about 3.0×3.5 cm^2. The chosen magnification of the transparencies permitted good initial alignment, but the limited area through

which light was gathered was *not* large compared to the largest hole size (see Figure VI-2). For this reason, the displacement-dependent intensity measurements were performed over three different regions of the transparencies. Overlapping regions were avoided so that one area of the cross section was not weighted more than another when the results were averaged.

§VI: 4 — DATA AND ANALYSIS

The data for this section was gathered by Henry Schriemer.

Of the samples #18-22 , measurements were performed only on #20 due to time constraints. A log-log plot of the average transmitted intensity versus the displacement R is shown in Figure VI-3 , from which the three length scale regimes described by Equation (VI-13) can be identified. In the regime $R < \sim 0.8\mu m$, the approximate average radius of the glass beads, the dependence of the intensity on displacement is low. For $R \gg 5\ \mu m$, the intensity is seen to remain approximately constant and a line of zero slope can be drawn through the data, as is expected in the Euclidean regime of a percolating system (Equation (VI-13b)). However it can be seen that within the region $(\sim 0.8 < R < \sim 5)\ \mu m$, the data is reasonably described by a straight line of slope -0.58 ± 0.10 . The points chosen for the fitted region and the line best describing these points were judged by eye. The uncertainty of the slope arose mainly due to the uncertainty of the boundaries of the region to be fitted. From Equation (VI-13a) , the obtained value of the slope yields a value of the fractal dimension $D = 2.42 \pm 0.10$, in good agreement with the theoretical value of $D = 2.50$. The point that the fitted lines of the two regimes $R \gg 5\ \mu m$ and $(\sim 0.8 < R \sim 5)\ \mu m$ intersect is a good approximation of the cross-over point of the fractal and Euclidean regimes, and is found to be $\xi \sim 5\ \mu m$.

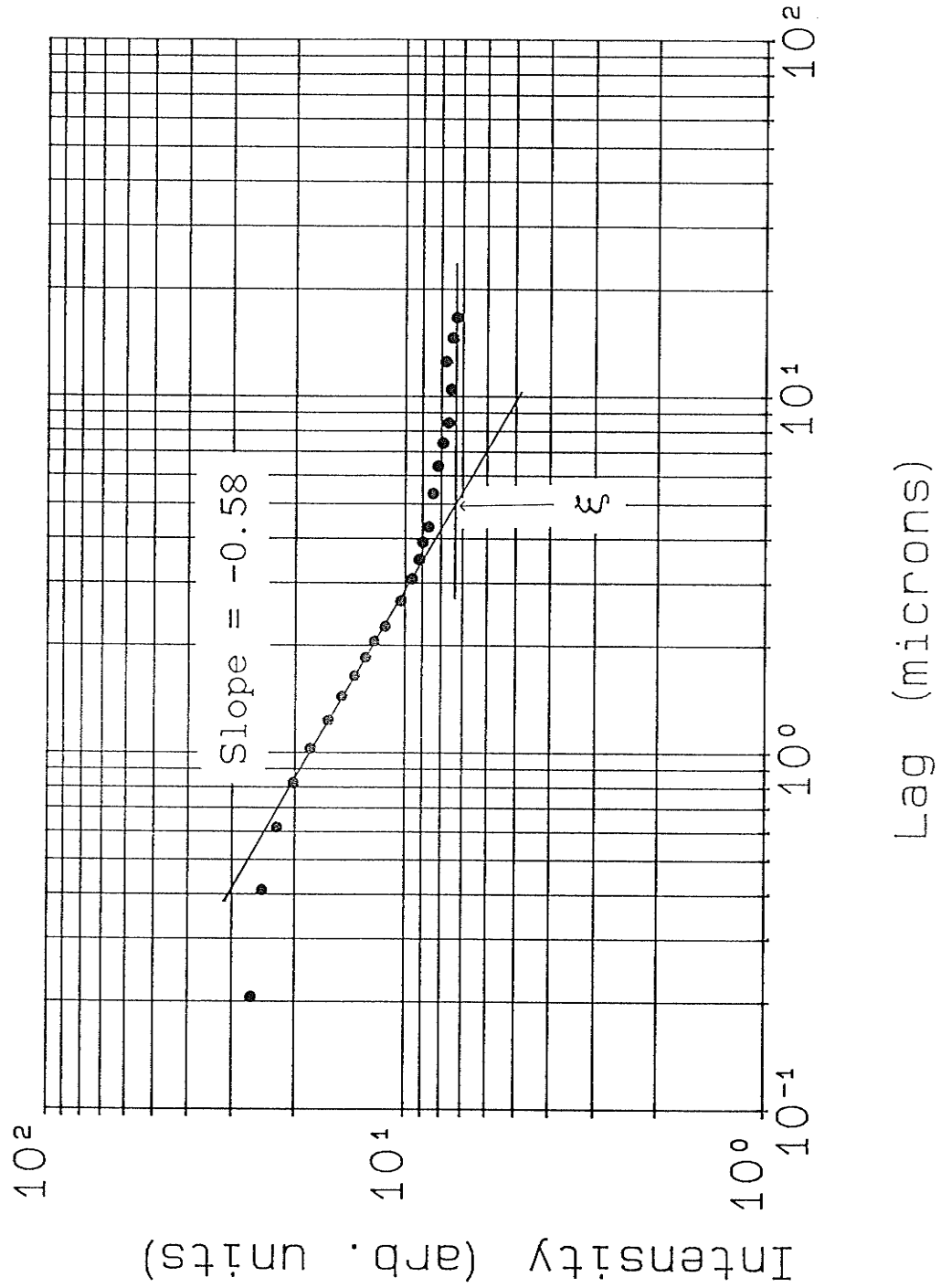

Figure VI-3: Logarithmic plot of the transmitted light intensity versus the lag of a transparency of a two-dimensional sample cross section with an identical copy. The correlation length $\xi \sim 5\ \mu m$ marks the boundary between fractal and Euclidean regimes. The value of the imbedding dimension d plus the slope yields the fractal dimension D : $3 - 0.58 = 2.42 \pm 0.10$.

Chapter VII: Conclusions

Ultrasonic velocity and attenuation measurements have been performed to study the vibrational properties of a structural percolation system made from glass microspheres. In an attempt to construct a physical realization of a three dimensional percolation system, 1 μm glass spheres were randomly positioned by mixing them with nickel powder of a similar grain size. After sintering the glass beads together, the nickel particles were removed through etching in acid to leave a porous glass network in which the positions of glass beads and voids were controlled as in percolation models. Samples with occupied volume fraction f ranging from 0.19 to 0.5 were prepared, although the present ultrasonic measurements were limited to the denser samples because of the large attenuations found in our frequency range for $f < 0.3$. The percolation threshold was estimated to be $0.187 + 0.008$ because upon removal of the nickel, one sample with $f = 0.180$ completely disintegrated whereas a sample with $f = 0.195$ did not.

Evidence that bulk properties of the samples can be well described by percolation theory was found from the dependence of sample density on occupied volume fraction. For the samples on which ultrasonic measurements were performed, the density was found to vary as $(f-f_c)^{0.44\pm0.03}$ in good agreement with the percolation theory exponent $\beta = 0.44$ for the infinite cluster above p_c. Note that for samples with occupied volume fractions close to threshold, one would not expect the measured density to correspond to that of the infinite cluster since the mass of the isolated clusters also contributes appreciably to the total mass of

the sample. However the samples that were used in the ultrasonic measurements all had occupied volume fractions sufficiently far above f_c that the contribution of isolated clusters to the total mass was negligible.

The structure of one of the samples was examined using scanning electron micrographs of a two dimensional cross section. Area autocorrelation measurements were performed with the micrographs to determine both the fractal dimension D and the correlation length ξ that sets the upper length scale for fractal properties. For this sample, the fractal dimension was measured to be $D = 2.42 \pm 0.10$ which is consistent with the value predicted for a percolating structure imbedded in three dimensions ($D = 2.5$). The correlation length was found to be $\xi \sim 5\ \mu m$, only five times the typical particle radius, indicating that for this sample which was quite far above the percolation threshold ($f-f_c = 0.17$) the fractal region is very small. A relatively low magnification micrograph of the two dimensional cross section also revealed that there are inhomogeneities on length scales much larger than the correlation length (up to $\sim 10\xi$), despite attempts to minimize them through careful packing of the sample before pressing.

Ultrasonic velocity measurements were performed to learn about the weak elasticity of the porous glass network. It was found that the softening of the velocity varies strongly with a decrease in the occupied volume fraction. The velocities of both the longitudinal and transverse modes followed a power law dependence on $f-f_c$, namely $\omega \propto (f-f_c)^{1.25\pm0.1}$. Measurement of this exponent allowed the calculation of the fracton dimension $\tilde{d} = 1.0 \pm 0.1$ and showed that the micro-

scopic elasticity is better described by the tensorial bond-bending model ($\tilde{d}_{b\text{-}b}$=0.89) than by the scalar Born model ($\tilde{d}=\frac{4}{3}$).

Measurements of the attenuation of ballistic sound waves enabled the frequency dependence of the elastic mean free path $\ell(\omega)$ to be determined. At low frequencies, the attenuation is low and $\ell(\omega)$ is very long compared to the wavelength. However at the highest measured frequencies, the attenuation is very large and $\ell(\omega)$ is less than a wavelength, suggesting that a propagating wave description is no longer valid and that a crossover to localized acoustic vibrations exists. However in this work, the Ioffe-Regel localization condition was not reached due to loss of a transmitted signal at high frequencies. It would be interesting to make measurements on very thin samples in order to search for crossover behaviour in the attenuation and velocity measurements.

The attenuation curves for different samples were found to scale reasonably with the correlation length ξ. The correlation lengths were not measured directly for all samples; a scaling length ℓ^* was instead extracted from each attenuation curve. The value of ℓ^* was chosen to be the mean free path at which $\ell(\omega)=\lambda(\omega)$; it was expected to be proportional to ξ. The attenuation curves scaled well with ℓ^* and produced a single curve, as expected if single-parameter scaling holds. One source of concern, however, is the fact that the scaling lengths extracted from the transverse attenuation curves were consistently shorter than those from the corresponding longitudinal curves. It is possible that the mechanism behind this discrepancy is an inelastic component of the attenuation, although it would be necessary

for this contribution to be greater for longitudinal waves and to scale with $f-f_c$ in the same way as the elastic component.

The frequency dependence of the attenuation was found to have a crossover point at the scaled frequency $\omega/\omega^* \cong 0.5$. For $\omega \lesssim 0.5\omega^*$, it is plausible that the scaled attenuation follows a frequency dependence of ω^4 , as expected from Raleigh scattering. For $\omega \gtrsim 0.5\omega^*$ (that is, $\lambda \lesssim 2\ell^*$), the best fit line is $\alpha(\omega) \propto \omega^{2.35\pm0.10}$. This weaker frequency dependence is probably due to inhomogeneities in the samples on length scales comparable with the ultrasonic wavelength for $\lambda/2\pi \lesssim 10\xi$. However it is difficult to verify this idea through a quantitative model for the measured frequency dependence in the absence of detailed information on the distribution of inhomogeneities in our samples. A more fruitful approach may be to reduce the inhomogeneities of the samples by the method of multiple grindings, as discussed in §III:2.4 . This would be advantageous because eliminating the $\omega^{2.35}$ behaviour would reduce the attenuation at the length scale of $\sim 10\xi$ and enable measurements to be performed on samples closer to f_c using our available frequency range. That is, scaling behaviour closer to the percolation threshold could be investigated.

APPENDIX A: ATTAINING ACTUAL ATTENUATION MEASUREMENTS FROM MISMATCHED TRANSDUCERS

As mentioned in §IV: 1.1b , some of the pairs of transducers do not have exactly the same frequency response. This means that for the same initial voltage applied, the signal output by one transducer is a different amplitude than the signal output by the other. To correct for this, the reflected and transmitted signals from a sample were measured with one transducer acting as the signal generator, then the same measurement was immediately repeated with the roles of the two transducers exchanged. The average of the two is the true value, as proven in the following discussion.

With reference to Figure A-1 , define the following variables:

V_o = initial voltage impinging upon generating transducer

V_R = voltage detected in reflected path

V_T = voltage detected in transmitted path

V' = voltage at the detector

G = gain of amplifier

α = attenuation coefficient of sample

x = sample thickness .

For transducers #i (i = 1,2),

β_i = bond and conversion efficiency factor .

At the sample boundaries #i (i = 1,2),

R_i = power reflection coefficient

T_i = power transmission coefficient .

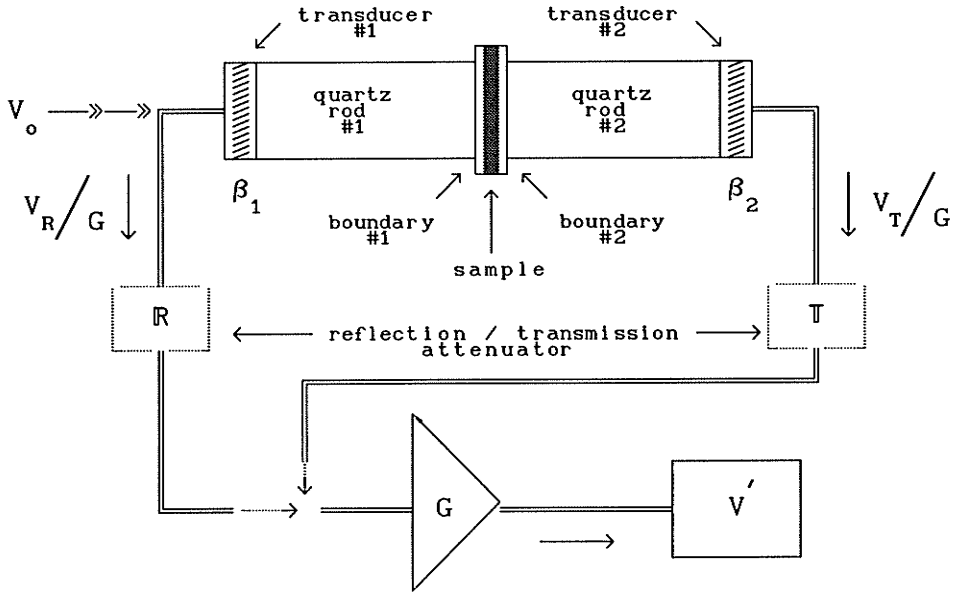

Figure A-1: Transmitted and reflected pulse paths

Following the path of the reflected and the transmitted pulses in Figure A-1 , we see that the detected voltages are

$$V_R = V_0 \beta_1 R_1^{1/2} \beta_1 G \qquad \text{(A-1)}$$

$$V_T = V_0 \beta_1 T_1^{1/2} \exp\{-\alpha x/2\} T_2^{1/2} \beta_2 G \ . \qquad \text{(A-2)}$$

The measured voltages from the transmitted and reflected paths were both adjusted to be equal to a set voltage V' using calibrated attenuators. That is, if $\mathbb{T}$ and $\mathbb{R}$ were the recorded values of the attenuators in decibels, then

$$\mathbb{T} = 20 \log\left(\frac{V_T}{V'}\right) \qquad \text{and} \qquad \mathbb{R} = 20 \log\left(\frac{V_R}{V'}\right) \tag{A-3}$$

so that

$$\mathbb{R} - \mathbb{T} = 20 \log\left(\frac{\beta_1}{\beta_2}\right) + 10 \log\left(\frac{R_1}{T_1 T_2}\right) + 4.34(\alpha x) \quad . \tag{A-4}$$

The voltages V_o and V', and the gain G are common to both the $\mathbb{R}$ and $\mathbb{T}$ term and cancel when subtracted. If the duties of the two transducers are reversed, it can be easily shown that

$$< \mathbb{R} - \mathbb{T} > = 10 \log(R_1 R_2) - 20 \log(T_1 T_2) + 4.34(\alpha x) \quad . \tag{A-5}$$

The first two terms represent the loss due to impedance mismatch (and bond loss) while the last term is the attenuation (in decibels) of the pulse amplitude due to all scattering and absorption mechanisms of the sample. The efficiencies of the transducers cancel when the average is calculated.

Appendix B: The Scanning Electron Microscope

A scanning electron microscope (SEM) was used to observe the samples at various stages of preparation. With a SEM, primary electrons are accelerated towards a sample under vacuum. The interaction of these electrons with the sample results in the emission of secondary electrons, as well as x-rays with energies that are characteristic of the element. The emitted secondary electrons are detected and processed to form an image of the sample; the x-rays detected by an energy dispersive spectrometer (EDS) are used to analyze the composition of a sample. Further details of this standard equipment can be found in reference texts (such as Goldstein [1981]). The purpose of this appendix is to note pertinent aspects and limitations of the SEM features which were used to study the samples.

§B: 1 — THE SEM AND THE EDAX SPECTROMETER

The SEM equipment that was used was an ISI-100B from International Scientific Instruments. The SEM was used to view cross sections of the samples in order to determine their homogeneity, to establish an acceptable degree of sintering, and to obtain micrographs of the samples at various stages of preparation.

Accompanying the SEM was an Energy Dispersive Analysis of X-rays (EDAX) spectrometer. The EDAX produces an energy spectrum from the characteristic x-rays from the samples. It was used to help differentiate nickel particles from glass particles when viewing a sample, to determine changes in composition of the glass, and to detect residual nickel in the samples after etching. Throughout Chapter III , analyses of spectra are listed. The values listed are not as accurate as stated by their uncertainties due to assumptions in the analysis program (EDAX 9100/60 version 2.3) that were *not* valid for the samples studied. These points will be discussed in the following subsections.

§B: 1.1 — Spectra Analysis and Assumptions

A standard technique to correct for bulk properties of a sample is the ZAF technique. In order to improve the quantitative analysis, the number of counts within the peaks are modified by factors which arise

due to influences of the atomic number (Z), the absorption of the x-rays by the constituents of the sample (A), and their fluorescence (F). The closer these multiplicative factors are to the value 1, the lesser the correction that is applied. The dominant factor in our case is the absorption coefficient.

For our samples, the penetration depth of a primary electron and the diameter of the resulting volume of interaction is ~1 μm ; it is from the interaction volume that the detected secondary electrons and x-rays originate. However, the x-ray analysis technique that is used is appro-priate for alloys: it assumes that the constituents of a sample are homogeneous within the interaction region. This is certainly not the case for a mixture of two materials that each have a grain size of ~2 μm .

The sample is assumed to be flat on the order of the penetration depth for analysis. Since the x-ray detector is at an angle to the sample surface, if the sample is not flat, some x-rays may pass through an outcrop of material before reaching the detector. This would tend to attenuate lower energy x-rays more than those of higher energy and it would therefore skew the proportion of sample constituents towards the emitter of the higher energy x-ray. The contribution of this factor is dependent upon the roughness of the sample surface and its angle to the detector. This factor varied from sample to sample and it may have been a cause of significant variation in the measured spectra.

§B: 1.2 — Mass Absorption Coefficients

The absorption factor A is calculated in the analysis program from the mass absorption coefficients (MACs). These coefficients give a measure of how much one material absorbs the x-rays emitted by another. The MACs for the constituents of a glass bead/nickel mixture are listed in Table B-1 from Goldstein [1981]. The net effect of these coefficients is that for an element, the larger the relative MAC , the larger the correction necessary. That is, a large MAC means that there is a high rate of absorption (a small absorption factor A) so that it is necessary to artificially add counts to a constituent which has its x-rays highly absorbed. This does not improve the statistical uncertainty, but it does increase the calculated proportion of the constituent. As seen in the table, nickel is a strong x-ray absorber for the constituents of the glass and strongest for sodium. The value of A for the absorption of sodium x-rays by nickel is on the order of 0.1 which means that the proportion of the sodium peak was adjusted on the order of 1000% !

§B: 1.3 — Incorrect Artificial Adjustments

From §B:1.1 , it is seen that the samples are not homogeneous such that both constituents are within the interacting volume of an impinging primary electron. However, from §B:1.2 it is seen that the analysis program multiplies the sodium contribution by a large adjustment factor

Table B-1

Mass Absorption Coefficients

	Emitter			
Absorber	Na	Si	Ca	Ni
Na	0	1654.1	265.9	37.2
Si	1332.5	327.9	530.6	75.2
Ca	4412.8	1086.0	139.4	193.7
Ni	12805.6	3151.6	404.4	58.9

to compensate for an absorption that in reality does not exist to a large extent. Thus it is expected that for the samples that contain nickel particles, the spectra listed will have a disproportionately large concentration of sodium (for example, Tables III-2 and 3) as an artifact of the analysis program.

§B: 2 — THE CONCENTRATION TABLES

The program could output the concentrations of the constituents of the samples in one of two ways. They could be listed in terms of their percentage of weight in the sample, or else the percentage weight numbers could be divided by the atomic weight of the elements to give the proportion of the number of atoms of each element in a volume. The latter was chosen because it made it slightly easier to include the mass to the undetected oxygen atoms when calculating the occupied volume fraction of each compound. The unnormalized occupied volume (not including air space) is given by

$$\text{occupied volume} \propto \frac{\text{Atomic \%} \times \text{mass/molecule}}{\text{bulk density}} \quad . \qquad \text{(B-1)}$$

The uncertainties that are listed in each table are statistical in nature and are dependent essentially upon the square root of the number of counts in each peak. The calculated uncertainty does *not* account for any systematic errors that arise from the ZAF coefficients which are incorporated in the calculation of the concentrations: these errors can be considerable as discussed in §B:1 . In addition, there may be a further systematic uncertainty in the calibration of the EDAX on the order of 2% . Therefore the analyses were useful only as a qualitative guide.

Appendix C: Reflection and Transmission Coefficients for Ultrasonic Waves in Attenuating Media

The standard problem of a wave train incident upon an interface of two media is very familiar. In this appendix, the boundary conditions imposed are specifically for acoustic waves, but generalized to include attenuating media. There are terms which evolve from this generalization that are not present in the conventional non-attenuating system, and affect both the phase and amplitude of the transmitted and reflected waves.

§C: 1 — PROPERTIES OF AN ATTENUATING MEDIUM

The displacements u_x associated with a longitudinal ultrasonic wave in an attenuating medium are

$$\begin{aligned} u_x &= A \exp[i(kx - \omega t)] \exp[-\alpha x] \\ &= A \exp[i(\tilde{K}x - \omega t)] \end{aligned} \qquad \text{(C-1)}$$

where α is the attenuation coefficient and $\tilde{K} = k + i\alpha$ is the complex wavevector. The attenuation causes both the elastic constants c and the impedances Z of the medium to become complex. The expressions for a non-attenuating medium are easily generalized by writing c and Z in terms of the wavevector $\tilde{K}$ (complex quantities are denoted by the tilde "~"):

$$c = \rho\left(\frac{\omega}{k}\right)^2 = \rho v^2$$

is analogously expressed as

$$\begin{aligned} \tilde{c} &= \rho\left(\frac{\omega}{\tilde{K}}\right)^2 = \rho\left(\frac{\omega}{(k + i\alpha)}\right)^2 = \rho\left(\frac{\omega}{k(1 + i\delta)}\right)^2 \\ &= \frac{c}{(1 + i\delta)^2} \end{aligned} \qquad \text{(C-2)}$$

and the analogous complex version of the impedance

$$Z = \rho\frac{\omega}{k} = \rho v$$

is expressed as

$$\tilde{Z} = \rho \frac{\omega}{\tilde{K}} = \rho \frac{\omega}{k + i\alpha} = \rho \frac{\omega}{k(1 + i\delta)}$$

$$= \frac{Z}{1 + i\delta} \qquad \text{(C-3)}$$

where $v = \omega/k$ is the phase velocity and we have defined $\delta = \alpha/k$. The particle velocity V_x, the strain ε_{xx}, and the stress σ_{xx} associated with the ultrasonic wave can be written in terms of these complex quantities:

$$V_x = \frac{\partial u_x}{\partial t} = -i\omega u_x \qquad \text{(C-4)}$$

$$\varepsilon_{xx} = \frac{\partial u_x}{\partial x} = i\tilde{K} u_x \qquad \text{(C-5)}$$

$$\sigma_{xx} = \tilde{c}\, \varepsilon_{xx} = i\omega \tilde{Z} u_x \,. \qquad \text{(C-6)}$$

With suitable modifications of the velocity and the elastic constant, the expressions for transverse waves is the same.

§C: 2 — REFLECTION AND TRANSMISSION AT A SINGLE INTERFACE BETWEEN TWO ATTENUATING MEDIA

Given a single interface between two attenuating media situated at x=0 (Figure C-1), consider an impinging longitudinal ultrasonic wave incident from the left.

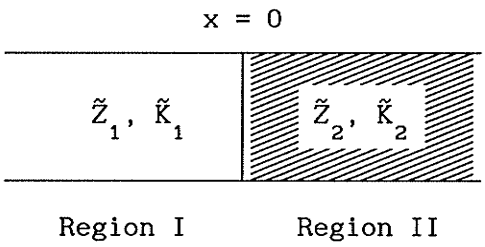

Figure C-1

The ultrasonic displacements u of the two regions are given by

$$u_I = A \exp\left[i(\tilde{K}_1 x - \omega t)\right] + B \exp\left[-i(\tilde{K}_1 x + \omega t)\right] \qquad \text{(C-7a)}$$

$$u_{II} = C \exp\left[i(\tilde{K}_2 x - \omega t)\right] \qquad \text{(C-7b)}$$

and the associated stresses $\sigma = \tilde{c}\,\frac{\partial u}{\partial x}$ in the two regions are

$$\sigma_I = i\omega\tilde{Z}_1\left\{A \exp\left[i(\tilde{K}_1 x - \omega t)\right] - B \exp\left[-i(\tilde{K}_1 x + \omega t)\right]\right\} \qquad \text{(C-8a)}$$

$$\sigma_{II} = i\omega\tilde{Z}_2\, C \exp\left[i(\tilde{K}_2 x - \omega t)\right] \quad . \qquad \text{(C-8b)}$$

As discussed by Auld [1973], the boundary conditions at x=0 require that the particle velocities and stresses be continuous across the interface. Equating the particle velocities in each region (Equations (C-4 and 7)) at x=0 gives the result

$$(A + B) = C \tag{C-9}$$

and equating the particle stresses in each region (Equations (C-6 and 8)) gives

$$(A - B)\tilde{Z}_1 = C\,\tilde{Z}_2 \,. \tag{C-10}$$

Using Equations (C-9 and 10) to solve for B/A and C/A produces

$$\frac{B}{A} = \frac{\tilde{Z}_1 - \tilde{Z}_2}{\tilde{Z}_1 + \tilde{Z}_2} \tag{C-11}$$

and

$$\frac{C}{A} = \frac{2\tilde{Z}_1}{\tilde{Z}_1 + \tilde{Z}_2} \,. \tag{C-12}$$

§C: 3 — REFLECTION AND TRANSMISSION COEFFICIENTS AT A SINGLE INTERFACE OF TWO ATTENUATING MEDIA

The reflection and transmission coefficients R and T are defined as the fraction of the incident energy flux that is reflected and transmitted across the boundary. For a longitudinal ultrasonic wave propagating in the x direction, the average power flow P_{av} is obtained from the acoustic Poynting vector P by

$$P_{av} = \mathrm{Re}(P) \qquad \text{(C-13)}$$

where the acoustic Poynting vector, as defined by Auld [1973], is

$$P = - \hat{\mathbf{x}} \frac{1}{2} V_x^* \sigma_{xx} . \qquad \text{(C-14)}$$

Note that P is complex even if there is no attenuation in the medium because of the use of complex representation for the displacements.

The following equations are developed for normal incident longitudinal waves but can be analogously be applied to normal incident shear waves. They are generalized versions of those discussed by Auld for non-attenuating media. We calculate the Poynting vector for the two media in order to calculate the coefficients. For region I of Figure C-1 , the acoustic Poynting vector is obtained using Equations (C-4, 7a, 8a, and 14):

$$P_I(x) = -\hat{\mathbf{x}}\frac{1}{2}V^*_{x,I}\,\sigma_{xx,I}$$

$$= -\hat{\mathbf{x}}\frac{1}{2}\left\{i\omega A^* \exp\left[-i(\tilde{K}_1^* x - \omega t)\right] + i\omega B^* \exp\left[i(\tilde{K}_1^* x + \omega t)\right]\right\} \times$$

$$i\omega\tilde{Z}_1\left\{A \exp\left[i(\tilde{K}_1 x - \omega t)\right] - B \exp\left[-i(\tilde{K}_1 x + \omega t)\right]\right\}$$

$$= \hat{\mathbf{x}}\frac{1}{2}\omega^2 \tilde{Z}_1 |A|^2\left\{\exp[-2\alpha_1 x] - \left|\frac{B}{A}\right|^2 \exp[2\alpha_1 x]\right.$$

$$\left. - \frac{B}{A}\exp[-2ik_1 x] + \left(\frac{B}{A}\right)^* \exp[2ik_1 x]\right\} . \qquad \text{(C-15)}$$

At x=0 , Equation (C-11) holds and substitution of it into Equation (C-15) yields

$$P_I(0) = \hat{\mathbf{x}}\frac{1}{2}\omega^2 \tilde{Z}_1 |A|^2\left\{1 - \left|\frac{\tilde{Z}_1 - \tilde{Z}_2}{\tilde{Z}_1 + \tilde{Z}_2}\right|^2 - 2\frac{\left(\tilde{Z}_1\tilde{Z}_2^* - \tilde{Z}_1^*\tilde{Z}_2\right)}{\left|\tilde{Z}_1 + \tilde{Z}_2\right|^2}\right\}$$

$$= \hat{\mathbf{x}}\,\omega^2 |A|^2 \frac{2\left|\tilde{Z}_1^*\right|^2 \tilde{Z}_2}{\left|\tilde{Z}_1 + \tilde{Z}_2\right|^2} . \qquad \text{(C-16)}$$

This can be compared to the acoustic Poynting vector for region II :

$$P_{II}(x) = -\hat{\mathbf{x}}\frac{1}{2}V^*_{x,II}\,\sigma_{xx,II}$$

$$= -\hat{\mathbf{x}}\frac{1}{2}\left\{i\omega C^* \exp\left[-i(\tilde{K}_2^* x - \omega t)\right]\right\}\left\{i\omega\tilde{Z}_2 C \exp\left[i(\tilde{K}_2 x - \omega t)\right]\right\}$$

$$= \hat{\mathbf{x}}\frac{1}{2}\omega^2 \tilde{Z}_2 |C|^2 \exp[-2\alpha_2 x] . \qquad \text{(C-17)}$$

At x=0 , Equation (C-12) holds and substitution into Equation (C-17) yields

$$P_{II}(0) = \hat{\mathbf{x}}\,\omega^2|A|^2\frac{2\left|\tilde{Z}_1^*\right|^2\tilde{Z}_2}{\left|\tilde{Z}_1+\tilde{Z}_2\right|^2} \qquad \text{(C-18)}$$

which is identical to Equation (C-16) for $P_I(0)$, confirming that energy is indeed conserved over the interface.

If the real part of Equation (C-15) is considered for the case when B=0 (no interface), the surviving term must be proportional to the incident energy flux:

$$P_{av,Inc} = \hat{\mathbf{x}}\,\frac{1}{2}\omega^2 X_1|A|^2 \qquad \text{(C-19)}$$

where X_1 is defined as

$$X_1 = \mathrm{Re}(\tilde{Z}_1) = \frac{Z_1}{1+\delta_1^2} \; . \qquad \text{(C-20)}$$

The remaining terms of Equation (C-15) at x=0 are then proportional to the reflected energy flux:

$$P_{av,R} = \hat{\mathbf{x}}\,\frac{1}{2}\omega^2\,|A|^2\mathrm{Re}\left\{\tilde{Z}_1\left|\frac{\tilde{Z}_1-\tilde{Z}_2}{\tilde{Z}_1+\tilde{Z}_2}\right|^2 + 2\tilde{Z}_1\frac{\left(\tilde{Z}_1\tilde{Z}_2^*-\tilde{Z}_1^*\tilde{Z}_2\right)}{\left|\tilde{Z}_1+\tilde{Z}_2\right|^2}\right\} . \qquad \text{(C-21)}$$

It is worth noting a few attributes of this reflection term. First of all, when $\delta_1 = 0$ (no attenuation in region I), $\tilde{Z}_1 = X_1$ is real and there is *no* contribution from the second term of Equation (C-21) since it is purely imaginary. When $\delta_1 \neq 0$, the second term represents the effect of interference between the incident and reflected waves in region I which arises from the position dependence of the amplitude of

both waves in the attenuating medium. Starting from the third and fourth terms in Equation (C-15), we can write the position dependence of the interference terms (I.T.) as

$$\text{I.T.} = \hat{\mathbf{x}}\,\omega^2|A|^2\,\frac{X_1\delta_1}{X_1^2(1+\delta_1^2) + X_2^2(1+\delta_2^2) + 2X_1X_2(1+\delta_1\delta_2)}$$

$$\times\left\{\sin(2k_1x)\left[X_1^2(1+\delta_1^2) - X_2^2(1+\delta_2^2)\right] + \cos(2k_1x)\left[2X_1X_2(\delta_1-\delta_2)\right]\right\} \qquad \text{(C-22)}$$

so that at $x=0$,

$$\text{I.T.} = \hat{\mathbf{x}}\,\omega^2|A|^2\,\delta_1\,\frac{2X_1^2X_2(\delta_1-\delta_2)}{X_1^2(1+\delta_1^2) + X_2^2(1+\delta_2^2) + 2X_1X_2(1+\delta_1\delta_2)} \quad . \qquad \text{(C-23)}$$

This shows the explicit dependence of the interference term on δ_1 and δ_2 . However, for short pulses, the interference term is zero outside the region of overlap so that the measured reflected power includes only the first term of Equation (C-21) :

$$P_{av,R} = \hat{\mathbf{x}}\,\frac{1}{2}\omega^2\,|A|^2X_1\left|\frac{\tilde{Z}_1 - \tilde{Z}_2}{\tilde{Z}_1 + \tilde{Z}_2}\right|^2 \qquad \text{(short pulse, no overlap).} \qquad \text{(C-24)}$$

The transmitted energy flux is obtained from Equation (C-18) and is proportional to

$$P_{av,T} = \hat{\mathbf{x}}\,\omega^2|A|^2\frac{2\left|\tilde{Z}_1\right|^2 X_2}{\left|\tilde{Z}_1 + \tilde{Z}_2\right|^2} \quad . \qquad \text{(C-25)}$$

Thus it is possible to obtain the transmission and reflection coefficients T and R :

$$T = \frac{P_{av,T}}{P_{av,Inc}}$$

$$= \frac{4\left|\tilde{Z}_1\right|^2}{\left|\tilde{Z}_1 + \tilde{Z}_2\right|^2} \frac{X_2}{X_1}$$

$$T = \frac{4X_1X_2(1+\delta_1^2)}{X_1^2(1+\delta_1^2) + X_2^2(1+\delta_2^2) + 2X_1X_2(1+\delta_1\delta_2)} \qquad \text{(C-26)}$$

and, using Equations (C-19 and 21),

$$R = \frac{P_{av,R}}{P_{av,Inc}}$$

$$= \left| \frac{\tilde{Z}_1 - \tilde{Z}_2}{\tilde{Z}_1 + \tilde{Z}_2} \right|^2 - \delta_1 \frac{4X_1X_2(\delta_1 - \delta_2)}{\left|\tilde{Z}_1 + \tilde{Z}_2\right|^2}$$

$$= \frac{X_1^2(1+\delta_1^2) + X_2^2(1+\delta_2^2) - 2X_1X_2(1+\delta_1\delta_2)}{X_1^2(1+\delta_1^2) + X_2^2(1+\delta_2^2) + 2X_1X_2(1+\delta_1\delta_2)} \quad \text{(short pulse term)}$$

$$- \delta_1 \frac{4X_1X_2(\delta_1 - \delta_2)}{X_1^2(1+\delta_1^2) + X_2^2(1+\delta_2^2) + 2X_1X_2(1+\delta_1\delta_2)} \quad \text{(interference term).} \qquad \text{(C-27)}$$

Note that when $\delta_1=0$, the interference term vanishes, and when both media have no attenuation, both the impedances are real and the conventional reflection and transmission coefficients are recovered.

§C: 4 — REFLECTION AND TRANSMISSION COEFFICIENTS FOR ULTRASONIC WAVES PROPAGATING THROUGH AN ATTENUATING SAMPLE SANDWICHED BETWEEN ANOTHER ATTENUATING MEDIUM

In this section, we derive the reflection and transmission coefficients for a normal plane ultrasonic wave propagating through a sample which is sandwiched between two ultrasonic delay rods having an acoustic impedance different than that of the sample (as schematically shown in Figure C-2). In our experiments, the ultrasonic pulse width is generally less than the ultrasonic transit time through the sample or delay rod so that the effects of multiple reflections can be neglected. The measured quantities of interest are then the ultrasonic intensity that is reflected at x=0 (and detected at transducer A) and the intensity that is transmitted through the interfaces at x=0 and x=L (and detected at transducer B).

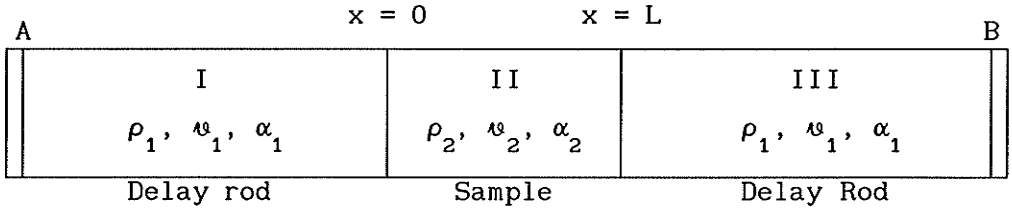

Figure C-2

§C: 4.1 — The Ultrasonic Wave Amplitudes

With the addition of a second interface at x=L , the transmitted wave of amplitude C from §C:2 may be considered incident to the second interface and will undergo partial reflection and transmission there. As previously discussed, multiple reflections are ignored for our purposes. The wave amplitudes of short pulses near the interface x=L in regions II and III are

$$u_{II} = C \exp\left[i(\tilde{K}_2 x - \omega t)\right] + D \exp\left[-i(\tilde{K}_2 x + \omega t)\right] \Big\} \qquad \text{(C-28a)}$$

$$u_{III} = F \exp\left[i(\tilde{K}_1 x - \omega t)\right] \quad . \qquad \text{(C-28b)}$$

Equating particle velocities and stresses at x=L yields the following relations:

$$\frac{D}{C} = \frac{\tilde{Z}_2 - \tilde{Z}_1}{\tilde{Z}_1 + \tilde{Z}_2} \exp\left[i2\tilde{K}_2 L\right] \qquad \text{(C-29)}$$

and

$$\frac{F}{C} = \frac{2\tilde{Z}_2}{\tilde{Z}_1 + \tilde{Z}_2} \exp\left[-i(\tilde{K}_2 - \tilde{K}_1)L\right] \quad . \qquad \text{(C-30)}$$

§C: 4.2 — Reflection and Transmission Coefficients at the Second Interface

Poynting's vector for region II of Figure C-2 can be calculated using Equations (C-4, 6, 14 and 28):

$$P_{II}(x) = -\hat{x}\frac{1}{2}V^{*}_{x,II}\,\sigma_{xx,II}$$

$$= -\hat{x}\frac{1}{2}\left\{i\omega C^{*}\exp\left[-i(\tilde{K}^{*}_{2}x - \omega t)\right] + i\omega D^{*}\exp\left[i(\tilde{K}^{*}_{2}x + \omega t)\right]\right\}$$

$$\times\, i\omega\tilde{Z}_{2}\left\{C^{*}\exp\left[-i(\tilde{K}_{2}x - \omega t)\right] + D^{*}\exp\left[i(\tilde{K}_{2}x + \omega t)\right]\right\}$$

$$= \hat{x}\frac{1}{2}\omega^{2}\tilde{Z}_{2}\left\{|C|^{2}\exp\left[-2\alpha_{2}x\right] - |D|^{2}\exp\left[2\alpha_{2}x\right]\right.$$

$$\left. - C^{*}D\exp\left[-2ik_{2}x\right] + CD^{*}\exp\left[2ik_{2}x\right]\right\} \qquad \text{(C-31)}$$

At x=L , Equations (C-29 and 31) can be combined to obtain

$$P_{II}(L) = \hat{x}\frac{1}{2}\omega^{2}|C|^{2}\exp\left[-2\alpha_{2}L\right]\tilde{Z}_{2}\left\{1 - \left|\frac{\tilde{Z}_{1} - \tilde{Z}_{2}}{\tilde{Z}_{1} + \tilde{Z}_{2}}\right|^{2} - 2\frac{\left(\tilde{Z}_{1}\tilde{Z}^{*}_{2} - \tilde{Z}^{*}_{1}\tilde{Z}_{2}\right)}{\left|\tilde{Z}_{1} + \tilde{Z}_{2}\right|^{2}}\right\}$$

$$= \hat{x}\,\omega^{2}|C|^{2}\exp\left[-2\alpha_{2}L\right]\frac{2\,\tilde{Z}_{1}\left|\tilde{Z}_{2}\right|^{2}}{\left|\tilde{Z}_{1} + \tilde{Z}_{2}\right|^{2}} \qquad \text{(C-32)}$$

In a similar manner, Poynting's vector for region III can be calculated:

$$P_{III}(x) = -\hat{x}\frac{1}{2}V^{*}_{x,III}\,\sigma_{xx,III}$$

$$= -\hat{x}\frac{1}{2}\left\{i\omega F^{*}\exp\left[-i(\tilde{K}^{*}_{1}x - \omega t)\right]\right\}\left\{i\omega\tilde{Z}_{1}F\exp\left[i(\tilde{K}_{1}x - \omega t)\right]\right\}$$

$$= \hat{x}\frac{1}{2}\omega^{2}\tilde{Z}_{1}|F|^{2}\exp\left[-2\alpha_{1}x\right] \qquad \text{(C-33)}$$

At x=L we can substitute Equation (C-30) into Equation (C-33):

$$P_{III}(L) = \hat{\mathbf{x}}\,\omega^2|C|^2\exp\left[-2\alpha_2 L\right]\frac{2\tilde{Z}_1\left|\tilde{Z}_2\right|^2}{\left|\tilde{Z}_1+\tilde{Z}_2\right|^2} \qquad \text{(C-34)}$$

which is identical to $P_{II}(L)$ from Equation (C-32), confirming once again that energy is conserved over a boundary. By setting D=0 in Equation (C-31), it can be seen that at the second boundary, the incident energy flux is proportional to

$$P^{(2)}_{av,Inc} = \hat{\mathbf{x}}\,\frac{1}{2}\omega^2 X_2|C|^2\exp\left[-2\alpha_2 L\right] \qquad \text{(C-35)}$$

and in a fashion similar to Equation (C-27), the reflected energy flux at the second boundary can be found to be proportional to

$$P^{(2)}_{av,R} = \hat{\mathbf{x}}\,\frac{1}{2}\omega^2 X_2\exp\left[-2\alpha_2 L\right]\left\{\left|\frac{\tilde{Z}_1-\tilde{Z}_2}{\tilde{Z}_1+\tilde{Z}_2}\right|^2 + \delta_2\frac{4X_1X_2(\delta_1-\delta_2)}{\left|\tilde{Z}_1+\tilde{Z}_2\right|^2}\right\} \qquad \text{(C-36)}$$

where the first term is the short pulse, no overlap term and the second term is the interference term which arises near the boundary. The transmitted energy flux at the second boundary is proportional to

$$P^{(2)}_{av,T} = \hat{\mathbf{x}}\,\omega^2|C|^2\frac{2\left|\tilde{Z}_2^*\right|^2 X_1}{\left|\tilde{Z}_1+\tilde{Z}_2\right|^2}\exp\left[-2\alpha_2 L\right] \quad . \qquad \text{(C-37)}$$

Therefore from Equations (C-35, 36 and 37), it is possible to obtain the reflection and transmission coefficients through the second interface:

$$R^{(2)} = \frac{P_{av,R}}{P_{av,Inc}}$$

$$= \left| \frac{\tilde{Z}_1 - \tilde{Z}_2}{\tilde{Z}_1 + \tilde{Z}_2} \right|^2 + \delta_2 \frac{4X_1 X_2 (\delta_1 - \delta_2)}{\left| \tilde{Z}_1 + \tilde{Z}_2 \right|^2} \qquad \text{(C-38)}$$

and

$$T^{(2)} = \frac{P_{av,T}}{P_{av,Inc}}$$

$$= \frac{4\left|\tilde{Z}_2\right|^2}{\left|\tilde{Z}_1 + \tilde{Z}_2\right|^2} \frac{X_1}{X_2} \quad . \qquad \text{(C-39)}$$

§C: 4.3 — The Transmission Coefficient Through Both Interfaces

The results from the the previous sections can be used to calculate the transmission coefficient of a wave incident from the left of the sample and passing through the two boundaries. For this case, Equation (C-19) is proportional to the incident energy flux, Equation (C-27) is proportional to the reflected energy flux, while Equation (C-34) is proportional to the final transmitted energy flux. From Equations (C-12 and 30) ,

$$\frac{F}{A} = \frac{4\tilde{Z}_1 \tilde{Z}_2}{\left(\tilde{Z}_1 + \tilde{Z}_2\right)^2} \exp\left[-i(\tilde{K}_2 - \tilde{K}_1)L\right] \qquad \text{(C-40)}$$

which means that

$$|F|^2 = 16|A|^2 \frac{\left|\tilde{Z}_1\tilde{Z}_2\right|^2}{\left|\tilde{Z}_1 + \tilde{Z}_2\right|^4} \exp\left[-2(\alpha_2-\alpha_1)L\right] \quad . \tag{C-41}$$

Thus Equations (C-19, 33 and 41) can be combined to produce the transmission coefficient through both interfaces:

$$T = \frac{P_{T,III}}{P_{Inc,I}}$$

$$= 16 \frac{\left|\tilde{Z}_1\tilde{Z}_2\right|^2}{\left|\tilde{Z}_1 + \tilde{Z}_2\right|^4} \exp\left[-2\alpha_2 L\right] \quad . \tag{C-42}$$

For the case when $\delta_1 \cong 0$,

$$T = \frac{16z^2(1+\delta^2)}{\left[z^2 + 2z + (1+\delta^2)\right]^2} \exp\left[-2\alpha L\right] \tag{C-43}$$

where we have defined $\delta_2 = \delta$, $\alpha_2 = \alpha$ and $z = Z_2/Z_1$.

The reflection coefficient at the first interface remains unchanged from the initial result of Equation (C-27) because multiple reflections have not been considered. When $\delta_1 \cong 0$, the interference term vanishes leaving

$$R = \frac{(1 - z)^2 + \delta^2}{(1 + z)^2 + \delta^2} \quad . \tag{C-44}$$

§C: 5 — Phase Shifts of the Reflected and Transmitted Waves Caused by Attenuation

For a short pulse incident on the sample, consider the phase of the reflected wave with respect to the incident wave. Assume that the first medium has $\delta_1 \cong 0$ so that, as in the previous section, $\tilde{Z}_1 = Z_1$, $z = Z_2/Z_1$ and $\delta = \delta_2$. From Equation (C-11), the reflected wave then has the form

$$\frac{B}{A} = \frac{1 - z/(1+i\delta)}{1 + z/(1+i\delta)}$$

$$= \frac{1 - z + i\delta}{1 + z + i\delta}$$

$$= \frac{1-z^2+\delta^2+ i2\delta z}{(1+z)^2 + \delta^2} \qquad \text{(C-45)}$$

so that the phase of the reflected wave with respect to the incident wave is

$$\theta_R = \arctan\left\{ \frac{2\delta z}{1-z^2+\delta^2} \right\} . \qquad \text{(C-46)}$$

Now consider the transmitted wave under the same conditions and make the appropriate substitutions into Equation (C-40) :

$$\frac{F}{A} = \frac{4z/(1+i\delta)}{\left[1 + z/(1+i\delta)\right]^2} \exp\left[i(k_2 - k_1)L\right] \exp\left[-\alpha L\right] . \qquad \text{(C-47)}$$

At the position x=L , the phase change contributed by the first exponential factor is caused by the difference of acoustic velocity in

the delay rods and the sample. This factor would occur even if the sample was non-attenuating. The second exponential does not cause a phase change; it simply reduces the amplitude of the propagating wave. It is the phase of the remaining factor which is of interest, and can be calculated from the following:

$$\frac{F'}{A} = \frac{4z/(1+i\delta)}{\left[1 + z/(1+i\delta)\right]^2}$$

$$= \frac{4z(1+i\delta)}{\left[1 + z + i\delta\right]^2}$$

$$= \frac{4z}{\left[(1+z)^2 + \delta^2\right]^2}\left\{(1+z)^2 + \delta^2(2z+1) + i\delta(z^2-1-\delta^2)\right\} . \qquad \text{(C-48)}$$

The phase change of the transmitted signal induced by the attenuation of the medium is therefore

$$\theta_T = \arctan\left\{\frac{\delta(z^2-1-\delta^2)}{(1+z)^2 + \delta^2(2z+1)}\right\} . \qquad \text{(C-49)}$$

Note that the phases of both the reflected and transmitted signals are zero when the attenuation δ is zero.

Figure C-3 shows the dependence of the reflected and transmitted wave phase shifts upon the the attenuation level δ, using the transverse impedance of quartz as Z_1 and that of sample #20 as Z_2. It is valid to assume $\delta_1 \cong 0$ since the attenuation for fused quartz is less than 0.010 dB/m/MHz [Weast, 1989]. Note that the phase shift of the reflected wave is an order of magnitude less than that of the transmitted wave.

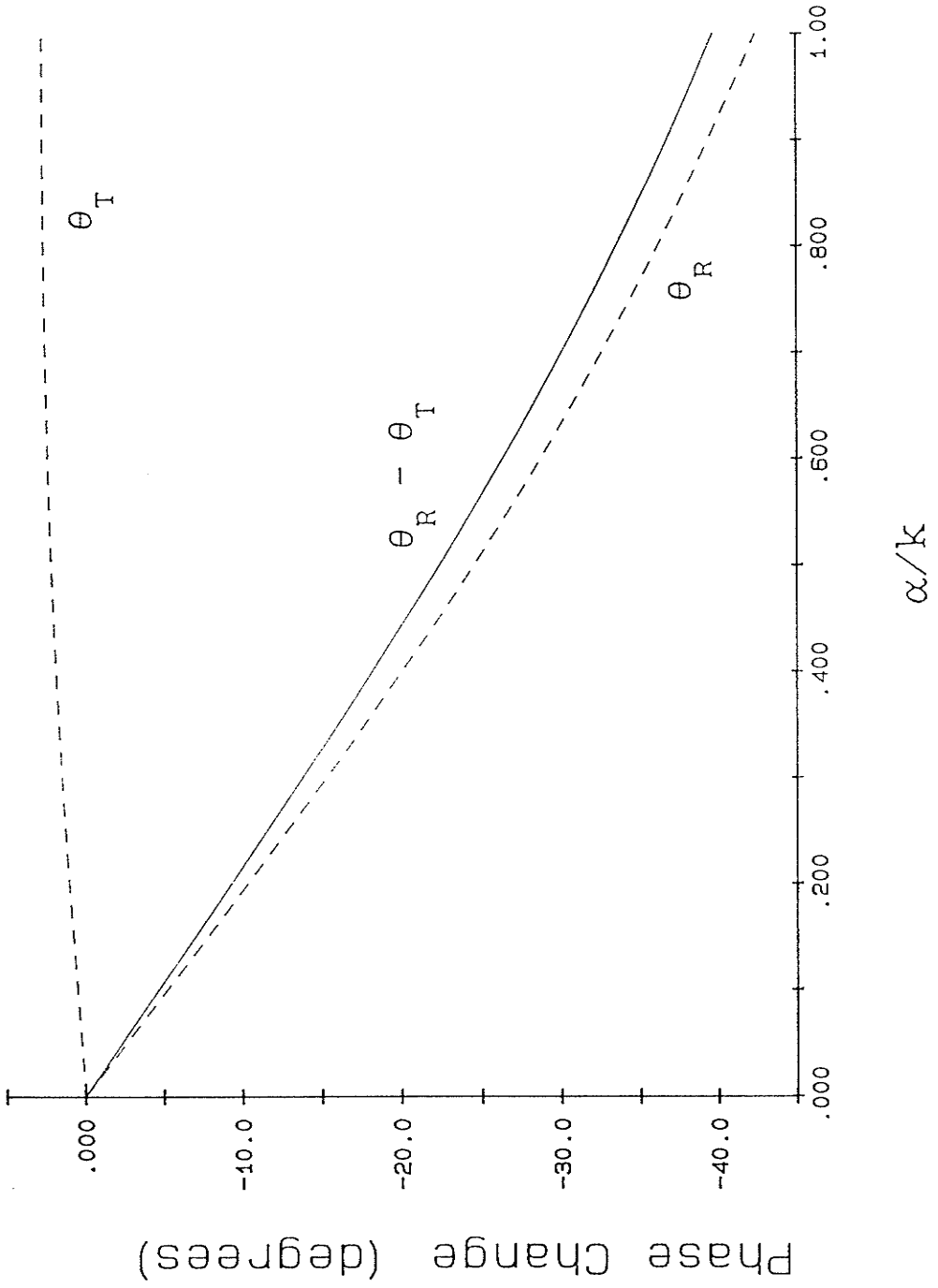

Figure C-3: A typical dependence of the reflected (θ_R) and transmitted (θ_T) wave phase shifts upon the the attenuation level $\delta_2 = \alpha/k$ is shown in this figure. The transverse impedance of quartz was used as Z_1 and that of sample #20 was used as Z_2. The attenuation of the first medium was set to zero.

For each sample, the time shift $\{\theta_R - \theta_T\}/\{360^\circ \times \text{freq}\}$ was calculated for both the highest and lowest recorded frequencies, where θ_R and θ_T are the phase shifts of the reflected and transmitted pulses respectively. In order to obtain a first order approximation of the effect of the phase changes on the transit time extrapolations, a line was first fit to the uncorrected highest and lowest frequency points of each sample, and then compared to a line fit to the corrected values. The difference of the zero-period extrapolations for each sample is a reasonable approximation of the effect of the attenuation on the delay data since the frequency dependence of the attenuation is greater than linear so that the time shifts increase monotonically with frequency for each sample. Note that when comparing the maximum phase shifts between samples, a larger value of δ corresponds to a larger phase shift but does not necessarily correspond to a larger time delay since the time shift is also inversely proportional to the frequency. The positive sign of the net phase shifts $\theta_R - \theta_T$ means that the corresponding time shift corrections must be subtracted from the measured values. The correction factors of the measured time delay for longitudinal and transverse waves propagating through samples #19-22 are listed in Table C-1 . The magnitude of the corrections is small, usually on the order of the uncertainty of each time delay measurement.

Table C-1a

Phase Shift Due to the δ Factor of the Samples

Longitudinal

#	$\frac{Z_2}{Z_1}$	v_L (m/s)	$\omega/2\pi$ (MHz)	α (dB/cm)	δ	θ_R (deg)	θ_T (deg)	Time Shift (ns)	Zero T Shift (ns)
19	0.0289	524	4.06	771	0.365	1.1	-19.0	13.7	26.1
			3.47	468	0.259	0.9	-13.8	11.6	
20	0.0444	730	6.11	613	0.268	1.3	-13.8	6.9	8.8
			3.41	148	0.116	0.6	-12.6	5.4	
21	0.0817	1144	5.92	145	0.102	1.0	-5.0	2.8	4.8
			3.39	21.4	0.026	0.3	-1.3	1.3	
22	0.1206	1500	5.49	27.2	0.027	0.4	-1.2	0.8	1.0
			3.83	11.8	0.017	0.2	-0.8	0.7	

Table C-1b

Phase Shift Due to the δ Factor of the Samples

Transverse

#	$\frac{Z_2}{Z_1}$	v_L (m/s)	$\omega/2\pi$ (MHz)	α (dB/cm)	δ	θ_R (deg)	θ_T (deg)	Time Shift (ns)	Zero T Shift (ns)
19	0.0245	280	2.88	722	0.326	0.7	-13.8	13.9	19.5
			1.16	46	0.051	0.1	-2.2	5.6	
20	0.0470	490	6.79	915	0.306	1.2	-12.4	5.6	6.5
			1.16	6	0.012	0.1	-1.8	1.3	
21	0.0928	819	10.72	735	0.261	2.1	-9.7	3.1	3.5
			1.16	~0	~0	0	0	0	
22	0.1349	1070	14.77	489	0.164	2.0	-5.7	1.4	1.9
			4.87	16	0.016	0.2	-0.6	0.4	

Appendix D: Time Delay Data and Extrapolations

The time delay of the transmitted wave with respect to the reflected wave was measured, and the method of data analysis (see §V:2.1) removed any ambiguity of the time delay via extrapolation to zero period. Graphs of the raw data and tables of the extrapolations from fitted lines are presented in this appendix. After a set of delay data was collected for a sample, usually a second set was immediately gathered with the roles of the two transducers reversed. This allowed the extrapolations of the two orientations to be averaged to account for any difference in path time delay of the two transducers and delay rods. The different orientations are referred as "#1 Generating" and "#2 Generating" in this appendix, to indicate which transducer generated the incident pulse (and detected the reflected signal), and the corresponding time delays are denoted as Δt_1 and Δt_2. When the average of the time delays $\langle \Delta t \rangle$ from the two orientations is found, their time difference $\Delta t_2 - \Delta t_1$ does not contribute to the statistical uncertainty of the average. The value of $\Delta t_2 - \Delta t_1$ is expected to be constant for a pair of transducers so that in the case of samples for which delay data were not collected in one of the orientations, the value of $\Delta t_2 - \Delta t_1$ (measured from other samples) could be used to calculate the actual delay.

A straight line was fit to the set of time delays that were measured when the transmitted pulse was properly overlapped with respect to the reflected pulse, and the same procedure was done for those time

delays which were offset by N periods. The zero-period y-intercept values were calculated for each line and it can be seen from the tables in this appendix that there is generally a small systematic increase of the values with increase of N , as discussed in §V:2.1 . The value and uncertainty of the actual transit time through the sample was taken as the zero-period delay extrapolated from the N=0 line, but the y-intercepts of the other lines were useful to ensure there was no unexplained systematic error associated with the data.

§D: 1 — LONGITUDINAL DATA

For the longitudinal measurements using the polymer transducers, it was found that the range of frequencies for which the most reliable measurements were obtained corresponds to periods between 0.17 and 0.30 μs . For measurements at larger periods (for example, see Figures D-1b and 2b), the delay time shows deviations from a linear dependence on period. This has been attributed to inaccuracy of the period measurement due to either pulse shape distortion or the non-linear response of the polymer transducers at their band edge. The greatest period for which reliable delay measurements can be made is dependent upon the transducer characteristics, but from data of Figure D-1b it was judged that the upper limit was $T = 0.30\ \mu s$ for the polymer transducers.

For the delay data at high frequencies, there is also a deviation from a straight line that is especially apparent for sample #21 (Figure D-2b). One cause of distortion of the transmitted signal was that spurious signals could become relatively significant when the measured signal was weak (see §IV:1.4). The spurious signal was eliminated for all transverse measurements, but the problem had not been identified until after the longitudinal data had been gathered for samples #20 and 21 . Sample #20 had been dismounted from the delay rods and therefore nothing could be done to salvage the higher frequency data ($T < 0.17\ \mu s$ of Figure D-3), but sample #21 was still mounted; a small correction factor was measured and subtracted from the gathered delay data of sample #21 , the final results of which are found in Figure D-2 .

However, the delay data of this figure is still found to deviate from a linear period dependence at ~0.17 μs . Some possible sources of delay distortion could be interference effects due to scattering in the porous samples, non-parallelism of the transducers, or scattering arising from long scale sample inhomogeneities. All these cancellation effects should become greater at higher frequencies, suggesting that the low frequency data ($T \geq 0.17$ μs) is more reliable.

The spurious signal had been eliminated for the delay measurements of sample #22 , but in Figure D-1b it can be seen that the data tends to curve upward with increase of frequency. This deviation is inconsistent, however, with the delay measurements of the other orientation of the same sample (Figure D-1a): it remains quite linear even to high frequencies. This implies that the curvature of Figure D-1b is caused not by some property of the sample, but that perhaps the bond of one of the sample faces was inferior and caused the peculiar frequency dependence.

Of all the samples, it is sample #21 (Figure D-2b) which has the most limited period range over which the longitudinal delay data does not significantly deviate from a linear fit ($0.17 \leq T \leq 0.30$ μs). In order to compare delay results extrapolated from a consistent period range, a linear least-squares fit was performed on the longitudinal data of each set within the same period range. In addition, if the period range of a set of data extended lower than this limit, the data was also analyzed over all points $T \leq 0.30$ μs and compared to the results obtained from over the limited range ($0.17 \leq T \leq 0.30$ μs).

The path delay difference $\langle \Delta t \rangle_2 - \langle \Delta t \rangle_1$ of the polymer transducers was calculated from extrapolations of lines fit to the delay data

over the period range $0.17 < T < 0.30\ \mu s$ and are summarized in Table D-1 .

Note that each of the measured longitudinal delays was corrected by the phase delay caused by the attenuation of the samples, the values of which are calculated in Appendix C .

Table D-1

Path Delay Difference of Polymer Transducers

for $0.17 < T < 0.30\ \mu s$

#	$\langle \Delta t \rangle_2 - \langle \Delta t \rangle_1$ (μs)
22	0.046 ± 0.015
21	0.060 ± 0.007
20	0.075 ± 0.005
average:	0.06 ± 0.01

§D: 1.1 — Sample #22

The measured delay time as a function of period for sample #22 is shown in Figure D-1 , and the zero-period extrapolations of a linear least-squares fit to each set of data is given in Table D-2 . The two different trials of one orientation (Table D-2a) were performed with the

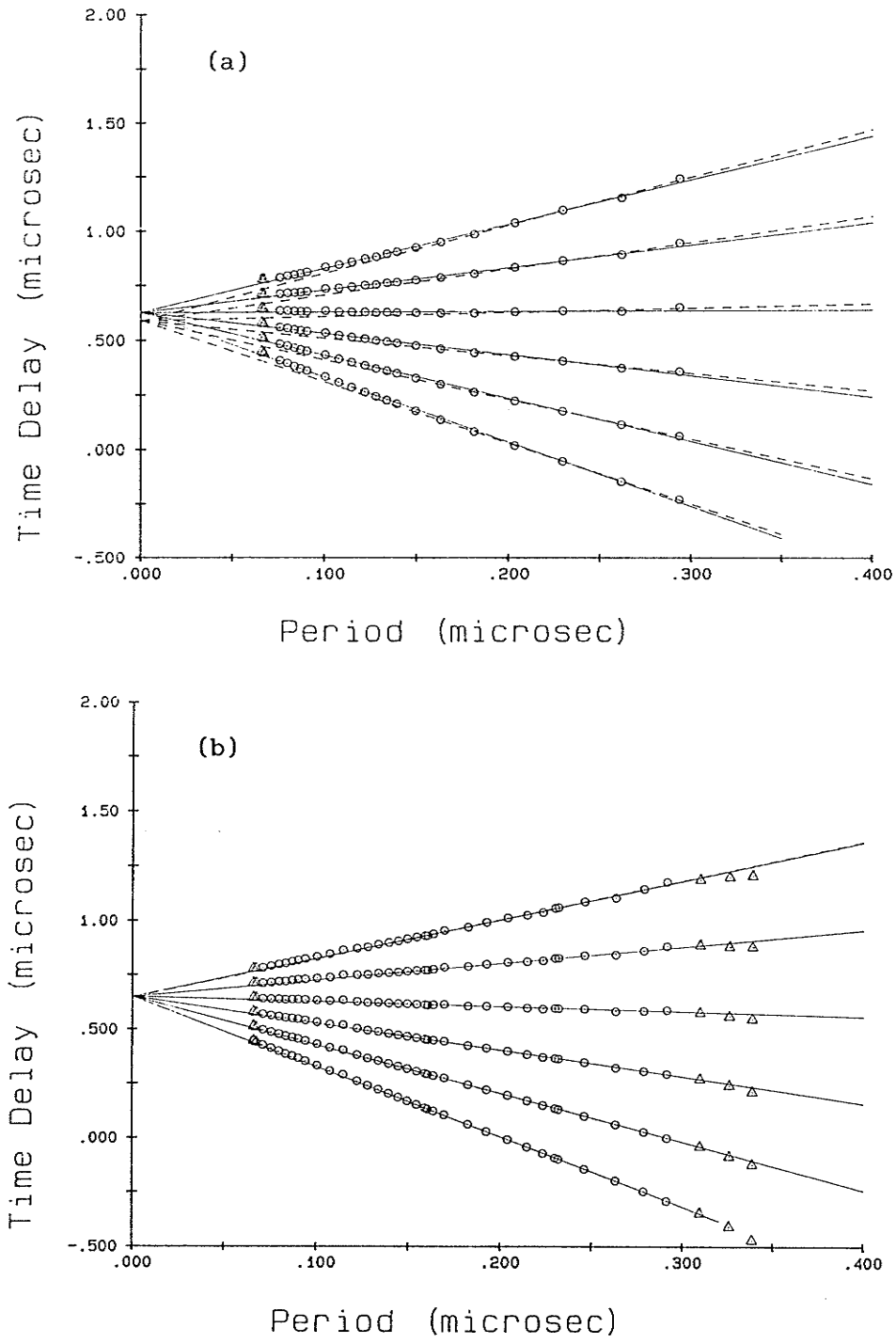

Figure D-1: Longitudinal delay measurements versus period for sample #22 , with polymer transducer **(a)** #1 (trial #2) and **(b)** #2 as the generator. Data (⊙) was fit over range $T < 0.30\ \mu s$ (——) and $0.17 < T < 0.30\ \mu s$ (----). The most horizontal line corresponds to the zero-period offset. The points (Δ) were not included in the line fits because their delay uncertainties were much larger than the other points.

Table D-2a

Sample #22 Longitudinal

#1 Transducer Generating

	Delay (μs)			
Range Fit:	T < 0.30 μs		0.17 < T < 0.30 μs	
N	Trial #1	Trial #2	Trial #1	Trial #2
+3	0.619 ± 0.003	——	0.584 ± 0.010	——
+2	0.620 ± 0.003	0.627 ± 0.004	0.584 ± 0.009	0.587 ± 0.020
+1	0.621 ± 0.003	0.627 ± 0.004	0.589 ± 0.007	0.588 ± 0.017
0	**0.621 ± 0.002**	**0.628 ± 0.003**	**0.591 ± 0.006**	**0.590 ± 0.013**
-1	0.621 ± 0.002	0.628 ± 0.003	0.592 ± 0.005	0.591 ± 0.010
-2	0.622 ± 0.002	0.628 ± 0.003	0.597 ± 0.004	0.592 ± 0.007
-3	0.622 ± 0.002	0.627 ± 0.003	0.596 ± 0.004	0.589 ± 0.008
Average:	**(0.625 ± 0.006)** μs		**(0.590 ± 0.013)** μs	

Table D-2b

Sample #22 Longitudinal

#2 Transducer Generating

N	T < 0.30	0.17 <T< 0.30
+4	0.65 ± 0.01	——
+3	0.65 ± 0.01	——
+2	0.65 ± 0.01	0.648 ± 0.011
+1	0.65 ± 0.01	0.652 ± 0.009
0	**0.65 ± 0.01**	**0.654 ± 0.007**
-1	0.65 ± 0.01	0.655 ± 0.004
-2	0.65 ± 0.01	0.658 ± 0.002
-3	0.65 ± 0.01	0.656 ± 0.003
-4	0.65 ± 0.01	0.661 ± 0.005

bond and delay rod separation unchanged, but the measurements were performed about one week apart. The reason for the measured delay discrepancy was not determined; therefore the average of the delays was used with an uncertainty sufficiently large to encompass the range of the two measured values.

It should also be noted that the two different period ranges over which a line was fit extrapolate to different y-intercepts. It can be seen that the delay data of sample #22 for one orientation (Figure D-1a) has a curvature which bends upward with decreasing period so that the resulting difference of delay extrapolation is not unreasonable. As previously discussed in this appendix, this curvature may be caused by an inferior bond on one face of the sample.

The path delay difference for sample #22 is found to be

$$\langle \Delta t \rangle_2 - \langle \Delta t \rangle_1 = (0.025 \pm 0.012)\ \mu s \qquad \text{for} \quad T < 0.30\ \mu s$$

$$\langle \Delta t \rangle_2 - \langle \Delta t \rangle_1 = (0.046 \pm 0.015)\ \mu s \qquad \text{for} \quad 0.17 < T < 0.30\ \mu s.$$

It can be seen (when compared to Table D-1) that the path delay difference values are most consistent when the same period range is used. This suggests that comparison of the extrapolated time delays may be most valid if the same period ranges are used for the line fits. The average value of the extrapolated time delay as obtained from the data fit in the period range $0.17 < T < 0.30\ \mu s$ is $\langle \Delta t \rangle_L^{22} = 0.622 \pm 0.007$ microseconds, but there is an additional delay correction of $-0.001\ \mu s$ due to the attenuation of the material which results in a final value of

$$\boxed{\langle \Delta t \rangle_L^{22} = (0.621 \pm 0.007)\ \mu s}\ .$$

§D: 1.2 — Sample #21

As described previously, the delay curves of sample #21 (Figure D-2) have a definite deviation from a straight line for $T < 0.17\ \mu s$ so that the y-intercepts of the lines fit to the delay data (Table D-3) are dependent upon the period range used. It is believed the higher period data is more reliable than the lower period delays; therefore the time delay through the sample is taken to be $(0.855 \pm 0.004)\ \mu s$, modified by the the delay correction due to phase changes induced by the attenuating medium. When the calculated correction factor of $-0.005\ \mu s$ is included, the result is

$$\boxed{\langle \Delta t \rangle_L^{21} = (0.850 \pm 0.004)\ \mu s} \ .$$

§D: 1.3 — Sample #20

The data for this sample is found in Figure D-3 and the zero-period extrapolations are found in Table D-4 . When the attenuation correction factor of $-0.009\ \mu s$ is included, the resultant delay of the data of Figure D-3 is

$$\boxed{\langle \Delta t \rangle_L^{20} = (1.205 \pm 0.003)\ \mu s} \ .$$

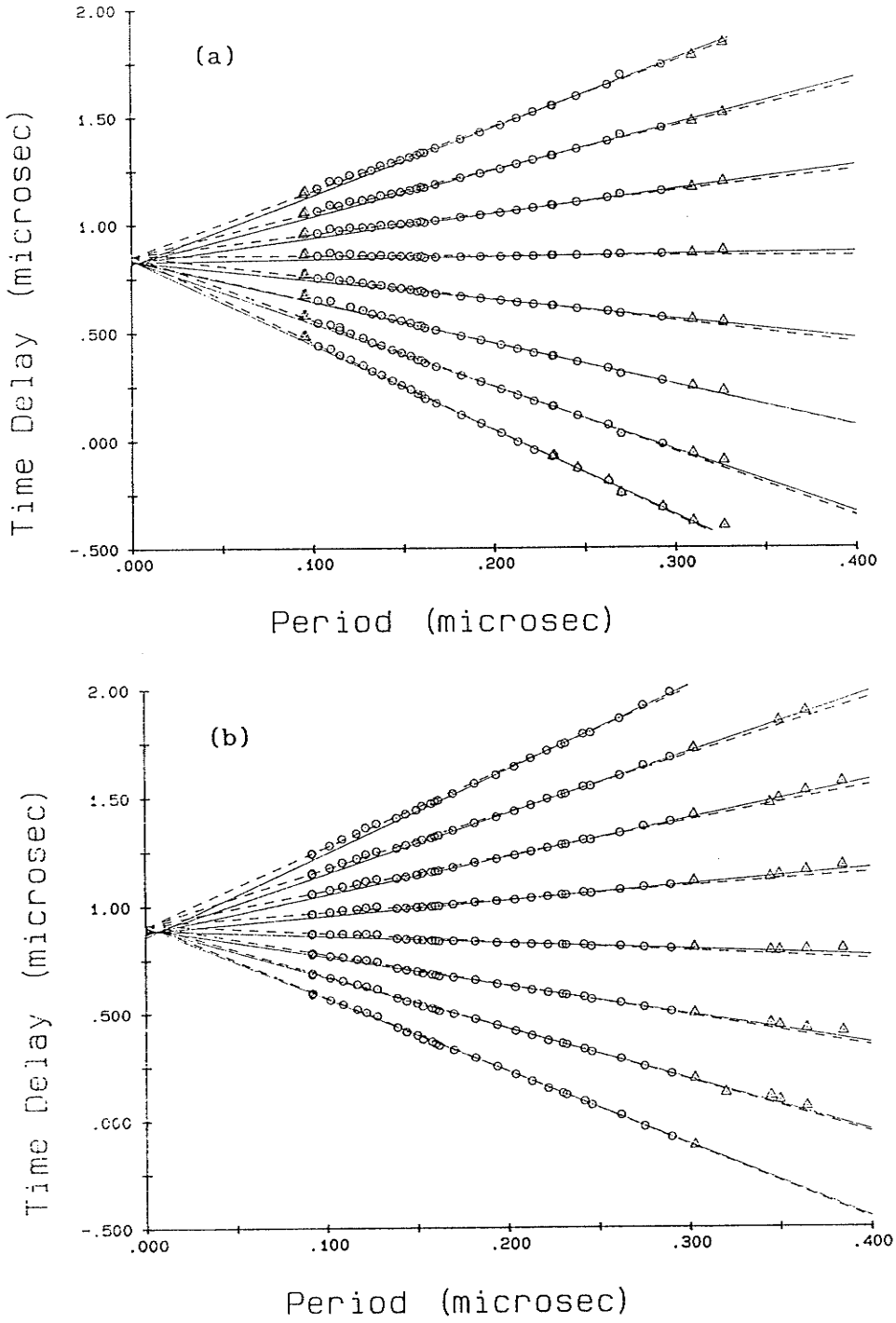

Figure D-2: Longitudinal delay measurements versus period for sample #21 , with polymer transducer **(a)** #1 and **(b)** #2 as the generator. Data (⊙) was fit over the ranges $T < 0.30$ μs (——) and $0.17 < T < 0.30$ μs (----). The most horizontal line corresponds to the N=0 offset. The points (Δ) were not included in the line fits because either their delay or period uncertainties were much larger than the other points.

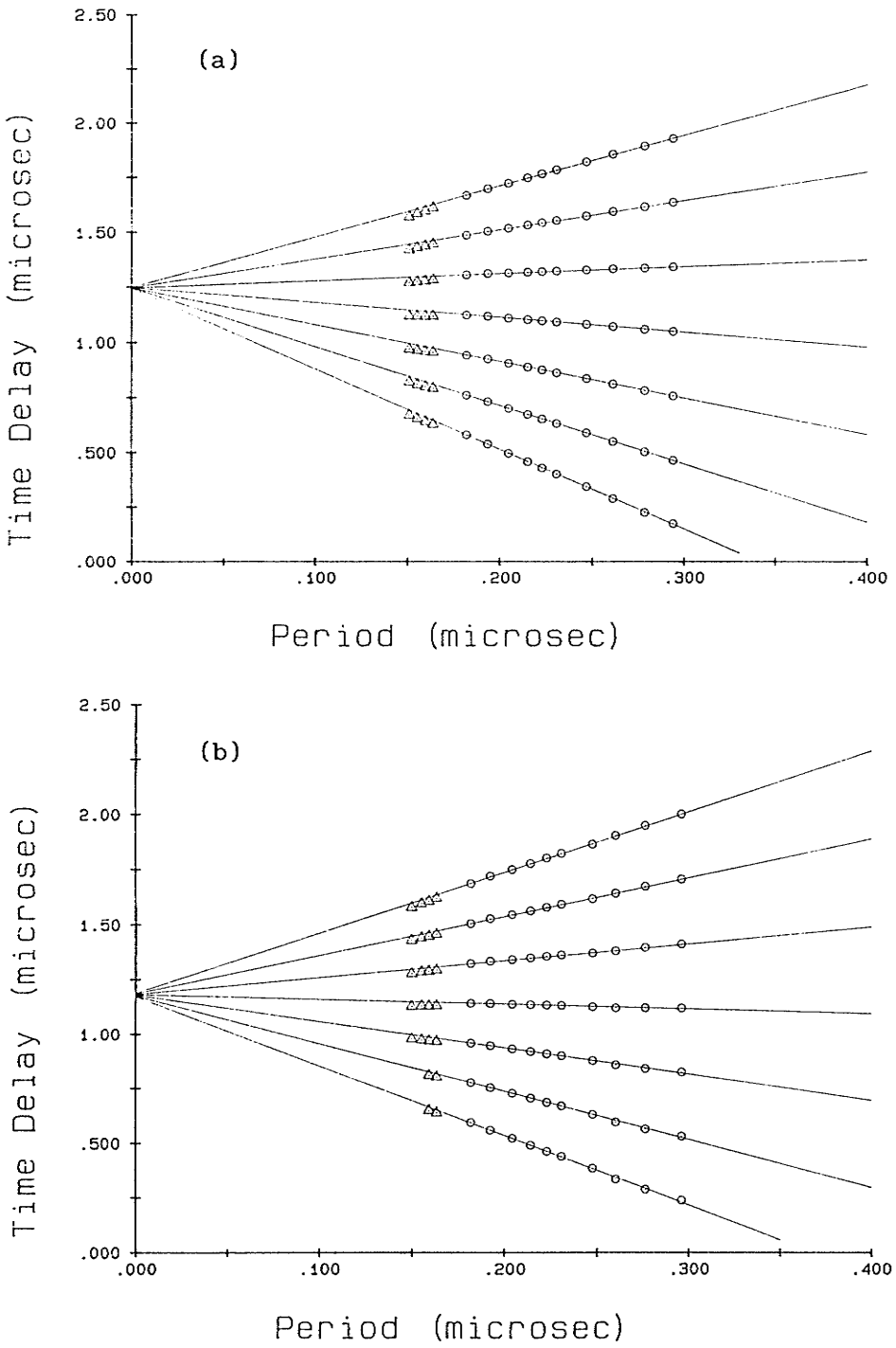

Figure D-3: Longitudinal delay measurements versus period for sample #20 , with polymer transducer **(a)** #1 and **(b)** #2 as the generator. A line (——) was fit to the collected data (⊙), which was within the range $0.17 < T < 0.30$ μs . The most horizontal line corresponds to the N=0 offset. The points (Δ) were not included in the line fits because they were mainly spurious signals.

Table D-3

Sample #21 Longitudinal

	Delay (μs)			
Points Fit:	T < 0.3 μs		0.168 < T < 0.3 μs	
N	#1 Generating	#2 Generating	#1 Generating	#2 Generating
+3	——	0.910 ± 0.008	——	0.860 ± 0.009
+2	0.855 ± 0.005	0.912 ± 0.008	0.816 ± 0.013	0.873 ± 0.006
+1	0.859 ± 0.006	0.914 ± 0.008	0.821 ± 0.009	0.880 ± 0.005
0	**0.858 ± 0.004**	**0.915 ± 0.008**	**0.825 ± 0.006**	**0.885 ± 0.004**
-1	0.858 ± 0.004	0.916 ± 0.008	0.826 ± 0.002	0.891 ± 0.004
-2	——	0.917 ± 0.008	0.827 ± 0.002	0.899 ± 0.004
-3	0.831 ± 0.006	0.918 ± 0.008	0.831 ± 0.006	0.905 ± 0.004
-4	0.861 ± 0.004	0.920 ± 0.008	0.832 ± 0.011	0.909 ± 0.004
-5	0.861 ± 0.005	——	0.835 ± 0.015	——
	$\langle\Delta t\rangle$ = (0.886 ± 0.005) μs		$\langle\Delta t\rangle$ = (0.855 ± 0.004) μs	

Table D-4

Sample #20 Longitudinal

	Delay (μs)	
Points Fit:	0.17 < T < 0.3 μs	
N	#1 Generating	#2 Generating
+3	1.189 ± 0.005	——
+2	1.186 ± 0.004	1.248 ± 0.004
+1	1.184 ± 0.003	1.246 ± 0.002
0	**1.181 ± 0.004**	**1.246 ± 0.002**
-1	1.178 ± 0.006	1.246 ± 0.002
-2	1.175 ± 0.008	1.245 ± 0.002
-3	1.173 ± 0.010	1.245 ± 0.002
-4	——	1.242 ± 0.014
	$\langle\Delta t\rangle$ = (1.214 ± 0.003) μs	

§D: 1.4 — Sample #19

The uncertainty of the zero-period extrapolations (Table D-5) of the data of sample #19 (Figure D-4) is so large because there were very few data points; only the lowest frequencies could be transmitted through the sample. Note that the path delay difference for the two transducers is only (0.01 ± 0.04) μs for this sample. This is less than the delay difference of the other samples (Table D-1), although the size of the uncertainty is nearly enough to explain the discrepancy. It is assumed some factor (such as an inferior bond similar to that of sample #22 (Figure D-1b)) has caused a timing error in one or both orientations of the delay data. The uncertainty of the average was increased to ± 0.04 μs to account for this possibility. There is also

Table D-5

Sample #19 Longitudinal

Points Fit:	Delay (μs) T < 0.3 μs	
N	#1 Generating	#2 Generating
+2	1.45 ± 0.05	1.43 ± 0.02
+1	1.42 ± 0.04	1.44 ± 0.02
0	**1.44 ± 0.03**	**1.45 ± 0.03**
-1	1.47 ± 0.03	1.48 ± 0.04
-2	1.46 ± 0.02	1.45 ± 0.06
	<Δt> = (1.44 ± 0.03) μs	

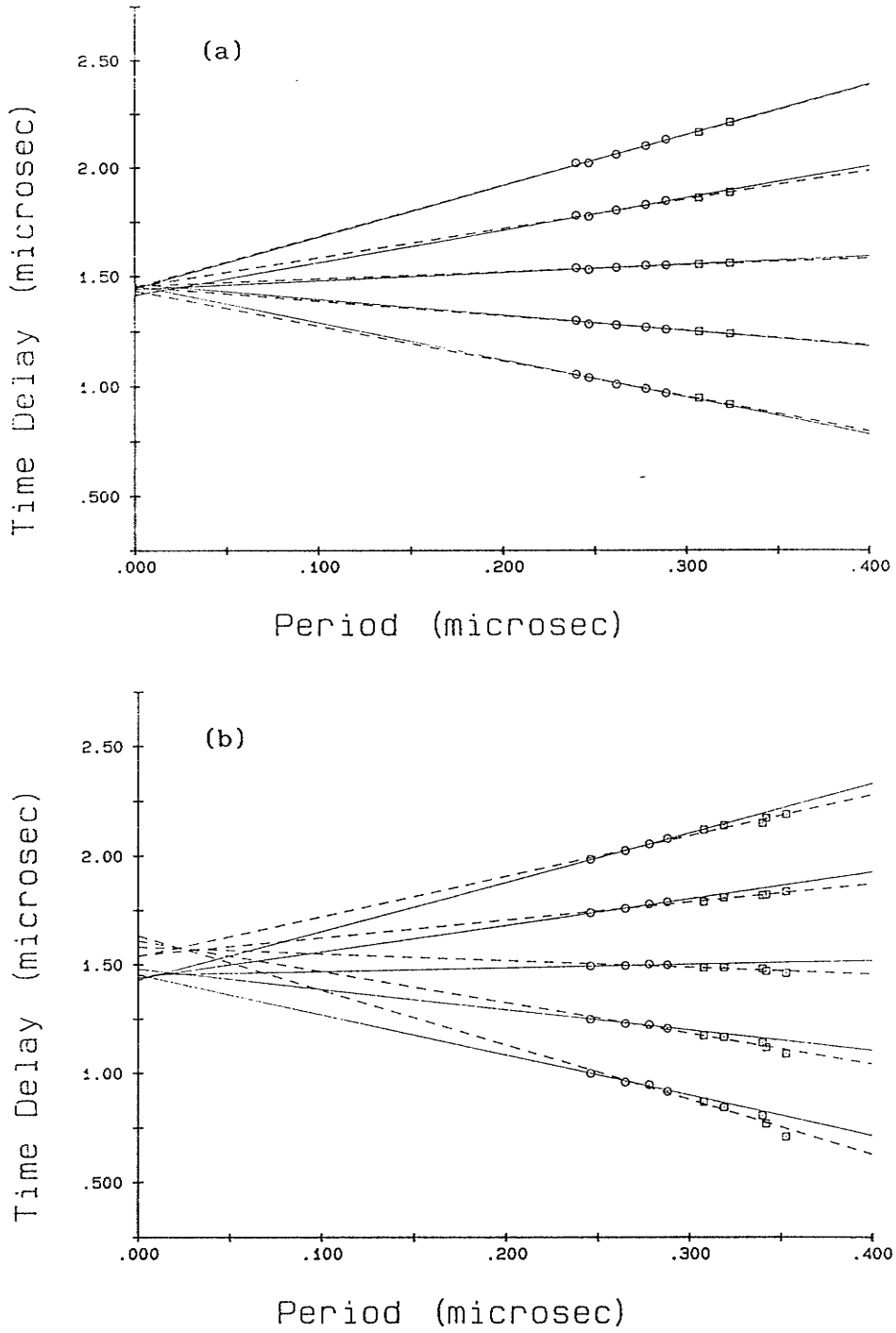

Figure D-4: Longitudinal delay measurements versus period for sample #19 , with polymer transducer **(a)** #1 and **(b)** #2 as the generator. Data was fit over the ranges $T < 0.30\ \mu s$ (——,⊙) and $T < 0.37\ \mu s$ (----, ⊙ & □). The most horizontal line corresponds to the N=0 offset.

a time delay correction of -0.03 μs due to the attenuation of the sample so that the final value of the delay is

$$\boxed{\langle \Delta t \rangle_{L}^{19} = (1.41 \pm 0.04)\ \mu s} \quad .$$

Inclusion of the higher period, edge distorted data (T > 0.30 μs) in the least-squares fit results in a calculated transist time of $\langle \Delta t \rangle$ = (1.50 ± 0.04) μs .

§D: 2 — TRANSVERSE DATA

The period range of the gathered transverse data extends up to $T \cong 0.38\ \mu s$, but when looking at Figure D-5 , it can be seen that the data at the greatest period values of sample #22 stray from the line formed by the remainder of the data. The rise time of the PZT transverse transducers is slower than that of the polymer longitudinal transducers and therefore the largest period measurements are possibly inaccurate (as described in the previous section). The points with periods $\sim 0.35\ \mu s$ *may* have accurate measurements of their periods, but it is uncertain. Since the bandwidth of the PZT transducers is much narrower than that of the polymer transducers, there were fewer data points over the same frequency range; the omission of any point has a significant effect on the line fit of the set of data. A line of good fit can be found for the data points in the period range $T \leq 0.35\ \mu s$ and also the range $T \leq 0.30\ \mu s$, although the y-intercepts of the two fitted lines differ by more than their statistical uncertainties. The transit time through the sample is quoted as the average of the two extrapolations is, with an uncertainty which encompasses each individual measurement.

The path delay difference of the two shear transducers was very small so that it was deemed unnecessary to collect data for both orientations of the transducers for each sample. Measurement in both orientations were performed for samples #21 and 22 , but only the delay data for sample #22 was sufficiently precise to determine a non-zero path

difference. The near-negligible value obtained was $\langle\Delta t\rangle_2 - \langle\Delta t\rangle_1 = 0.006 \pm 0.004\ \mu s$. The time corrections due to the phase changes induced by sample attenuation were calculated in Appendix C and most were found to be insignificant compared to the uncertainties of the calculated time delays.

§D: 2.1 — Sample #22

The measured delay time as a function of the period for sample #22 is shown in Figure D-5, and the zero-period extrapolations of a linear least-squares fit to each set of data is given in Table D-6 . The line fits over the two different period ranges of Figure D-5 yield two slightly different values, so that the transit time of shear waves through sample #22 is averaged and found to be

$$\boxed{\langle\Delta t\rangle_T^{22} = (0.904 \pm 0.010)\ \mu s} \ .$$

A correction value of $-0.002\ \mu s$ has been added to the average delay time due to the phase changes induced by sample attenuation.

§D: 2.2 — Sample #21

Shear delay measurements were performed on sample #21 on two separate occasions. Since the thickness of the sample was slightly different for the two trials, the results were analyzed separately. For

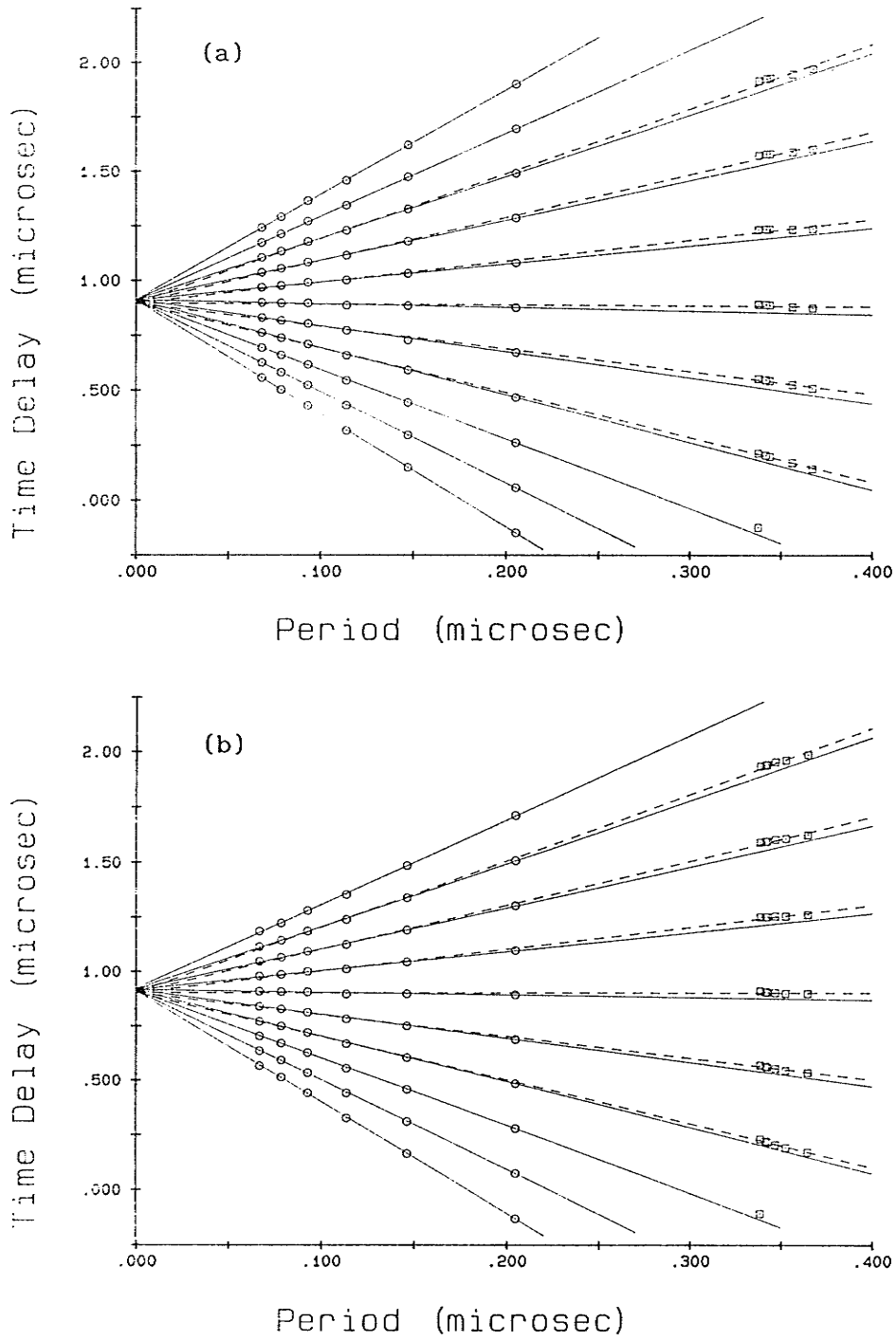

Figure D-5: Transverse delay measurements versus period for sample #22 , with PZT transducer **(a)** #1 and **(b)** #2 as the generator. Data was fit over the ranges $T < 0.30\ \mu s$ (——,⊙) and $T < 0.37\ \mu s$ (----,⊙ & □). The most horizontal line corresponds to the N=0 offset.

Table D-6

Sample #22 Transverse

	Delay (μs)			
Points Fit:	T < 0.37 μs		T < 0.30 μs	
N	#1 Generating	#2 Generating	#1 Generating	#2 Generating
+4	——	——	0.913 ± 0.003	0.924 ± 0.005
+3	0.908 ± 0.014	0.905 ± 0.006	0.912 ± 0.003	0.921 ± 0.004
+2	0.904 ± 0.013	0.905 ± 0.005	0.912 ± 0.003	0.920 ± 0.004
+1	0.901 ± 0.008	0.905 ± 0.004	0.912 ± 0.003	0.919 ± 0.004
0	**0.897 ± 0.004**	**0.905 ± 0.004**	**0.911 ± 0.003**	**0.917 ± 0.003**
-1	0.892 ± 0.008	0.905 ± 0.003	0.912 ± 0.006	0.916 ± 0.003
-2	0.890 ± 0.013	0.905 ± 0.003	0.911 ± 0.003	0.915 ± 0.003
-3	——	——	0.911 ± 0.003	0.915 ± 0.003
-4	——	——	0.910 ± 0.003	0.914 ± 0.004
-5	——	——	——	0.912 ± 0.004
	$\langle\Delta t\rangle$ = (0.901 ± 0.003) μs		$\langle\Delta t\rangle$ = (0.914 ± 0.002) μs	

trial #1 , the data is found in Figure D-6 and the zero-period extrapolations of the data are found in Table D-7 . The average of the zero-period extrapolations for the two period ranges yields the delay

$$\boxed{{}^{(1)}\langle\Delta t\rangle_T^{21} = (1.22 \pm 0.02)\ \mu s}\ .$$

Sample #21 was bonded a second time (trial #2) and the extrapolations of Figure D-7 are listed in the Table D-8 . From the extrapolations of Figure D-7 , the y-intercepts yield a transit time of

$$\boxed{{}^{(2)}\langle\Delta t\rangle_T^{21} = (1.19 \pm 0.04)\ \mu s}\ .$$

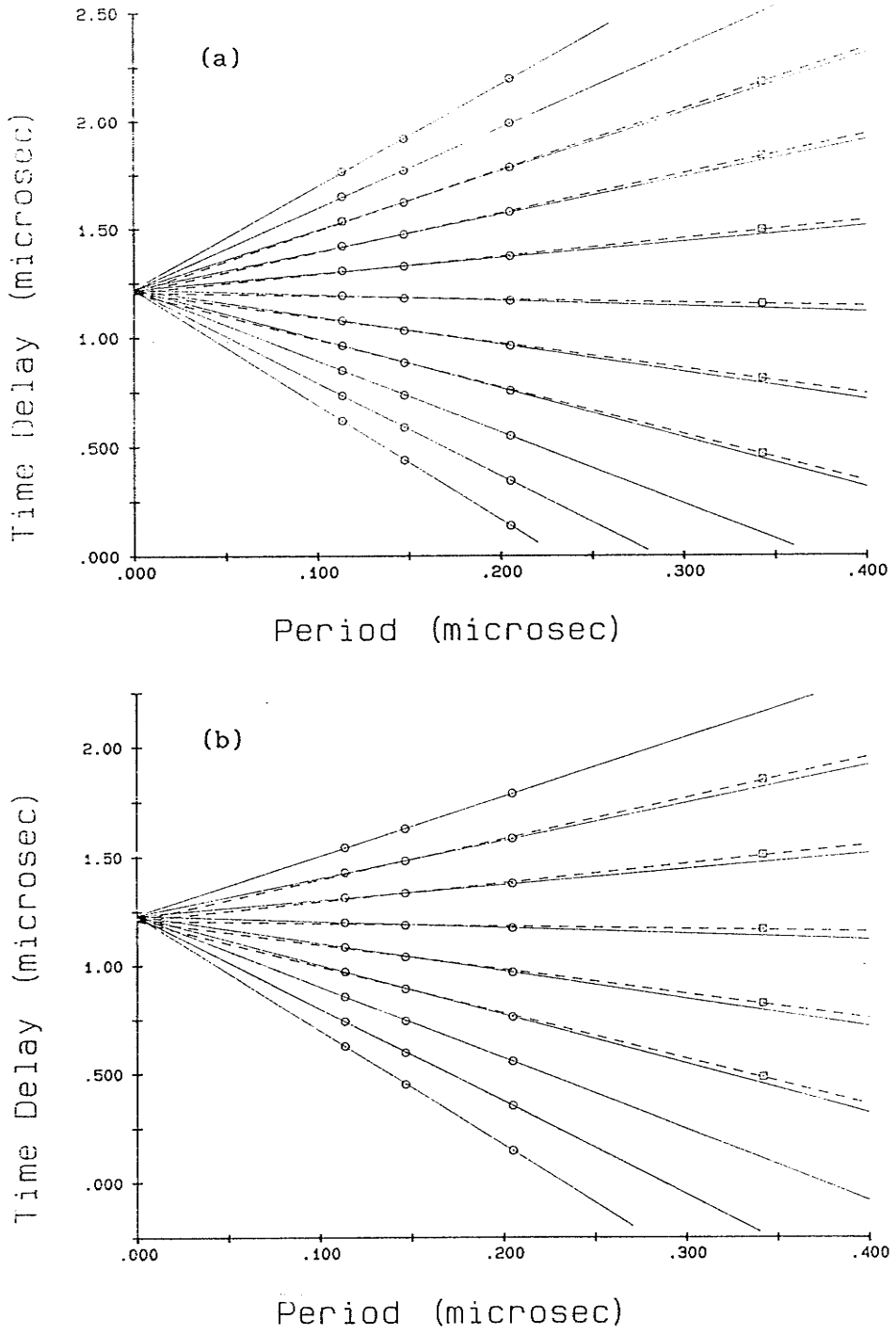

Figure D-6: Transverse delay measurements versus period for sample #21 (trial #1), with PZT transducer **(a)** #1 and **(b)** #2 as the generator. Data was fit over the ranges $T < 0.30$ μs (——,⊙) and $T < 0.36$ μs (----,⊙ & □). The most horizontal line corresponds to the N=0 offset.

Table D-7

Sample #21 Transverse
Trial #1

	Delay (μs)			
Points Fit:	T < 0.36 μs		T < 0.30 μs	
N	#1 Generating	#2 Generating	#1 Generating	#2 Generating
+5	——	——	1.226 ± 0.013	——
+4	——	——	1.224 ± 0.012	——
+3	1.210 ± 0.007	——	1.224 ± 0.012	1.235 ± 0.007
+2	1.209 ± 0.007	1.21 ± 0.01	1.224 ± 0.010	1.233 ± 0.007
+1	1.208 ± 0.007	1.21 ± 0.01	1.223 ± 0.009	1.233 ± 0.007
0	**1.206 ± 0.007**	**1.21 ± 0.01**	**1.222 ± 0.009**	**1.232 ± 0.008**
-1	1.205 ± 0.007	1.21 ± 0.01	1.221 ± 0.008	1.231 ± 0.007
-2	1.204 ± 0.007	1.21 ± 0.01	1.220 ± 0.007	1.231 ± 0.008
-3	——	——	1.220 ± 0.007	1.231 ± 0.009
-4	——	——	1.219 ± 0.006	1.229 ± 0.009
-5	——	——	1.218 ± 0.006	——
	$\langle\Delta t\rangle$ = (1.208 ± 0.006) μs		$\langle\Delta t\rangle$ = (1.225 ± 0.007) μs	

Table D-8

Sample #21 Transverse
Trial (2)

	Delay (μs)			
Points Fit:	T < 0.36 μs		T < 0.30 μs	
N	#1 Generating	#2 Generating	#1 Generating	#2 Generating
+3	1.18 ± 0.02	——	1.21 ± 0.02	1.22 ± 0.02
+2	1.18 ± 0.02	1.17 ± 0.02	1.21 ± 0.02	1.22 ± 0.02
+1	1.18 ± 0.02	1.17 ± 0.02	1.21 ± 0.02	1.22 ± 0.02
0	**1.18 ± 0.02**	**1.17 ± 0.02**	**1.21 ± 0.02**	**1.22 ± 0.02**
-1	1.18 ± 0.02	1.17 ± 0.02	1.21 ± 0.02	1.23 ± 0.02
-2	1.18 ± 0.02	1.17 ± 0.02	1.21 ± 0.02	1.23 ± 0.02
-3	1.18 ± 0.02	——	1.21 ± 0.02	1.23 ± 0.02
	$\langle\Delta t\rangle$ = (1.17 ± 0.02) μs		$\langle\Delta t\rangle$ = (1.22 ± 0.02) μs	

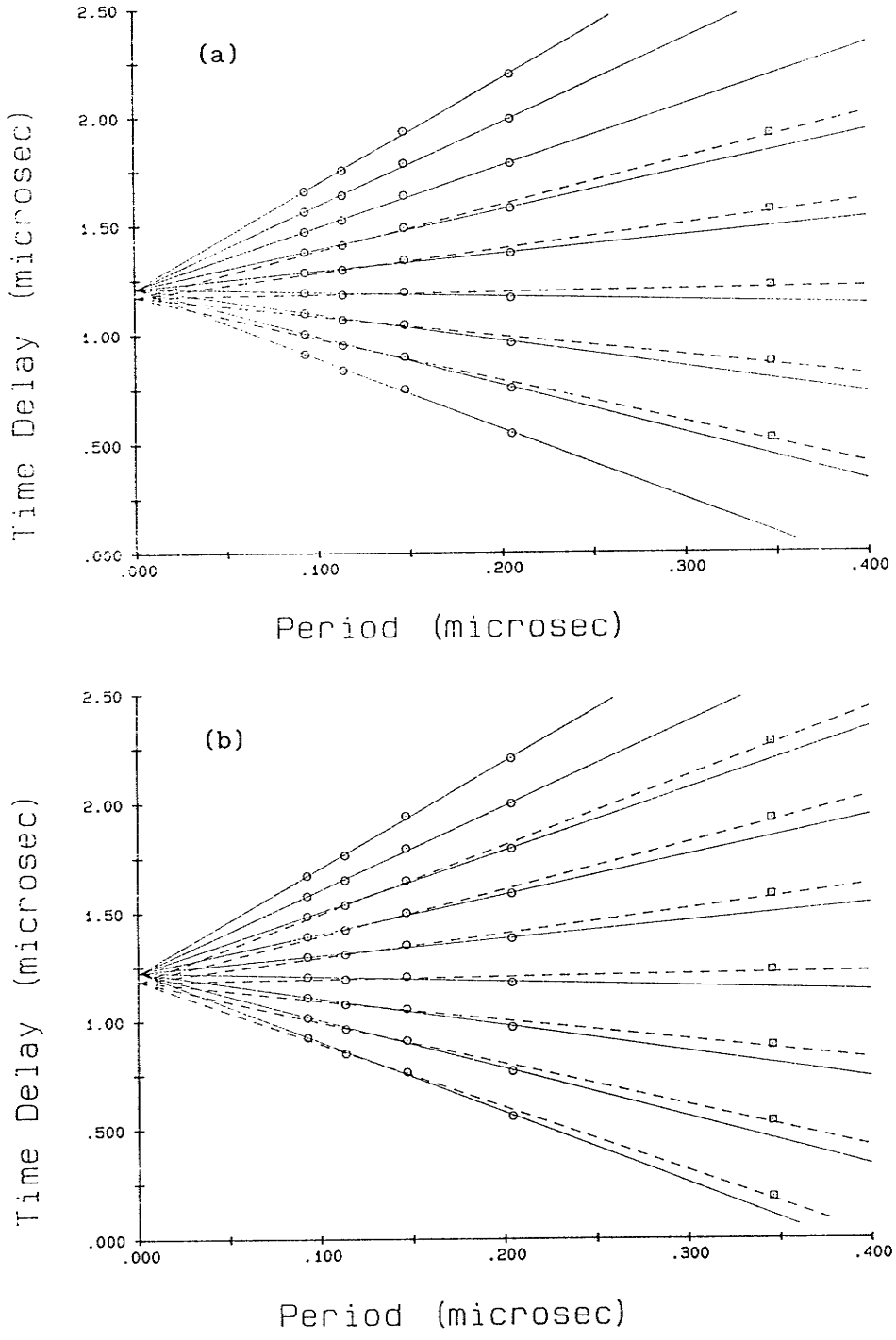

Figure D-7: Transverse delay measurements versus period for sample #21 (trial #2), with PZT transducer **(a)** #1 and **(b)** #2 as the generator. Data was fit over the ranges $T < 0.30$ μs (——,⊙) and $T < 0.36$ μs (----,⊙ & □). The most horizontal line corresponds to the N=0 offset.

§D: 2.3 — Sample #20

Figure D-8 contains the data collected for sample #20, and the zero-period extrapolations are listed in Table D-9. The average value of the N=0 offset extrapolations is

$$\langle \Delta t \rangle_T^{20} = (1.68 \pm 0.03)\ \mu s \quad .$$

Table D-9

Sample #20 Transverse

#1 Transducer Generating

Points Fit:	T < 0.36 μs	T < 0.3 μs
N	Delay (μs)	Delay (μs)
+3	——	1.63 ± 0.05
+2	1.670 ± 0.003	1.64 ± 0.07
+1	1.671 ± 0.002	1.65 ± 0.04
0	**1.672 ± 0.003**	**1.68 ± 0.03**
-1	1.674 ± 0.003	1.70 ± 0.05
-2	1.676 ± 0.003	1.70 ± 0.06
-3	——	1.76 ± 0.09

§D: 2.4 — Sample #19

As seen in Figure D-9, the range over which data could be transmitted was severely limited for this sample and therefore the uncertainty of the zero-period extrapolations (Table D-9) is sizable.

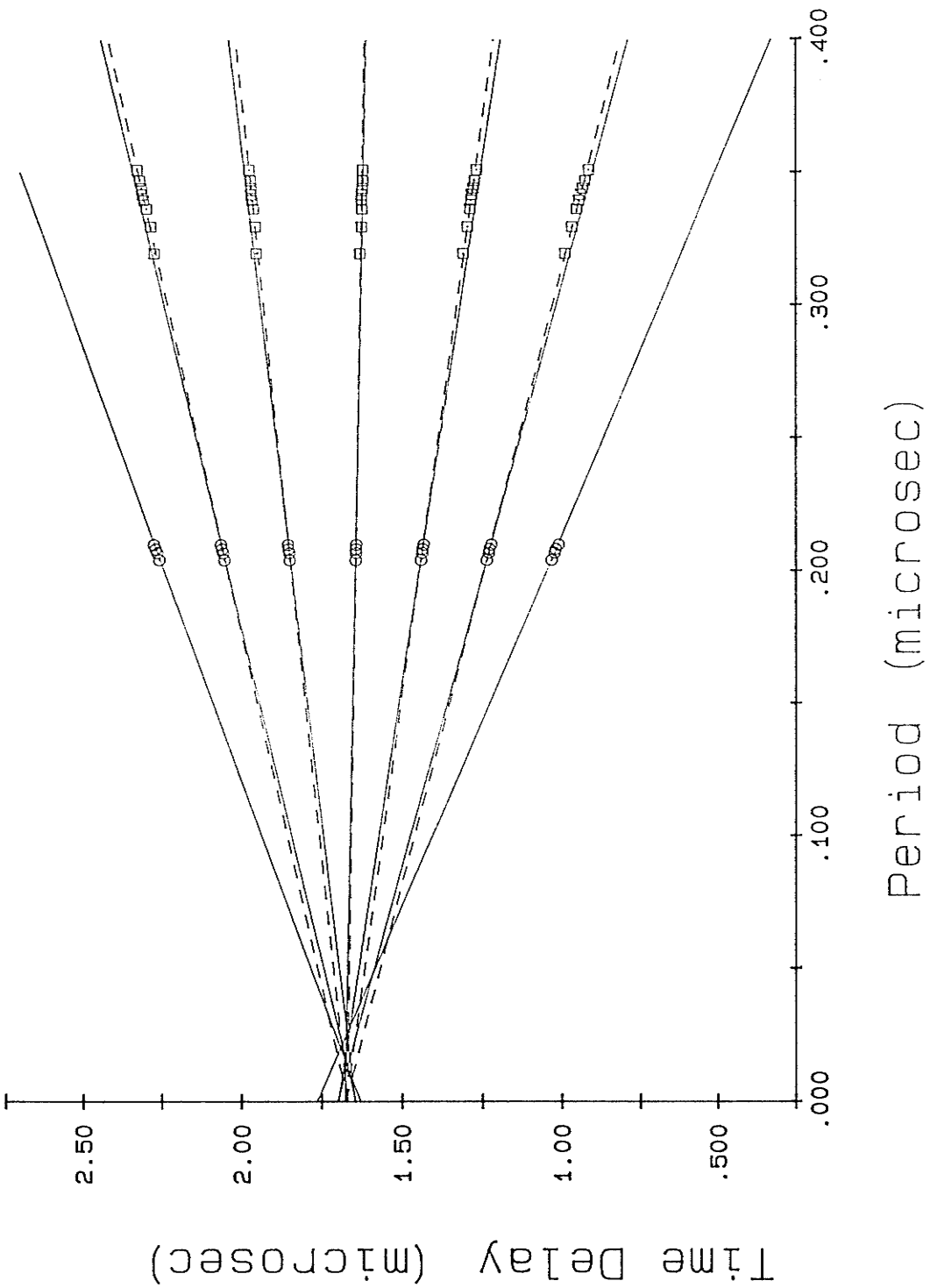

Figure D-8: Transverse delay measurements versus period for sample #20 , with PZT transducer #1 as the generator. Data was fit over the ranges $T < 0.30\ \mu s$ (——,⊙) and $T < 0.36\ \mu s$ (- - - - , ⊙ & □). The most horizontal line corresponds to the N=0 offset.

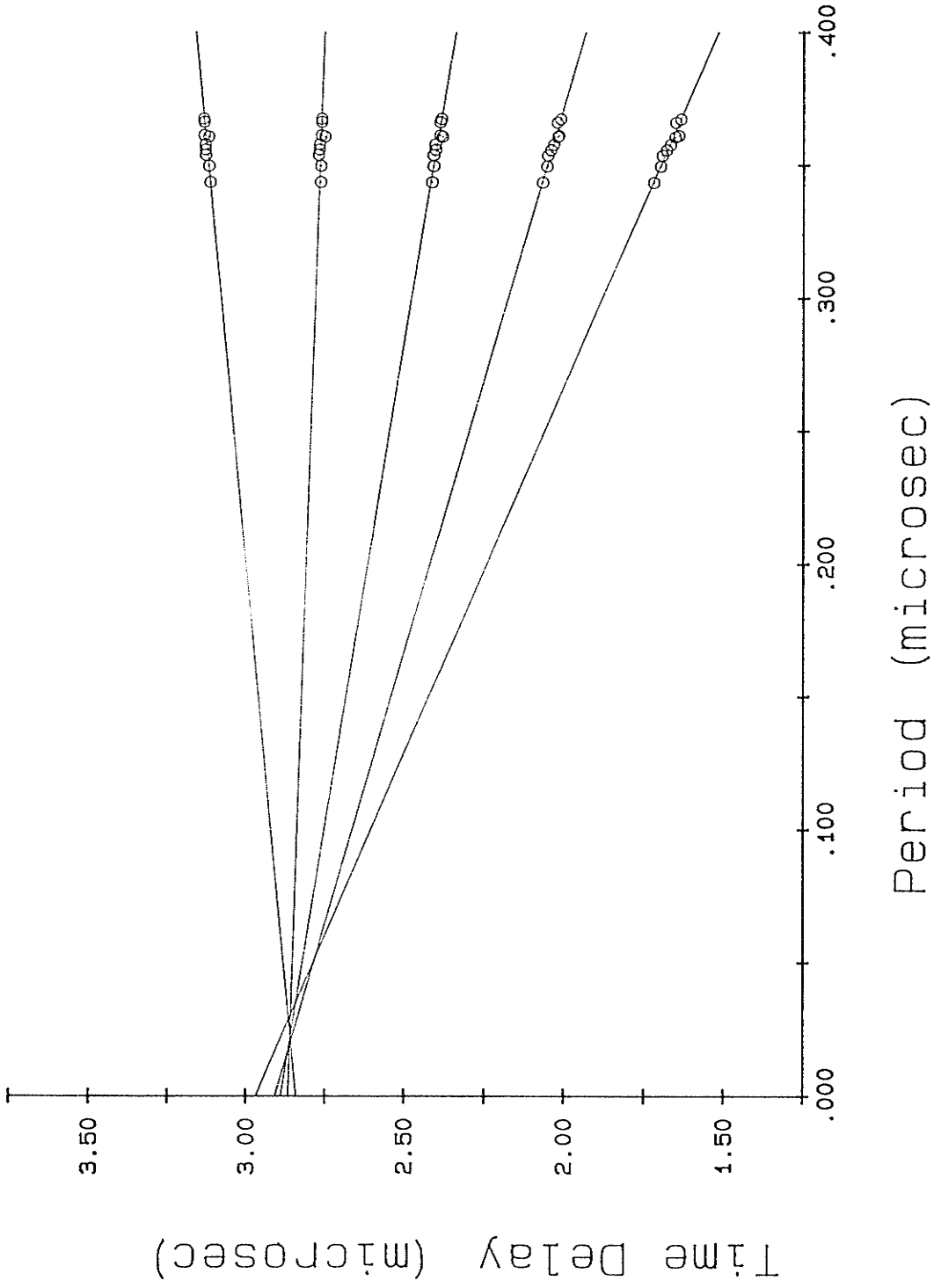

Figure D-9: Transverse delay measurements versus period for sample #19 , with PZT transducer #1 as the generator. Data was fit over the ranges $T < 0.30\ \mu s$ (——,⊙) and $T < 0.36\ \mu s$ (---- , ⊙ & □). The most horizontal line corresponds to the N=0 offset.

Also note that the range over which data could be collected for this sample was limited to the region for which the period measurements are possibly inaccurate due to pulse distortion ($T \cong 0.35\ \mu s$). In order to gain an idea of the effect of the limited and possibly distorted period range on the zero-period extrapolations, the transit time was extrapolated from the delay data of samples #20 and 22 over the period range $T > 0.30\ \mu s$ and compared to the values extrapolated from the range $T < 0.30\ \mu s$. There was no appreciable difference between the extrapolated values for sample #20 , but the values for sample #22 differed by ~0.1 μs . However this difference is not larger than the uncertainty of the extrapolated transit time (Table D-10) of sample #19 and therefore the value obtained from the extrapolations is reasonable.

$$\langle \Delta t \rangle_T^{19} = (2.9 \pm 0.2)\ \mu s$$

Table D-10

Sample #19 Transverse
#1 Transducer Generating

Points Fit: $T \cong 0.35\ \mu s$

N	Delay (μs)
+2	2.86 ± 0.11
+1	2.87 ± 0.13
0	**2.88 ± 0.13**
-1	2.85 ± 0.11
-2	2.87 ± 0.13

The final values of all of the calculated delays in this appendix are summarized in Table V-4 .

BIBLIOGRAPHY

Aharony, Amnon, Alexander, S., Entin-Wohlman, Ora and Orbach, R., *Phys. Rev. Lett.*, **58**, 132 (1987).

Alexander, S. and Orbach, R., *J. Physique Lett.*, **43**, 625 (1982).

Auld, B.A. (1973). "*Acoustic Fields and Waves in Solids*", John Wiley & Sons, New York.

Bevington, Philip R. (1969). "*Data Reduction and Error Analysis for the Physical Sciences*", McGraw Hill, Inc., New York.

Born, M. and Huang, K. (1954). "*Dynamical Theory of Crystal Lattices*", Oxford University Press, New York.

Coniglio, A., *Phys. Rev. Lett.*, **46**, 250 (1981).

Courtens, Eric, Pelous, Jacques, Phalippou, Jean, Vacher, René, and Woignier, Thierry, *Phys. Rev. Lett.*, **58**, 128 (1987).

Cusack, N.E. (1987). "*The Physics of Structurally Disordered Matter: An Introduction*", IOP Publishing Ltd., Philadelphia.

Goldstein, Joseph I., Newbury, Dale E., Echiln, Patrick, Joy, David C., Fiori, Charles and Lifshin, Eric (1981). "*Scanning Electron Microscopy and X-Ray Microanalysis*", Plenum Press, New York.

Harrison, J.P., *J. Low Temp. Phys.*, **37**, 467 (1979).

Kantor, Yacov and Webman, Itzhak, *Phys. Rev. Lett.*, **52**, 1891 (1984).

Klein, Miles V. (1970). "*Optics*", John Wiley & Sons, New York.

Lee, Sung-Ik, Noh, Tae Won and Gaines, J.R., *Phys. Rev. B*, **55**, 1626 (1985).

Maliepaard, M.C., Page, J.H., Harrison, J.P. and Stubbs, R.J., *Phys. Rev. B*, **32**, 6261 (1985).

McMillan, P.W. (1964). "*Glass-Ceramics*", Academic Press, New York.

Pachet, N. and Page, J.H., in "*Phonons 89*", ed. by Hunklinger, S., Ludwig, W. and Weiss, G. (World Scientific, Singapore) pp. 679-81, 1990.

Page, J.H. and McCulloch, R.D., *Phys. Rev. Lett.*, **57**, 1324 (1986).

Paul, A. (1982). "*Chemistry of Glasses*", p.122, Chapman and Hall Ltd., London.

Pike, R. and Stanley, H.E., *J. Phys. A*, **14**, L169 (1981).

Rammal, R. and Toulouse, G., *J. Physique Lett.*, **44**, L13 (1983).

Roux, Stéphane, *J. Phys. A*, **19**, L351 (1986).

Rutherford, A.R., Harrison, J.P., and Stott, M.J., *J. Low Temp. Phys.*, **55**, 157 (1984).

Stanley, H. Eugene and Ostrowsky, Nicole (ed.) (1986). "*On Growth and Form*", Martinus Nijhoff Publishers, Dordrecht.

Stauffer, Dietrich (1985). "*Introduction to Percolation Theory*", Taylor and Francis Inc., Philadelphia.

Weast, Robert C. (ed.) (1989). "*Handbook of Chemistry and Physics 70th Edition*", Chemical Rubber Publishing Co.

Webman, Itzhak and Grest, Gary S., *Phys. Rev. B*, **31**, 1689 (1985).